Automatic Ultra Wideband Radar System for Life Detection of Hidden Humans

Dissertation

zur Erlangung des akademischen Grades

Doktor der Ingenieurwissenschaften

(Dr. -Ing.)

der Technischen Fakultät

der Christian-Albrechts-Universität zu Kiel

Chengchung Chao

Kiel

2012

1. Gutachter: Prof. Dr.-Ing. Reinhard Knöchel

2. Gutachter: Prof. Dr.-Ing. Dr. h. c. Klaus Schünemann

Datum der mündlichen Prüfung: 15. Mai 2012

Acknowledgment

First and foremost, I would like to thank my supervisor Prof. Knöchel for the given opportunity to work in his group as a research fellow. This thesis would not have been completed without his great assistance and support. I especially would like to give deep appreciation to Dr.-Ing. Frank Daschner who contributed his knowledge, time and patience to guide me to the right way during my research.

I am particularly grateful to Dipl.-Ing. (FH) Wolfgang Taute and Miss Melanie Bork for their available support during my doctoral research. I would like to thank the following for providing help and friendship: Alexander Gülck, Falk Hettstedt, Heinz Kreft, Henning Mextorf, Holger Runkowske, Mohamed Kheir, Nasrin Nasr Esfahani, Oleksandr Teplyuk, Payman Rezaee, Robert Jahns, Thomas Lehmann.

I would like to express my deepest gratitude to my wife Lingli for her patience and support.

Kiel, October 2012

Chengchung Chao

Contents

List of Figures

List of Tables

Chapter 1

Introduction

The ultra-wideband (UWB) is a radio technology which can be used at very low energy levels for short-range high-bandwidth communications by using a large portion of the radio spectrum. In February 2002, the Federal Communications Commission (FCC) gave the permission for UWB to be used for imaging and radar production. The corresponding technology is continuing to be developed furthermore, especially the radar applications of life detection [1–16].

In various situations, the life-detection system for vital parameter detection is a highly useful and important application. It can be used to search for living objects in collapsed buildings after an earthquake or trapped in buildings on fire, or avalanche victims. It can also be used to monitor patients in clinics or at home where it can provide remote measurements of the parameters of a patient's vital activity without having contact with them. In addition, it can be used by law-enforcement services to search for criminals hiding behind various covers. Consequently, there is a growing demand for remote monitoring appliances of

human life detector systems.

In previous works, a UWB radar has been suggested for remote monitoring of a patient's vital signs [9–16]. The main advantages of UWB radar are: (1) high material-penetration capability; (2) low electromagnetic interference as well as lower specific absorption rates; (3) good immunity against multipath interference, which is very important within buildings and collapsed buildings; and (4) large bandwidth which allows a better separation between target and clutter.

Recently, the attention to radar based life detection systems has increased. The UWB radar is widely used to detect life parameters because of its simple structure and high sensitivity [9–16]. It can detect life parameters of humans non-invasively, even behind a barrier such as brick walls, debris, and clothes. The radar transmits electromagnetic waves to the human body and receives echo waves modulated by the body surface movements caused by its physiological activities. Life parameters such as distance (or direction), position, and breath frequency can be extracted according to the echo waves.

Unfortunately, most of the research [9–16] about seeing through the walls do not report as for their systems: According to this, there arise four problems in practical situations. The first problem is the calculation of the distance or position of a person. A reason for this is not only the effect of the wall with different permittivity and thickness but also the wave transmission angle toward the wall. These effects can cause errors in the distance calculation. Another reason is that

the origin of moving signals due to chest movement is not fixed. Therefore the result of the distance calculation is changed over the time. But the magnitudes of the changes are relatively small. The second problem is that the conventional signal processing is not fast, robust and accurate enough for an application in practical situations, especially in rescue operations. The third problem is that most of the articles also do not describe whether their systems are automatic or not. In practical situations, an automatic system is necessary. The fourth problem is that the surface of a human chest is not smooth and the chest movement in front of a human is more intensive than at the back. The breath frequency due to chest movement is easy to get in front of a human. That means, in practical situations the breath frequency cannot be determined at each angle. This is a very important point to take into account especially in rescue operations. The sensitive range could be expanded by the usage of more than one system in order to find someone in ruins or behind a wall.

In this sense, a UWB system has to be improved to be applied in practical situations. Indeed an automatic system with a fast, robust and accurate algorithm of signal processing is necessary. According to this, ongoing research will not only describe about the effect of the wall for distance estimation on the one hand but also build up an automatic system with a fast and robust algorithm for signal processing on the other hand. In this work the system is used to finish one-dimensional and two-dimensional measurements. For understanding the characteristics of different angles, a breath simulator is made. This simulator makes the reference measurements more reliable.

The concept of this work is based on transmitting sub-nanosecond pulses to achieve the measurement of an imitated breath movement. For signal processing, a Matlab program was developed. Averaging, variance and zero-phase filtering with round trip time are used to remove interferences of the wall, improve the signal to noise ratio (SNR), and determine the position after removing background distortions respectively. The breath frequency is determined from received reflected signal. The method can help us to detect the existence of human beings effectively and to identify parameters like respiration and body position signals automatically. A fast, robust and accurate method is used to extract the life parameters. The experimental setup and the measurement method, signal processing and practical results of tests are presented in the following chapters.

The algorithm is tested in three different types of measurements: a one-dimensional, a two-dimensional and one with a breathing simulator in different positions and angles to check its ability and feasibility. The positions and breath frequency are extracted with good accuracy and the best measurement angles are defined. The measurement setup, signal processing and results of the three designed measurements are described individually. This method is applicable in a real situation.

This work is organized as follows: in chapter 2 a theoretical background gives some specific aspects regarding the UWB radar system, the process of measurement, the permittivity of a three-layer wall and the effect of measured distance with different transmitting angles, and the basic concept of an interface from air to dry skin will be described. In chapter 3 details of the experimental proce-

dures in a one-dimensional measurement and an algorithm for signal processing are developed. The results of the experiments are shown in this chapter also. Chapter 4 describes details of the experimental procedures in four kinds of two-dimensional measurements and upgrades the algorithm for signal processing presented in chapter 3. The results of the experiments are also shown in this chapter. Chapter 5 describes the creation of a breath simulator to imitate human frequency. Chapter 6 details the experimental procedures and the effect at different angles with the breath simulator and the same algorithm that was used in the one-dimensional and two-dimensional measurements are investigated. The results of these experiments are also shown in this chapter. Finally, chapter 7 summarizes the conclusions obtained during this investigation and talks about future research.

Chapter 2

Through wall measurements using UWB pulses

2.1 Electromagnetic Theory

Maxwell's equations describe electricity, magnetism, space, time and the relationships among them. They are simple and fundamental. They are a set of four partial differential equations that relate the electric and magnetic fields to their sources, charge density and current density. These equations can be combined to show that light is an electromagnetic wave. Individually, the equations are known as Gauss's law, Gauss's law for magnetism, Faraday's law of induction, and Ampere's law with Maxwell's correction. The set of equations is named after James Clerk Maxwell. The general form of time-varying Maxwell's equations in free space can be written in differential or integral form. For general time-varying electromagnetic fields, they are given as follows [17,18]:

Differential form of Maxwell's equations

$$\nabla \times \vec{E} = -\frac{\partial \vec{B}}{\partial t}, \tag{2.1}$$

$$\nabla \times \vec{H} = \vec{J} + \frac{\partial \vec{D}}{\partial t}, \tag{2.2}$$

$$\nabla \cdot \vec{D} = \rho_v, \tag{2.3}$$

$$\nabla \cdot \vec{B} = 0. \tag{2.4}$$

Integral form of Maxwell's equations

$$\oint_c \vec{E} \cdot d\vec{l} = -\oint_s \frac{\partial \vec{B}}{\partial t} \cdot d\vec{S}, \tag{2.5}$$

$$\oint_c \vec{H} \cdot d\vec{l} = (\vec{J} + \frac{\partial \vec{D}}{\partial t}) \cdot d\vec{S}, \tag{2.6}$$

$$\oint_s \vec{D} \cdot d\vec{S} = \oint_v \rho_v dv, \tag{2.7}$$

$$\oint_s \vec{B} \cdot d\vec{S} = 0. \tag{2.8}$$

Where

$\vec{D}$ is the electric flux density in $Coulombs/m^2$

$\vec{B}$ is the magnetic flux density in Wb/m^2

$\vec{E}$ is the electric field intensity in V/m

$\vec{H}$ is magnetic field intensity in A/m

ρ_v is the electric charge density in $Coulombs/m^3$

$\vec{J}$ is the current density in A/m^2

In order to solve four field quantities, three constitutive relations are needed for using Maxwell's equations. They basically describe the relations between the fields through the properties of the medium. Under the time-harmonic assumption, the electric flux density $\vec{D}$ and electric field $\vec{E}$ in a simple medium are related [17,18] by

$$\vec{B} = \mu_0 \vec{H}, \tag{2.9}$$

$$\vec{D} = \epsilon_0 \vec{E}, \tag{2.10}$$

$$\vec{J} = 0. \tag{2.11}$$

Where μ_0 and ϵ_0 are the permeability and the permittivity of a vacuum respectively. The values are $\mu_0 = 4\pi * 10^{-7} H/m$ and $\epsilon_0 = 8.8542 * 10^{-12} F/m$. Maxwell's equations under the source-free condition are obtained by letting $\vec{J} = 0$. For real-world materials, the constitutive relations are not simple proportionalities, but approximations. The relations can usually still be written:

$$\vec{B} = \mu \vec{H}, \tag{2.12}$$

$$\vec{D} = \epsilon \vec{E}, \tag{2.13}$$

$$\vec{J} = \sigma \vec{E}. \tag{2.14}$$

Where $\epsilon = \epsilon_r \epsilon_0$, $\mu = \mu_r \mu_0$, ϵ_r is the permittivity of material, μ_r is the permeability of material. σ is the specific electric conductivity in a unit of (A/Vm). In general ϵ_r, μ_r and σ are functions of the location and direction in the medium as well as the power level applied to the medium. Most substrates used for electronic circuits,

however, are homogeneous, isotropic, and linear, having those constant. They are known as simple materials (media) [17,18]. Furthermore, most electronic substrates are nonmagnetic, having a relative permeability of 1. In this research, we will consider the reflection coefficient, velocity and travelling time respectively from the relative dielectric constant and permeability of a human chest and a penetrated wall.

2.2 Target model

A model for the target properties and the expected target movement has to be defined for this UWB radar application. The human lung of an adult human is located behind the chest and has a volume of approximately 4 to 6 liters. The tidal chest volume is normally between 500 ml and 800 ml. The breath rate is about 16 to 18 cycles per minute. The chest movement caused by breathing activity is around 1 to 2 cm [9, 19]. This movement is relatively small, a high resolution radar like a UWB radar has to be used to achieve breath detection. The radiated electromagnetic pulse coming from the transmitting antenna of the UWB radar will be reflected partly at every dielectric boundary. The main reflection will happen at the air/chest interface. The propagation impedance in free space η_0 is defined to

$$\eta_0 = \sqrt{\frac{\mu_0}{\epsilon_0}}. \tag{2.15}$$

Where μ_0 and ϵ_0 having been shown in previous section are the values of permeability and the permittivity of vacuum respectively. The value 376.3 Ω of η_0 can be

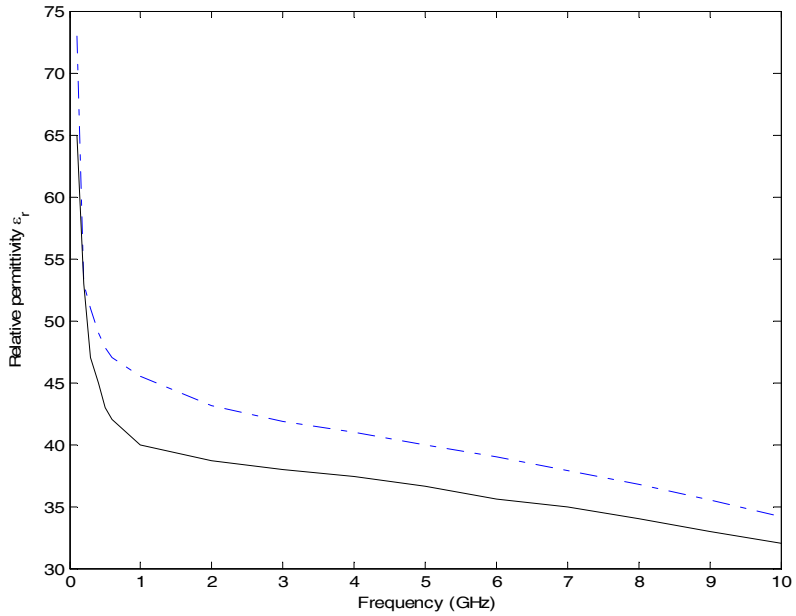

Figure 2.1: *Relative permittivity of dry skin (solid) and wet skin (dashed and dot) for the frequency range of 100 MHz to 10 GHz.*

calculated from equation 2.15. By taking the relative permittivity ϵ_r into account, the propagation impedance η in a material can be determined by

$$\eta = \sqrt{\frac{\mu_0}{\epsilon_0 \epsilon_r}}. \tag{2.16}$$

Due to dielectric relaxation of polar molecules (water), the relative permittivity of dry skin and wet skin is dependent for the frequency range of 100 MHz to 10 GHz [19] as shown in Figure 2.1.

For example dry skin has a relative permittivity $\epsilon_r = 40$ at a frequency of 1.4 GHz. This leads to a propagation impedance of

$$\eta_{skin} = \sqrt{\frac{\mu_0}{\epsilon_0 \epsilon_r}} = 59.57\Omega. \tag{2.17}$$

The reflection coefficient Γ is defined as

$$\Gamma = \frac{\eta_{skin} - \eta_0}{\eta_{skin} + \eta_0}. \tag{2.18}$$

Therefore the reflection at the air/skin interface can be calculated at 72%. This means it is possible to receive a reflected signal from the air/chest interface [9].

As mentioned above, breathing activity causes a chest movement of about 1 to 2 cm. If it is possible to detect the distance of the air/skin interface exactly with an appropriate repetition frequency, the according breathing rate could be determined.

2.3 The penetrated wall

It is necessary to determine the permittivity of the walls for doing measurements. Practically, walls are not simple dielectric layers with easily measurable permittivity. Generally, walls contain a certain number of layers with different permittivity, for example, a gas-concrete wall with gypsum board and rock wool heat-insulation.

Figure 2.2 shows the lightweight structure of the wall including three layers of materials for the measurements made in this work. Both the first and third layer are gypsum boards with 1.5 cm thickness. The second layer between the two boards is filled with rock wool with a thickness of 9 cm. The whole thickness of

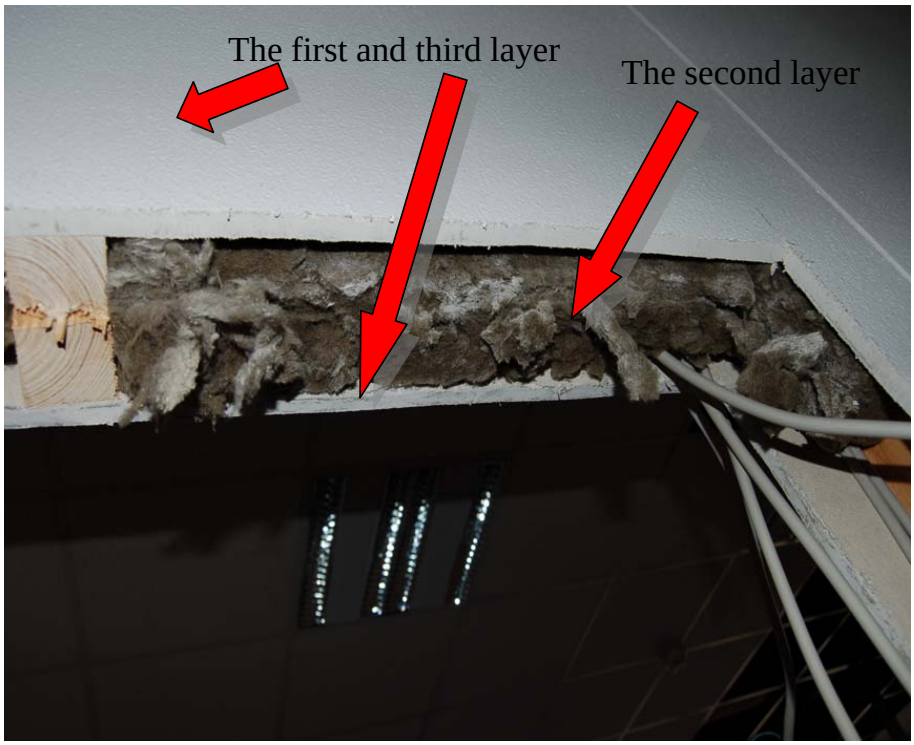

Figure 2.2: *Real structure of the wall for the measurements made in this work.*

the wall is 12 cm. The permittivity of rock wool and gypsum are approximately 2 and 3.7 respectively [20] [21]. It should be mentioned that a real wall has often pieces of metal are much thinner than the wall, hence the distortions of the metals are relatively low. In addition, the system used in this research is a UWB system and this distortion does not have a big effect on the accuracy of the measurement.

It is necessary that the wall structure makes wave penetration possible through specific building materials such as concrete blocks. When the wave reaches at the wall at a certain angle, the wave will continue its propagation in the wall but with changed directions in different layers. This is also valid in the case when the permittivity of the wall differs from the permittivity of the layers in front of the wall. Furthermore, when the wave leaves the wall, it changes its direction once

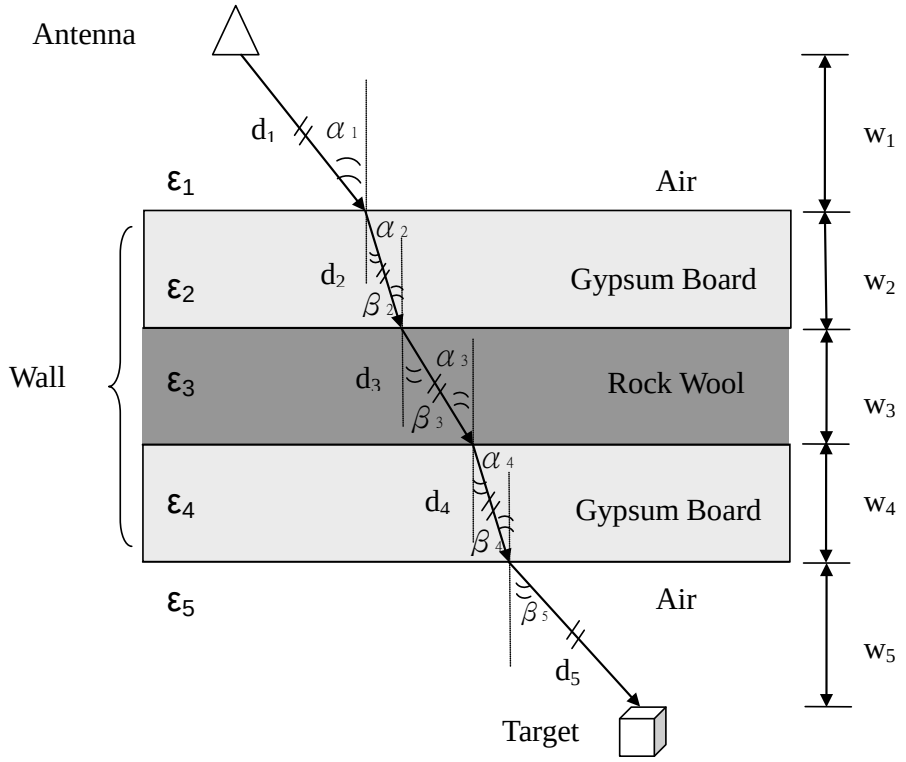

Figure 2.3: *True flight distance model through the wall.*

more. When the permittivity of the wall is greater than the permittivity of the air, which is in general the case, the wave velocity in the wall will be lower than in the air.

To estimate the correct distance or position of the objects behind the wall, the exact time of arrival (TOA) between the antenna and the object has to be known. This research is focused on computation of the true TOA between antenna and target, with a wall between them. The losses in the wall are not considered. For the calculation of this time, the model shown in Figure 2.3 is used.

The wall with 3 layers is almost homogeneous with constant permittivity and

constant thickness. The values of relative permittivity of the wall are $\epsilon_2 = \epsilon_4 = 3.7$ and $\epsilon_3 = 2.0$. The thicknesses are $w_2 = w_4 = 1.5$ cm and $w_3 = 9.0$ cm. The relative permittivity ϵ_1 and ϵ_5 of the air in front of the wall and behind are the same and equal to 1. The wave velocity in the air is equal to the velocity of light c. The velocity in different permittivity layers is given as

$$v_n = \frac{c}{\sqrt{\epsilon_n}}. \tag{2.19}$$

Because the three material layers inside the wall are homogeneous respectively, the angles have the relation $\beta_2 = \alpha_2$, $\beta_3 = \alpha_3$ and $\beta_4 = \alpha_4$. The true flight distance between antenna and target is not equal to the straight distance between them. It has to be computed as summation of distances.

$$d_{tot} = \sum_{i=1}^{n} d_n. \tag{2.20}$$

The travelling time in each layer is the ratio of distance to speed

$$t_n = \frac{d_n}{v_n}. \tag{2.21}$$

Now, the true TOA can be computed as the summation of 5 times

$$\begin{aligned} TOA &= \sum_{i=1}^{n} t_n \\ &= \sum_{i=1}^{n} \frac{d_n}{v_n}. \end{aligned} \tag{2.22}$$

Figure 2.4 shows the geometry for a plane wave obliquely incident at the interface between two dielectric layers. Snell's law expresses that the ratio of the sines of the angles of incident and refracted wave equals to the ratio of velocities in the

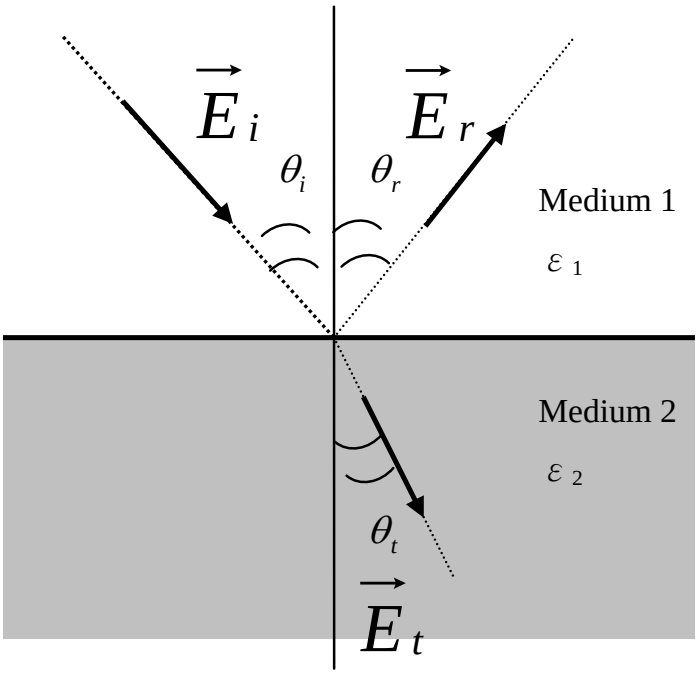

Figure 2.4: *Geometry for a plane wave obliquely incident at the interface between two dielectric regions.*

two media [22]. θ_i is the angle of incidence. θ_t is the angle of refraction. The equation can be defined as

$$\frac{\sin\theta_i}{\sin\theta_t} = \frac{v_1}{v_2}. \tag{2.23}$$

θ_t can be written as

$$\theta_t = arcsin\left(\frac{v_2}{v_1}\sin\theta_i\right). \tag{2.24}$$

In a medium with many layers θ_{tn} replaces θ_t and can be written as

$$\theta_{tn} = arcsin\left(\frac{v_n}{v_1}\sin\theta_i\right). \tag{2.25}$$

From the equation 2.25, the d_n can be easily determined as

$$\begin{aligned} d_n &= \frac{w_n}{cos\theta_{tn}} \\ &= w_n \sec[\arcsin(\frac{v_n}{v_1}\sin\theta_i)] \\ &= w_n \frac{1}{\cos[\arcsin(\frac{v_n}{v_1}\sin\theta_i)]}. \end{aligned} \tag{2.26}$$

It is known that $\sin^2\theta_i + \cos^2\theta_i = 1$. Let $\theta_i = \arcsin x$, then $\cos\theta_i = \sqrt{1-[\sin(\arcsin x)]^2} = \sqrt{1-x^2}$ can be determined, the converting $\cos(\arcsin x)$ will be

$$\begin{aligned} \cos(\arcsin x) &= \cos\theta_i \\ &= \sqrt{1-x^2}. \end{aligned} \tag{2.27}$$

According to the equation 2.27, the equation 2.26 can be determined as

$$\begin{aligned} d_n &= w_n \frac{1}{\left[1-(\frac{v_n}{v_1}sin\theta_i)^2\right]^{\frac{1}{2}}} \\ &= w_n \left[1-(\frac{v_n}{v_1}sin\theta_i)^2\right]^{-\frac{1}{2}}. \end{aligned} \tag{2.28}$$

By the equations 2.19 and 2.28, the equation 2.22 can be converted as

$$TOA = \sum_{i=1}^{n}\left(\frac{w_n\sqrt{\epsilon_n}}{v_1}\right)\left[1-(\frac{v_n}{v_1}sin\theta_i)^2\right]^{-\frac{1}{2}}. \tag{2.29}$$

In our case v_1 is equal to c. Equation 2.29 is simply re-written to

$$\begin{aligned} TOA &= \sum_{i=1}^{n}\left[\frac{w_n}{c}\left(\sqrt{\epsilon_n}\right)\right]\left[1-(\frac{v_n}{v_1}\sin\theta_i)^2\right]^{-\frac{1}{2}} \\ &= \sum_{i=1}^{n}\left(\frac{w_n}{c}\right)\left(\frac{\epsilon_n}{\sqrt{\epsilon_n-\sin^2\theta_i}}\right). \end{aligned} \tag{2.30}$$

2.4 UWB pulse

The basic physical principle for the operation of a microwave life-detection system is simple, as shown in Figure 2.5 [9–16]. When a microwave signal with proper frequency is transmitted toward a human body which is in a collapsed building, the microwave signal can penetrate the barrier or the rubble, and then reach the human body and cause reflection. The reflected wave from the human body will enter the signal processing and be modulated by breath movements. If the clutter of the reflected wave from a stationary background can be completely eliminated and the reflected wave from the human body's movement is properly modulated, a human body which has been buried under earthquake rubble or hidden behind barriers can be located. Therefore, breathing signals of the human chest can be extracted.

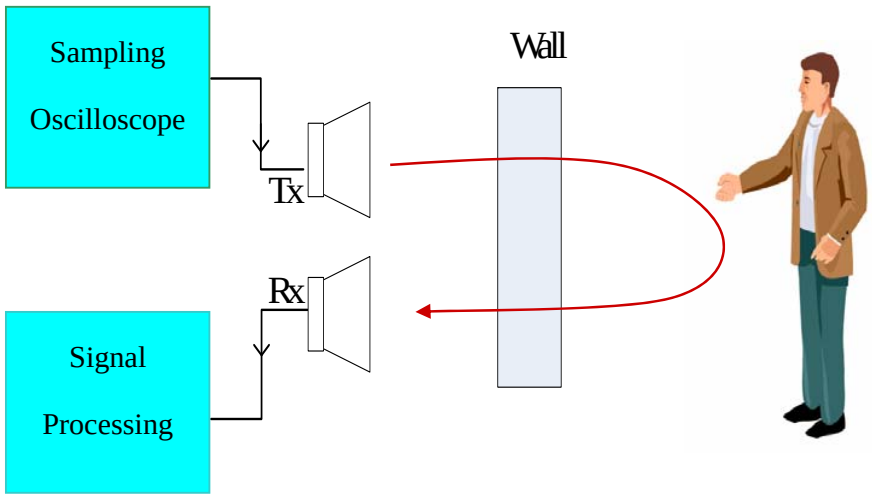

Figure 2.5: *The basic physical principle of a microwave life-detection system.*

A UWB radar transmits short impulses with pulse duration ranging from sub-

nanoseconds to a few nanoseconds. Due to the high resolution of UWB signals, the expansion of a chest cavity will cause noticeable variations to estimate the position and respiration rates.

For all life-detection radar systems, it is difficult to extract weak life signals from strong echo waves of the background. In a practical application there are four major problems: The first is the complexity of the algorithm. The second is how fast the result can be determined. The third is how robust the prediction of the life parameters is. The last is how accurate the results are. For the purposes of getting distance, position or frequency, a UWB system with a Matlab program has been developed to process the measured signal.

2.5 Mathematical approach

In this research, one of the goals which has been introduced in chapter 1 is building a fast, accurate and robust signal processing algorithm. It is important to use appropriate mathematical approaches for developing it. The methods including mean, filtering, variance and fast Fourier transform are described as follows.

2.5.1 Mean

The arithmetic mean is the "standard" average. It is often simply called the "mean". Assume we have a row vector $x_1, \ldots, x_n.$, then the arithmetic mean A is defined

via the equation

$$A = \frac{1}{n}\sum_{i=1}^{n} x_i. \tag{2.31}$$

If **A** is a matrix with size $M \times N$. Then the **A** can be determined

$$\mathbf{A}_n = \frac{1}{M}\sum_{m=1}^{M} \mathbf{X}_{m,n}, \tag{2.32}$$

where $1 \leq m \leq M$, $1 \leq n \leq N$.

The arithmetic mean has several properties that make it useful, especially as a measure of central tendency [23–25]. These include:

1. If numbers $x_1, ..., x_n$ have mean A, then$(x_1 - A) + ... + (x_n - A) = 0$. Since $x_i - A$ is the distance from a given number to the mean, one way to interpret this property is that the numbers to the left of the mean are balanced by the numbers to the right of the mean. The mean is the only single number for which the residuals defined this way sum to zero.

2. If it is required to use a single number A as an estimation for the value of numbers $x_1, ..., x_n$, then the arithmetic mean does this best, in the sense of minimizing the sum of squares $(x_i - A)^2$ of the residuals. (It follows that the mean is also the best single predictor in the sense of having the lowest root mean squared error).

3. For a normal distribution, the arithmetic mean is equal to both the median and the mode, other measures of central tendency.

2.5.2 Digital finite impulse response (FIR) filters

In signal processing, a filter is a device or process that removes from a signal some unwanted component or feature. Filtering is a class of signal processing, the defining feature of which is the complete or partial suppression of some aspect of the signal. Mainly, this means removing some frequencies and not others in order to suppress interfering signals and reduce background noise [23].

The difference equation that defines the output of an FIR filter in terms of its input can be written as:

$$\mathbf{y}[n] = b_0 x[n] + b_1 x[n-1] + b_2 x[n-2] ... + b_N x[n-N], \tag{2.33}$$

where:

- $\mathbf{x}[n]$ is the input signal,
- $\mathbf{y}[n]$ is the output signal,
- $\mathbf{b}_i$ is the filter coefficient, and
- N is the number of filter order - an Nth-order filter should have (N + 1) terms on the right-hand side.

This equation can also be expressed as a convolution of the coefficient sequence $\mathbf{b}_i$ with the input signal:

$$\mathbf{y}[n] = \sum_{i=0}^{N} \mathbf{b}_i \mathbf{x}[n-i]. \tag{2.34}$$

This means that the filter output is a weighted sum of the current and a finite

number of previous values of the input.

The finite impulse response filters (FIR) have some interesting properties that make them attractive in realisation and application [23]:

1. They are naturally stable. This is due to the truth that all the poles are located at the origin and therefore are located within the unit circle.
2. No feedback is required. This means that any rounding errors are not compounded by summed iterations. The same relative error occurs in each calculation. This can also make an implementation simpler.
3. By making the coefficient sequence symmetric; linear phase, or phase change proportional to frequency, these filers which can easily be designed to be linear phase corresponds to equal delays at all frequencies.

2.5.3 Variance

The variance of a random variable or distribution is the squared deviation of that variable from its expected or value mean. Thus, the variance is an evaluation of the amount of variation within the values of that variable, taking account of all possible values and their probabilities or weightings [24, 25].

If a random variable $\mathbf{B}$ with size $M \times N$ has the expected value (mean) $\overline{\mathbf{B}}$, then the

variance of **C** is given by:

$$\begin{aligned} \mathbf{C}_n &= s^2 \\ &= \frac{\mathbf{1}}{M-1}\sum_{m=1}^{M}(\mathbf{B}_{m,n} - \overline{\mathbf{B}}_n)^2, \end{aligned} \tag{2.35}$$

where

$$\overline{\mathbf{B}}_n = \frac{1}{M}\sum_{i=1}^{M}\mathbf{B}_{m,n}. \tag{2.36}$$

2.5.4 Fast Fourier transform(FFT)

A fast Fourier transform (FFT) is an efficient algorithm to compute the discrete Fourier transform (DFT). From simple complex-number arithmetic to group theory and number theory, there are many distinct FFT algorithms involving a wide range of mathematics. A DFT decomposes a sequence of values into components of different frequencies. This operation is useful in various fields, but it is often too slow from the definition to be practical computing directly. An FFT is a method to calculate the same result more quickly [24, 25].

The most well known FFT algorithms depend on the factorization of N. On the other side, even for prime N, there are FFTs with O(N log N) complexity for all N. Many FFT algorithms only rely on the fact that is an Nth primitive root of unity, and therefore can be applied to analogous transforms over any finite field which is such as number-theoretic transforms [24, 25].

The sequence of N numbers $x(1)$, ..., $x(N)$ is transformed into the sequence of N

numbers k=1,...,N by the FFT according to the following formula:

$$\mathbf{X}(k) = \sum_{j=1}^{N} \mathbf{x}(j)\omega_N^{(j-1)(k-1)}, \tag{2.37}$$

where $\omega_N = e^{(-2\pi i)/N}$ is the N_{th} root of unity.

Chapter 3

One-dimensional design

In this research, an application of ultra-wideband (UWB) radar through a wall of light construction for the remote measurement of the position and respiration of hidden persons is presented. The automatic system concept is based on the transmission of sub-nanosecond pulses to achieve the measurement of a human chest movement and processing the data immediately. For the signal processing a fast, robust and accurate method is recommended. The variations of the data and FIR filtering are used to calculate the distance after removing background distortions. This allows the detection of breath motions up to a distance of 4.75 meters behind a wall. The magnitude cycle rate in the summation of a various number of points is used to get the breath frequency. The results of this process which takes approximately 12 seconds are distance and breath frequency determination of the person. The measurement method, signal processing and practical results of tests are presented.

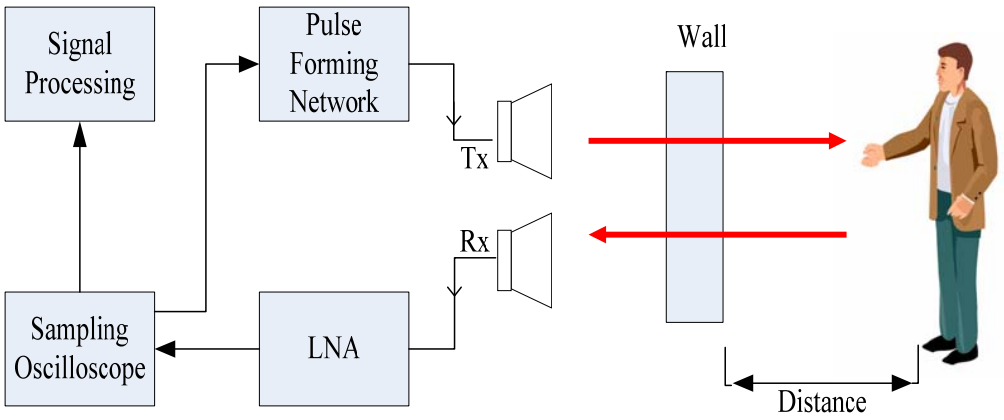

Figure 3.1: *Set-up breath movement detection measurement system.*

3.1 Measurement setup

An ultra wideband impulse radar test setup for generating real air/chest boundary reflection data was built. The block diagram of the implemented breath movement detection is shown in Figure 3.1. Generally, the constructed microwave life-detection system includes four major components [1–16]:

1. A generator and a pulse forming network which generates and amplifies the pulse to be transmitted.
2. An antenna system which consists of two or three separate antennas for transmitting and receiving signals.
3. A computer which controls the whole system and displays the results on the monitor.
4. A signal processing system which produces an optimal signal to remove the clutter caused from the wall and the background.

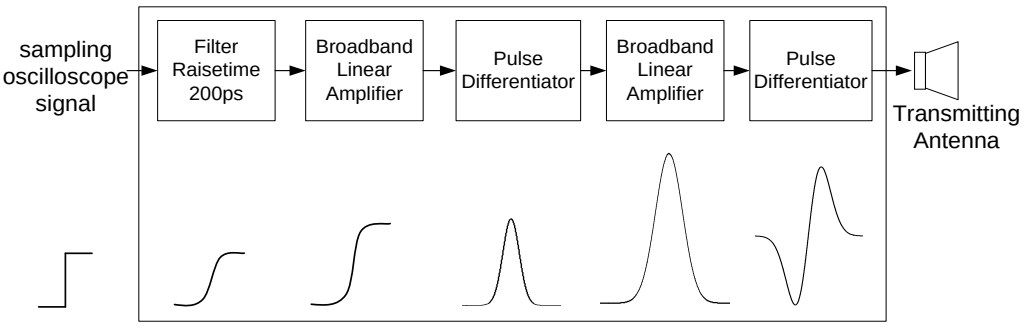

Figure 3.2: *Pulse forming network.*

For the pulse generator the *Tektronix TDS-8000* is used to generate a step pulse and acquires the measurement signal. The same oscilloscope with a bandwidth of 20 GHz is used for data acquisition. It is connected to a pulse forming network in order to produce a Gaussian pulse. The block diagram of the pulse forming network is shown in Figure 3.2.

The sampling oscilloscope signal is connected to the filter with a raise time of 200 ps. Then, the pulse passes the first amplifier, the first differentiator to create the Gaussian pulse, the second amplifier, the second differentiator for creating the 2^{nd} derivative of Gaussian pulse, and at the end the Gaussian signal can be transmitted by the transmitting antenna.

The output of the pulse forming network is connected to a UWB double-ridged horn antenna for transmitting the pulse. The output pulse has a pulse width about 600 ps, a peak to peak output voltage of 4.2 volts and a pulse repetition frequency of 200 kHz. The measured Gaussian pulse is shown in Figure 3.3.

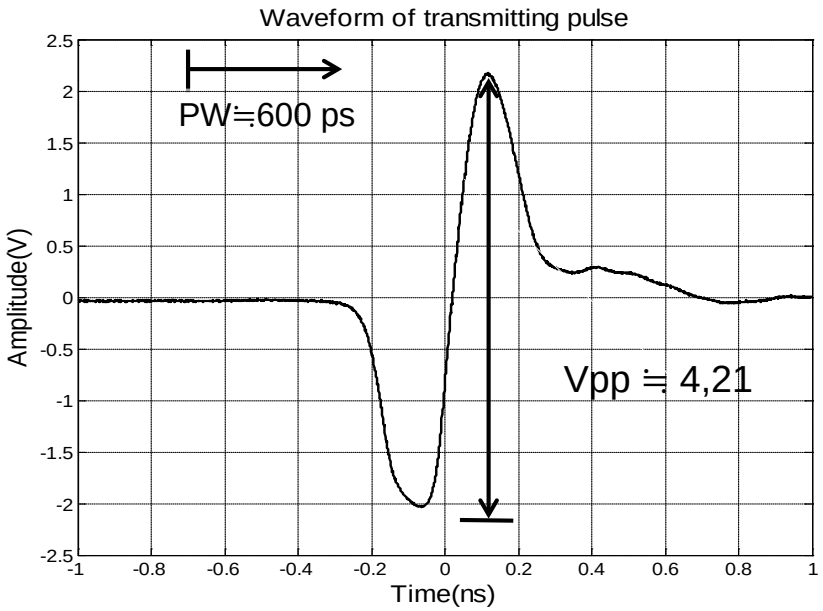

Figure 3.3: *Measurement signal consisting of Gaussian monocycles, fed directly into broadband antenna.*

The transmitting pulse touches the chest of a person whose breathing rate is 12-15 times/minute (0.2-0.25 times per second). The radiated pulse is reflected and received by another double-ridged horn antenna. The measurement set-up for breath detection is behind a wall of light construction having a thickness of 12 cm and the distance between the antennas and the wall is 53 cm.

The received signal is amplified by an amplifier which achieves a maximum gain of 26 dB from DC to 12.5 GHz. It is a broadband linear amplifier (Model 5865 from the company *Picosecond*). The sampling of the received signal is performed by the *Tektronix TDS-8000* sampling oscilloscope (t_s = 12.5 ps) too, which is triggered by the internal pulse generator. The time length of each record profile δ_τ is 50 ns. This implies that each waveform comprises $N = \frac{\delta_\tau}{t_s} = 4000$ sample points.

Every 100 ms an actual reflection measurement trace is captured for a total measurement time of 10 seconds. Therefore 100 data vectors are collected from each measurement.

The speed of an electromagnetic wave in the air is practically equal to the speed of light. The travelling speed of a wave differs in the varying materials of the wall. The travelling time in the same material but with different thickness is also not the same. In the following, equation 2.30 is transformed. The delay time (t_d) caused by the wave travelling in the wall should be considered. As assumed in air material, by equation 2.30, the travelling time in the air with a thickness w_n and an angle of incidence θ_i are determined as

$$TOA_c = \frac{w_n}{c}\left(\frac{1}{\cos\theta_i}\right). \tag{3.1}$$

For getting object data, the waves both for transmission and reception travel at various penetration angles. The effect of delay time in the wall compared to air can be described as subtracting equation 3.1 from equation 2.30

$$T_{delay} = \sum_{i=1}^{n}\left(\frac{w_n}{c}\right)\left(\frac{\epsilon_n}{\sqrt{\epsilon_n - \sin^2\theta_i}} - \frac{1}{\cos\theta_i}\right). \tag{3.2}$$

In our case, the angle range will be near to 0°. The range of delay time due to the wall can be computed as $t_d = 0.21662$ ns. That means, the travelling distance calculated directly from travelling time will have an error of 6.5 cm caused by the wall. After the pulse penetrates the wall it is reflected by the object. Then it penetrates the wall a second time and is received by the antennas. For more accuracy, the error of 6.5 cm will be subtracted twice from the round trip time.

3.2 Signal processing

3.2.1 Determination of position

With the presented UWB radar set-up, several breath movement measurements of a person at 15 different distances (1: 55 cm, 2: 85 cm, 3: 115 cm, 4: 145 cm, 5: 175 cm, 6: 205 cm, 7: 235 cm, 8: 265 cm, 9: 295 cm, 10: 325 cm, 11: 355 cm, 12: 385 cm, 13: 415 cm, 14: 445 cm and 15: 475 cm) behind a wall were made. The data of any point can be extracted from the original data which is measured by the receiving antenna. The data matrix $\mathbf{X}$ with size $m \times n$ is as a set of scalar quantities arranged in a rectangular array containing m rows and n columns. In other words, this array will be called a rectangular matrix of order m by n, or, briefly, an $m \times n$ matrix. The single matrix $\mathbf{X}$ can be described as

$$\mathbf{X} = \begin{bmatrix} x_{1,1} & x_{1,2} & \dots & x_{1,n} \\ x_{2,1} & x_{2,2} & \dots & x_{2,n} \\ x_{3,1} & x_{3,2} & \dots & x_{3,n} \\ \vdots & \vdots & \ddots & \vdots \\ x_{m,1} & x_{m,2} & \dots & x_{m,n} \end{bmatrix}, \tag{3.3}$$

where the quantities $x_{m,n}$ are called the entries or components of the matrix. In our measurement, they can also be described as the m^{th} data value of the n^{th} point.

The original reflected pulse plotted by the *Matlab* program is shown in Figure 3.4. It can be seen that the crosstalk is much higher than the reflection of the person. The reflection at the expected position is not observed clearly. An algorithm of

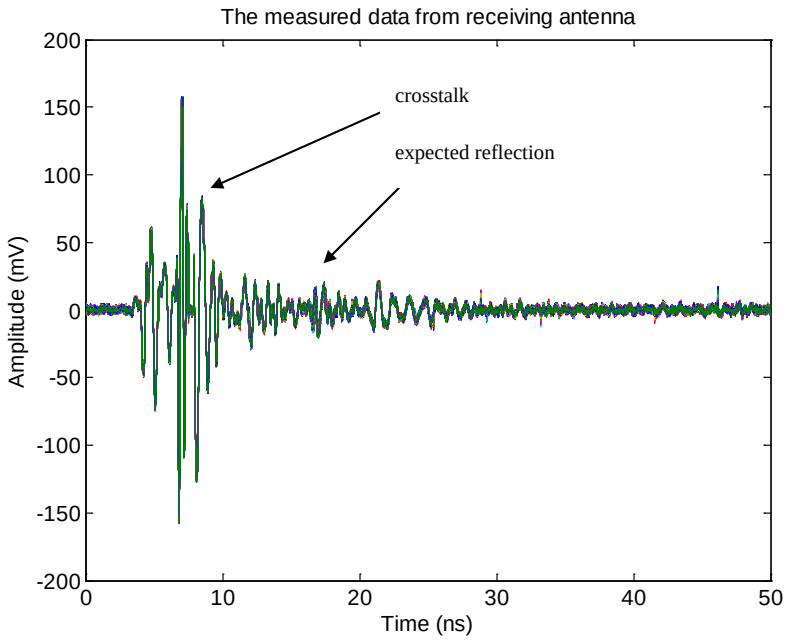

Figure 3.4: *Measured data from receiving antenna.*

signal processing was developed to process the measured data.

Firstly, there are two types of noise which need to be removed. Because obstacles are stationary in comparison to the chest movement, a moving average method is used to get the mean subtraction of the original data. The empirical mean along each dimension $n = 1, \ldots, N$, the calculated mean values were placed into a row vector $\mathbf{X}u_n$ of dimensions $1 \times N$ as

$$\mathbf{X}u_n = \frac{1}{M} \sum_{m=1}^{M} \mathbf{X}_{m,n}. \tag{3.4}$$

Then, with subtracting the mean vector $\mathbf{X}u_n$ from each column of the data matrix and storing mean-subtracted data in the matrix $\mathbf{A}$, the stationary part of the signal is removed. The data after this process can be expressed as

$$\mathbf{A}_{m,n} = \mathbf{X}_{m,n} - \mathbf{X}u_n. \tag{3.5}$$

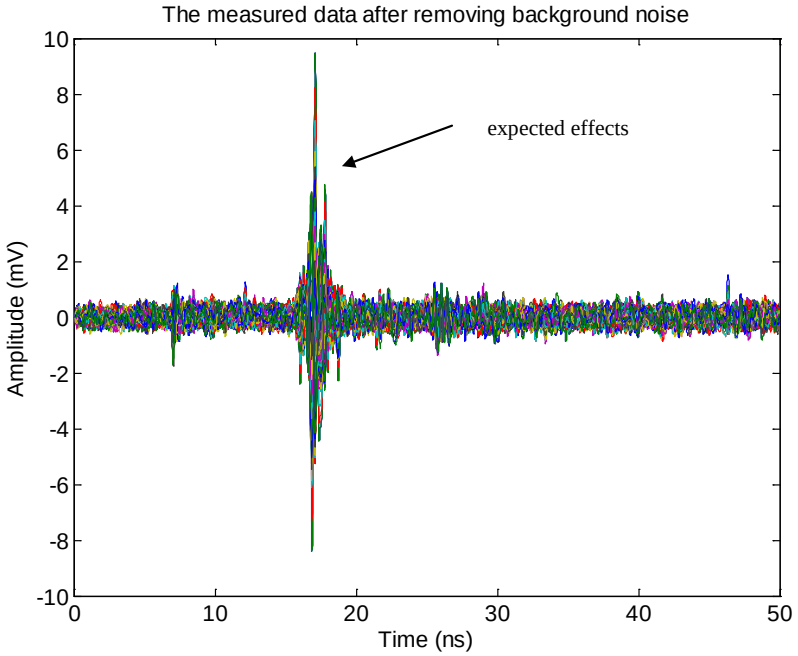

Figure 3.5: *Measured data after removing the background noise.*

After the method of mean-subtraction, a finite impulse response filter is used to remove the background noise. The filter is a linear-phase FIR digital filter with an order l. The filtered data can be written as

$$\mathbf{B}_{m,n} = \sum_{k=0}^{l} \mathbf{b}(k)\mathbf{A}_{m,(n-k)}, \tag{3.6}$$

where $\mathbf{b}(\mathbf{k})$ $k = 1, \ldots, l$ is a row vector containing the l+1 coefficients of an order l lowpass FIR filter. The coefficients are calculated using the *Matlab*. With the two methods, it is possible to find the expected data behind the noise. Hence they are robust. The expected effects can be seen in Figure 3.5. The parameters of the measurement including pulse length, sampling oscilloscope and reflection vectors are the same as described in chapter 3.1.

The signal of breath movement is clear and distortions were removed successfully.

Then, the unbiased variance of each column in the input over a period of time is computed to determine how large the differences are. Calculating the variance of each data column, the determined data of a row vector is defined as

$$\mathbf{C}_n = s^2 = \frac{\mathbf{1}}{M-1}\sum_{m=1}^{M}(\mathbf{B}_{m,n} - \overline{\mathbf{B}}_n)^2, \tag{3.7}$$

where

$$\overline{\mathbf{B}}_n = \frac{1}{M}\sum_{i=1}^{M}\mathbf{B}_{m,n}. \tag{3.8}$$

is the mean-value.

The variance data is shown in Figure 3.6. A finite impulse response (FIR) filtering is used again to get the moving average signal from the variance. This low-pass filters provide a smoother form of a signal, removing the short-term fluctuations, and leaving the longer-term trend. After this filtering, the data equation can be written to

$$\mathbf{D}_n = \sum_{k=0}^{\mathbf{n-1}}\mathbf{b}(k)\mathbf{C}_{n-k}. \tag{3.9}$$

See Figure 3.7, the position in time t_p of the peak of this signal, which is called the round trip time, can be found easily by a detection of the maximum. From equation 3.9, the index t_p of the maximum peak value can be determined exactly and can be written as

$$t_p = Max(\mathbf{D}_n). \tag{3.10}$$

With this determined time, and the subtraction of the double the delay time in the wall (approximately 0.13105 ns), the double short travelling time(STT) from antennas to and through the wall and the linear delay time (LDT) from the FIR

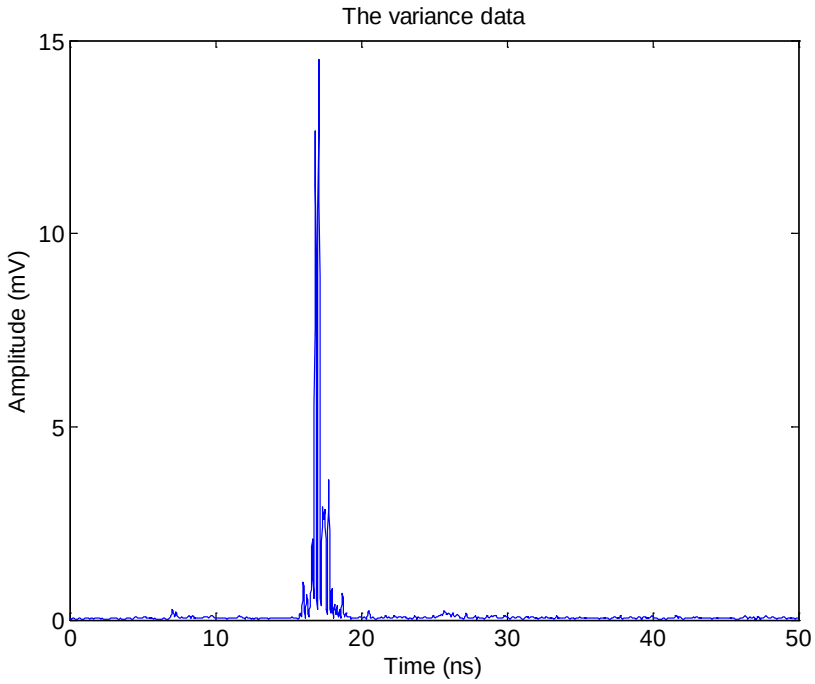

Figure 3.6: *Variance data.*

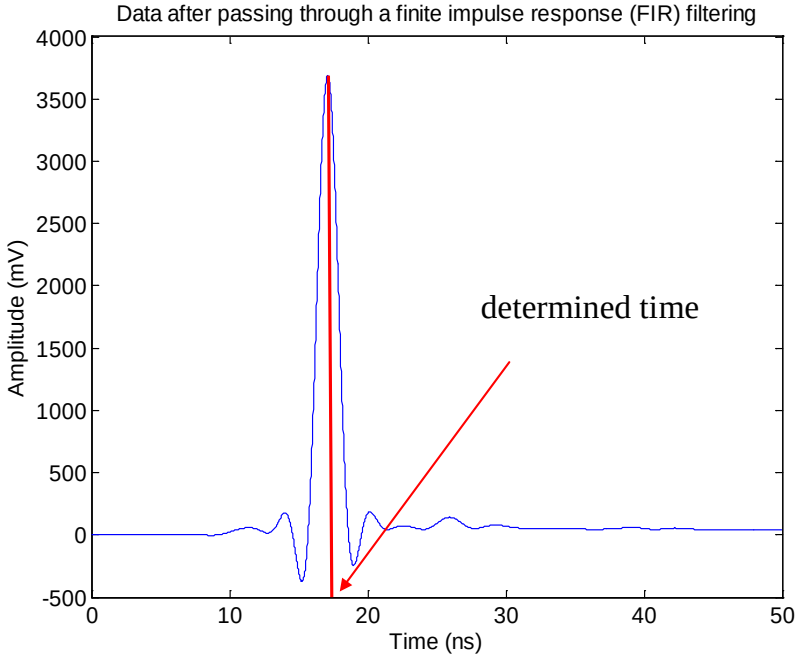

Figure 3.7: *Data after passing through a finite impulse response (FIR) filtering.*

filtering, the distances (d) of person can be determined by using the equation

$$d(cm) = \left((t_p - t_s) * 3 * 10^{10} cm/s\right)/2, \tag{3.11}$$

where

$$t_s = 2(0.21662 + STT) + LDT. \tag{3.12}$$

For example, a person is behind a wall at a distance of 115 cm. The position at time t_p which is 17.1 ns has been determined. In this work, the value of the STT is $65/(3 * 10^{10})$ ns and the LDT from filtering causes 5 ns linear phase shift. The predicted distance of 111 cm behind a wall has been determined by the equation 3.11. The maximum predicted distance up to 4.75 m was determined. In practical situations, the delay time t_d caused by the walls or obstacles could not be easy determined exactly before measurements. This will cause a measurement error. However, the principle of composition of the walls should be known and the delay time t_d should be estimated. Furthermore, t_d can be measured by the distance of the reflected pulses of the wall surfaces. But this is not discussed in detail here and the next measurements.

3.2.2 Determination of breath frequency

Furthermore, a way for the determination of the breath frequency was developed. The point "t_p" ns was obtained from equation 3.10 and set as a center point. The selected points(SP) 1, 3, 5, 7 in the affected area were chosen respectively. Points were selected at every 10 sample points (0.0125 ns) extending from both side of the center one. The defined positions of points (PP) according to the number of

Table 3.1: The definition of different selected points.

Numbers of selected points	Position of points(ns)
1	t_p
3	"t_p"-0.0125, "t_p" and "t_p"+0.0125
5	"t_p"-0.0125 × 2, "t_p"-0.0125, "t_p" ,"t_p"+0.0125 and "t_p"+0.0125 × 2
7	"t_p"-0.0125 × 3, "t_p"-0.0125 × 2,"t_p"-0.0125, "t_p", "t_p"+0.0125, "t_p"+0.0125 × 2 and "t_p"+0.0125 × 3

selected points (NSP) are shown in Table 3.1.

After removing the background, there are four thousand sample points in each row of measurement data as mentioned in the matrix $\mathbf{B}_{m,n}$. The equation of selected data can be defined to

$$\mathbf{G}_{m,n} = \mathbf{B}_n, \tag{3.13}$$

where

$$n = PP = t_p - 0.0125 * (NSP - 1)/2 + 0.0125 * \mathbf{BT}_p, \tag{3.14}$$

and

$$\mathbf{BT}_p = [0 : NSP - 1]. \tag{3.15}$$

A sample of three points in the affected area is shown in Figure 3.8. The amplitude change at any point in the affected area of the measured signals is proportional to the breath frequency.

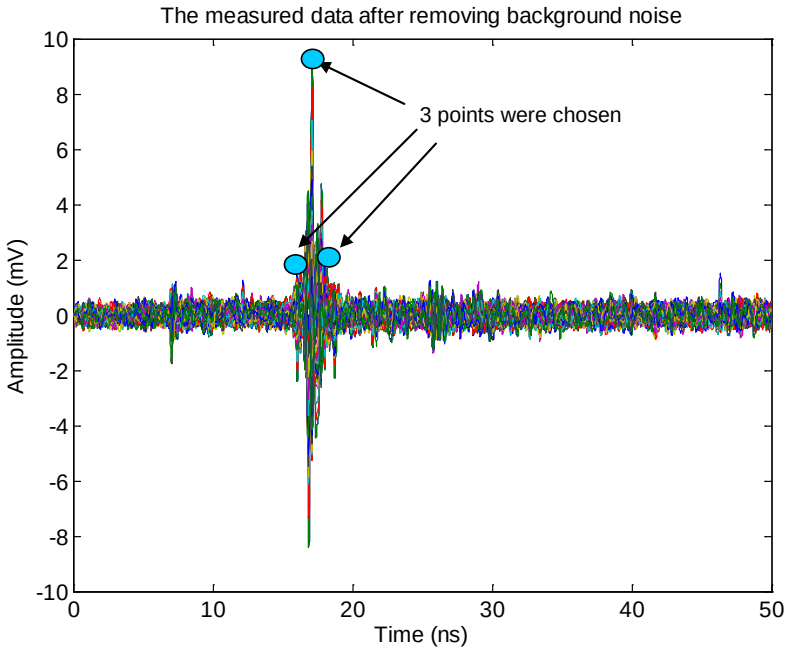

Figure 3.8: *Three points are chosen.*

Continuing from the previous sample, the three points ("t_p"-0.0125 ns, "t_p" and "t_p"+0.0125 ns) called p1, p2 and p3 were selected. Every point has 100 row values. From equation 3.13, the matrix **H** with 3 selected points and size 100×3 can be written

$$\mathbf{H} = \begin{bmatrix} h_{1,1} & h_{1,2} & h_{1,3} \\ h_{2,1} & h_{2,2} & h_{2,3} \\ h_{3,1} & h_{3,2} & h_{3,3} \\ \vdots & \vdots & \vdots \\ h_{100,1} & h_{100,2} & h_{100,3} \end{bmatrix}, \tag{3.16}$$

where $\mathbf{h}_1$, $\mathbf{h}_2$ and $\mathbf{h}_3$ are extracted from the n^{th} data value of the points 1, 2 and 3 respectively.

The matrix **S** with the size 3×100 is derived by the transpose operation of **H**:

$$\mathbf{S} = \begin{bmatrix} s_{1,1} & s_{1,2} & \dots & s_{1,100} \\ s_{2,1} & s_{2,2} & \dots & s_{2,100} \\ s_{3,1} & s_{3,2} & \dots & s_{3,100} \end{bmatrix}. \tag{3.17}$$

For each point chosen, the extracted data of each row of **S**, similar characteristics of the time of the magnitude cycle over 10 seconds can be computed as shown in Figure 3.9. In this figure, it is not easy to identify the frequency components by looking at the original signal. The discrete Fourier transform of the signal amplitude is for the conversion into the frequency domain, by taking the fast Fourier transform (FFT) as mentioned in chapter 2.5.4. The FFT equation 2.37 can be be written here again to the following formula

$$\mathbf{X}(k) = \sum_{q=1}^{Q} \mathbf{x}(q)\omega_Q^{(q-1)(k-1)}, \tag{3.18}$$

where $\omega_Q = e^{(-2\pi i)/Q}$ is an Q_{th} root of unity.

Then, the FFT of each row of **S** can be described as

$$\mathbf{S}(k) = \sum_{q=1}^{Q} \mathbf{S}(q)\omega_Q^{(q-1)(k-1)}. \tag{3.19}$$

For each selected point (each column), the breath frequency can be determined from the magnitude in the same way. The mean data of the breath frequencies of three points for an observation time of 10 seconds is shown in Figure 3.10.

The mean equation of the $\mathbf{S}_{p,q}$ can be determined as

$$\mathbf{T}_q = \frac{1}{P} \sum_{p=1}^{P} \mathbf{S}_{p,q}, \tag{3.20}$$

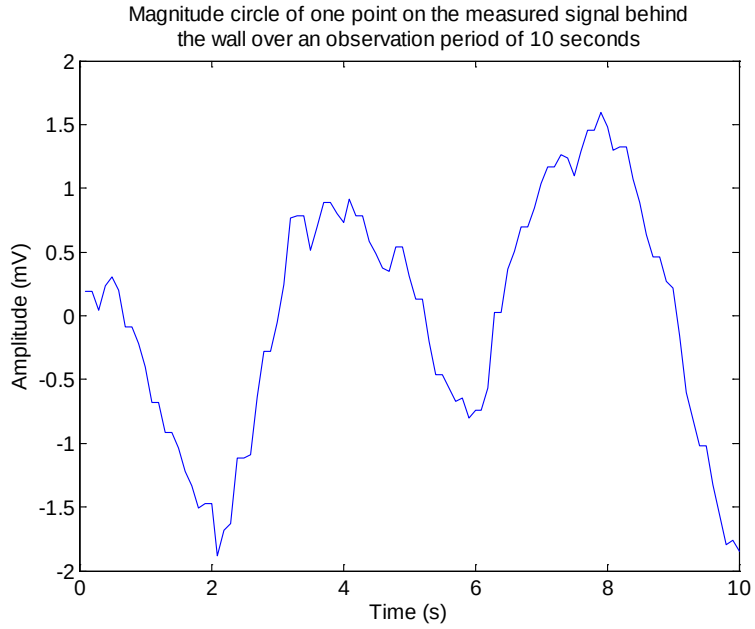

Figure 3.9: *Magnitude circle of one point on the measured signal behind the wall over an observation period of 10 seconds.*

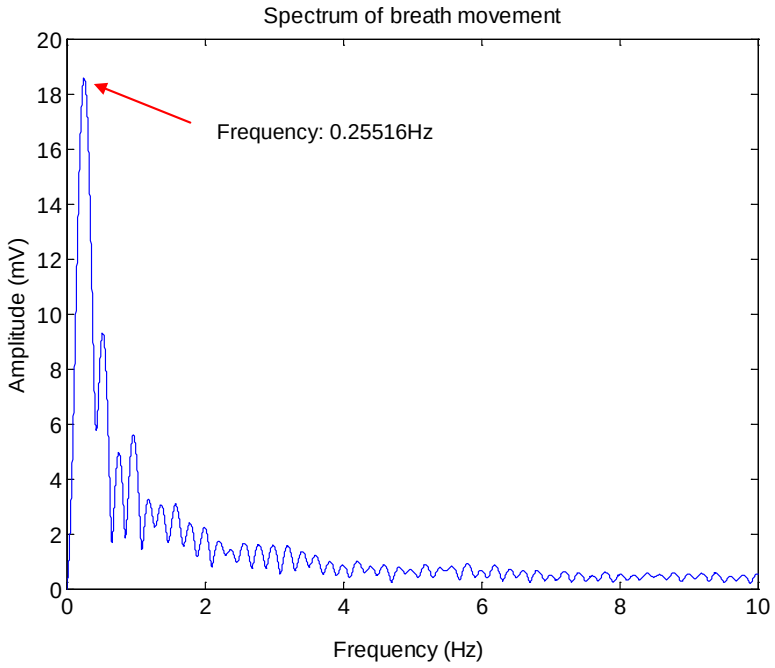

Figure 3.10: *Breath frequency determined by using the mean of the fast Fourier transforms from the magnitude changes of three points.*

where $1 \leq q \leq Q$, $\mathbf{T}_q$ is a row vector with size $1 \times Q$.

The maximum value of the matrix $\mathbf{T}$ can be obtained as equation

$$\mathbf{Y} = Max(\mathbf{T}_q). \tag{3.21}$$

In Figure 3.10, a waveform with a zero DC component is known as a DC-balanced waveform. The DC-component, the mean value of the waveform, is removed. The breath frequency of 0.25516 Hz was determined. The distance 111 cm of the hidden human was also determined as mentioned in the same section. The whole process of life detection in this case is also done automatically. The results of this process which takes around 12 seconds are distance and breath frequency determination of the person.

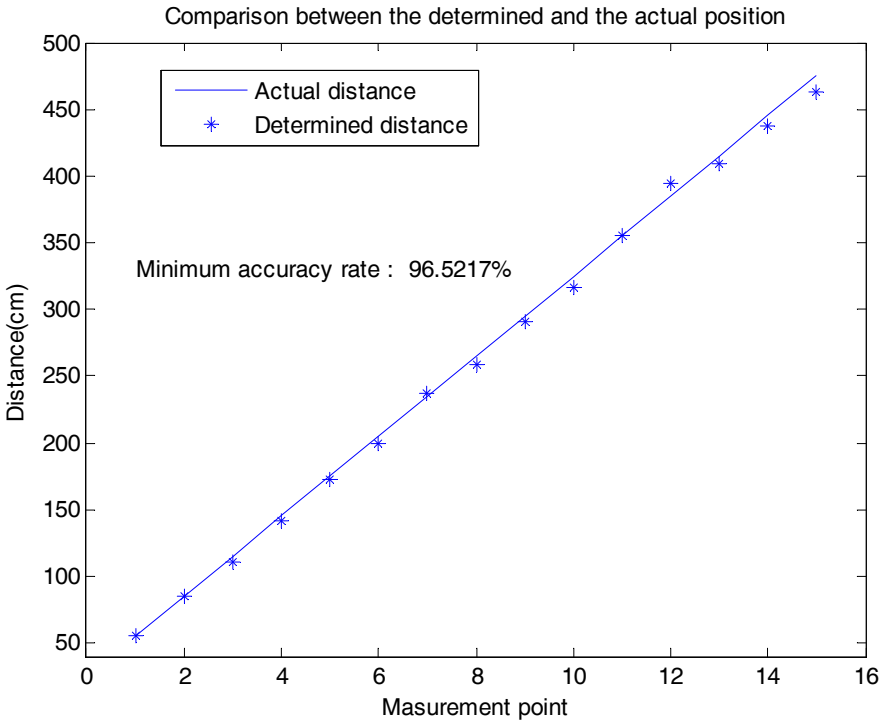

Figure 3.11: *Comparison of determined (*) and actual (solid) distance with 15 distances behind the wall from 0.55 m to 4.75 m.*

3.3 Results

Figure 3.11 shows the comparison of the actual and determined distances of the person behind the wall. The minimum accuracy is determined by the function $Accuracyrate = \frac{1-|a-p|}{a}$, where a is the actual distance, p is the determined distance. The minimum accuracy rate between the actual and determined distances is clearly over 96%.

Furthermore, according to the magnitude cycle rate, the breath frequencies can be determined with different distances and number of points. Figure 3.12 shows frequencies which are determined by the average of different points. The signs

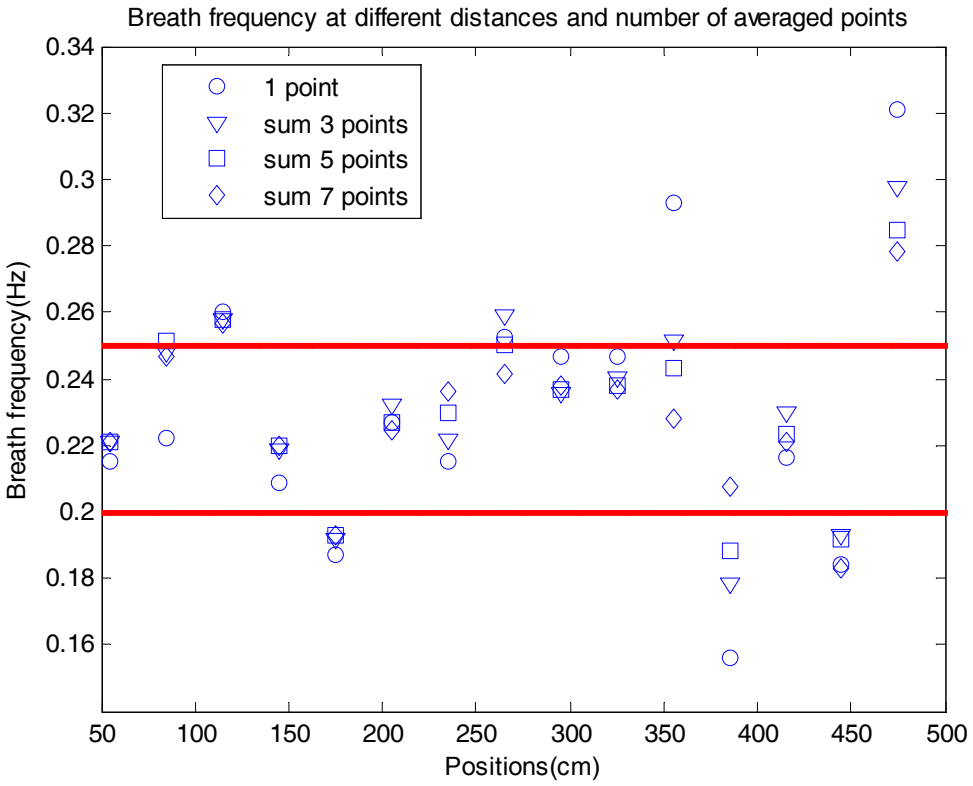

Figure 3.12: *Determined breath frequency at different distances and number of averaged points.*

◯, ▽, □ and ◇ express the number of averaged 1, 3, 5, 7 points respectively. The two parallel lines in breath frequency 0.2 and 0.25 Hz are the human frequencies as mentioned in chapter 3.1. The comparison of frequencies of different points shows that the accuracy improves towards the real frequency of 0.2 to 0.25 Hz with the number of points. In other words, the measurement with 7 points is better than the others. It will be used for further measurements. The details of the determined breath frequency at different distances and numbers of averaged points is shown in Table 3.2 and Table 3.3.

Table 3.2: Determined breath frequency at different distances (55-235cm) and number of averaged points.

Real distance (cm)	Number of points	Predicted breath frequency(Hz)	Mean error (Hz)
55	1	0.2149	0
55	3	0.2210	0
55	5	0.2210	0
55	7	0.2210	0
85	1	0.2222	0
85	3	0.2478	0
85	5	0.2515	0.0015
85	7	0.2466	0
115	1	0.2600	0.01
115	3	0.2576	0.0076
115	5	0.2576	0.0076
115	7	0.2564	0.0064
145	1	0.2088	0
145	3	0.2185	0
145	5	0.2198	0
145	7	0.2198	0
175	1	0.1868	0.0132
175	3	0.1917	0.0083
175	5	0.1929	0.0071
175	7	0.1929	0.0071
205	1	0.2271	0
205	3	0.2320	0
205	5	0.2271	0
205	7	0.2246	0
235	1	0.2154	0
235	3	0.2215	0
235	5	0.2300	0
235	7	0.2361	0

Table 3.3: Determined breath frequency at different distances (265-475 cm) and number of averaged points.

Real distance (cm)	Number of points	Predicted breath frequency(Hz)	Mean error (Hz)
265	1	0.2527	0.0027
265	3	0.2588	0.0088
265	5	0.2503	0.0003
265	7	0.2417	0
295	1	0.2466	0
295	3	0.2356	0
295	5	0.2368	0
295	7	0.2381	0
325	1	0.2466	0
325	3	0.2405	0
325	5	0.2381	0
325	7	0.2368	0
355	1	0.2930	0.043
355	3	0.2515	0.0015
355	5	0.2429	0
355	7	0.2283	0
385	1	0.1563	0.0437
385	3	0.1782	0.0218
385	5	0.1880	0.012
385	7	0.2075	0
415	1	0.2161	0
415	3	0.2295	0
415	5	0.2234	0
415	7	0.2210	0
445	1	0.1843	0.0167
445	3	0.1929	0.0071
445	5	0.1917	0.0083
445	7	0.1831	0.0169
475	1	0.3211	0.0711
475	3	0.2979	0.0479
475	5	0.2845	0.0345
475	7	0.2784	0.0284

Chapter 4

Two-dimensional measurement

An application of UWB radar through a wall of light construction for remote measuring of the two-dimensional position and respiration of hidden persons is discussed in this chapter. The automatic system concept and signal processing was recommended as described in chapter 3. A zero-phase FIR filtering instead of finite impulse response (FIR) filtering is used to calculate the distance without linear phase shift after removing background distortions. The magnitude cycle rate in the summation of various numbers of points is used to get the breath frequency. Two receiving antennas get two breath frequencies. Averaging these two frequencies is used to determine the frequency of the human person. Four different kinds of setups were used and the accuracy was determined. The total measuring time from start command to finish measurement is approximately 44 seconds. The measurement method, signal processing and practical results of tests are presented.

4.1 Measurement setup

The one-dimensional system was introduced in chapter 3. The system is fast, robust and accurate. In a real application, it is fast and suitable to search a given area quickly. The two-dimensional system was developed to also detect the location and breath frequency of a hidden person.

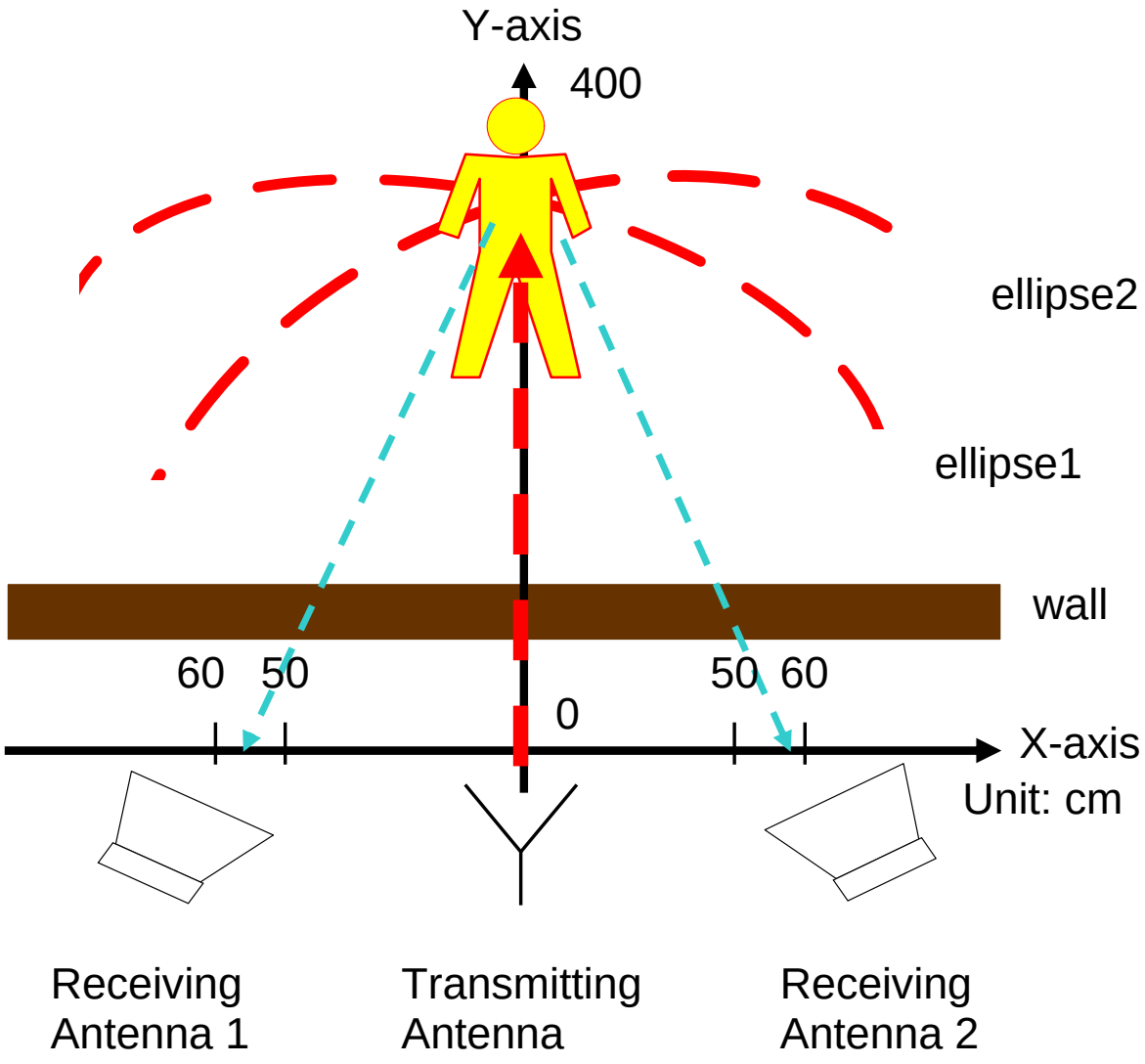

Figure 4.1: *Geometrical setup for two-dimensional measurement.*

Figure 4.1 shows the geometrical setup of the measurement. One transmitting antenna and two receiving antennas are used to detect the chest movement of a person behind the wall. The transmitting antenna shown on the X-axis, transmits a signal which penetrates the wall and touches the person. The reflected signals return to two receiving antennas after different times depending on the position. The receivers are put on the left and right hand side of the transmitting antenna at a distance of 60 cm. The travelling time from the transmitter to the person and back to the receiving antennas is calculated. Because of the receiving antennas' separation, the illuminated person is located on the elliptically-shaped curves with the antennas as the focus. The sum of the distances from any point on the curve of an ellipse to the two focal points is constant. There are two ellipse functions. The position of the person is calculated from an intersection of these two functions. In addition, according to the travelling time, the breathing frequency of the person is calculated using the magnitude cycle caused by the chest movement.

In order to observe the results step by step with the amplitude of the reflected signal getting weaker little by little, four types of environments for the two-dimensional measurements were set up and shown in Figure 4.2. In the first type, a tin plate in front of the chest of the person is used. The tin plate moves with the chest of the person. The tin plate is directly detected. In the second type, the detection is tested directly on the chest of the person. In the third type, the detection through a small wood board of a thickness of 2 cm between the antennas and the person is tested. The transmitted pulse penetrates the thin wall and is reflected by the person. In the first to third step, measurements are made at different positions. The maximum distance limited by our laboratory is 350 cm.

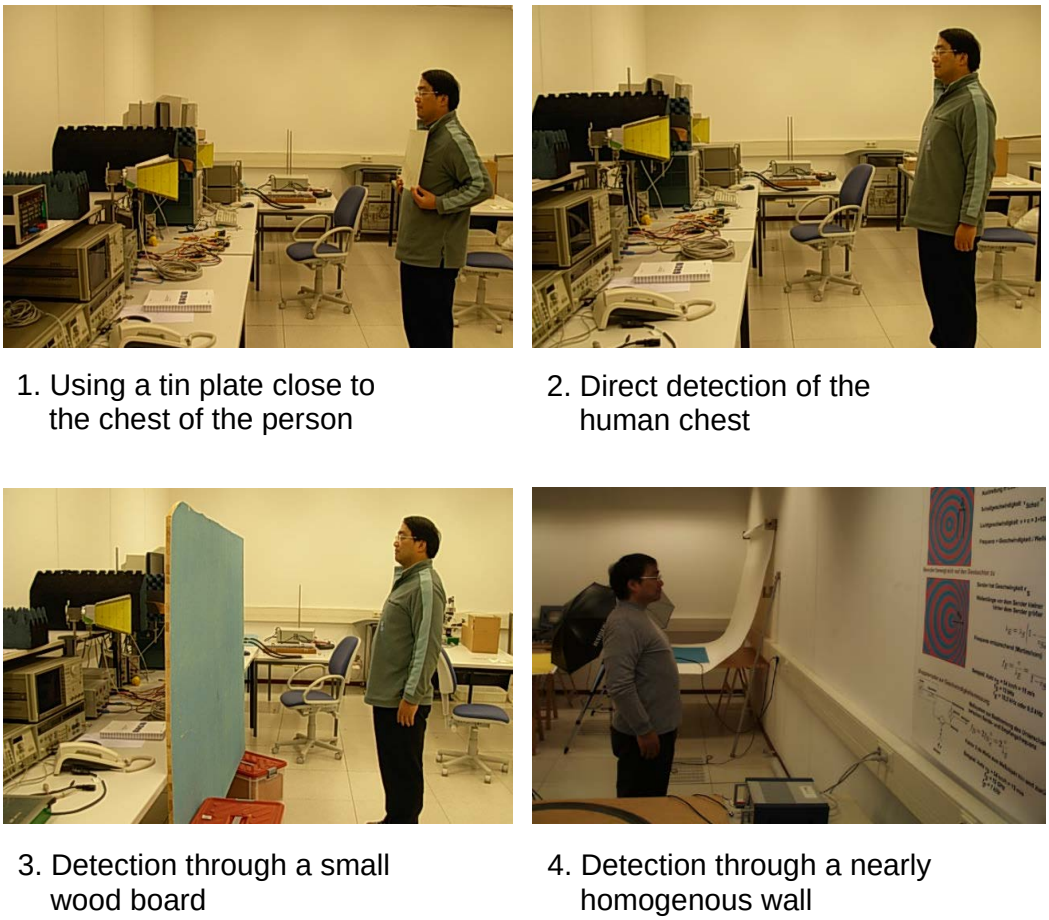

Figure 4.2: *Four types of measurement setups.*

In the last type, the detection is tested at a certain distance close to a homogenous wall between the antennas and the person. The thickness of the wall is 12 cm and the maximum measurement distance is 400 cm.

An ultra wideband impulse radar test setup was built for generating real air/chest boundary reflection data. The block diagram of the measurement set-up is shown in Figure 4.3. A pulse generator is used to generate a step pulse. But the transmitting antenna can not transmit the DC pulse as mentioned in chapter 3.1. It is necessary to connect a pulse forming network to produce a Gaussian pulse and

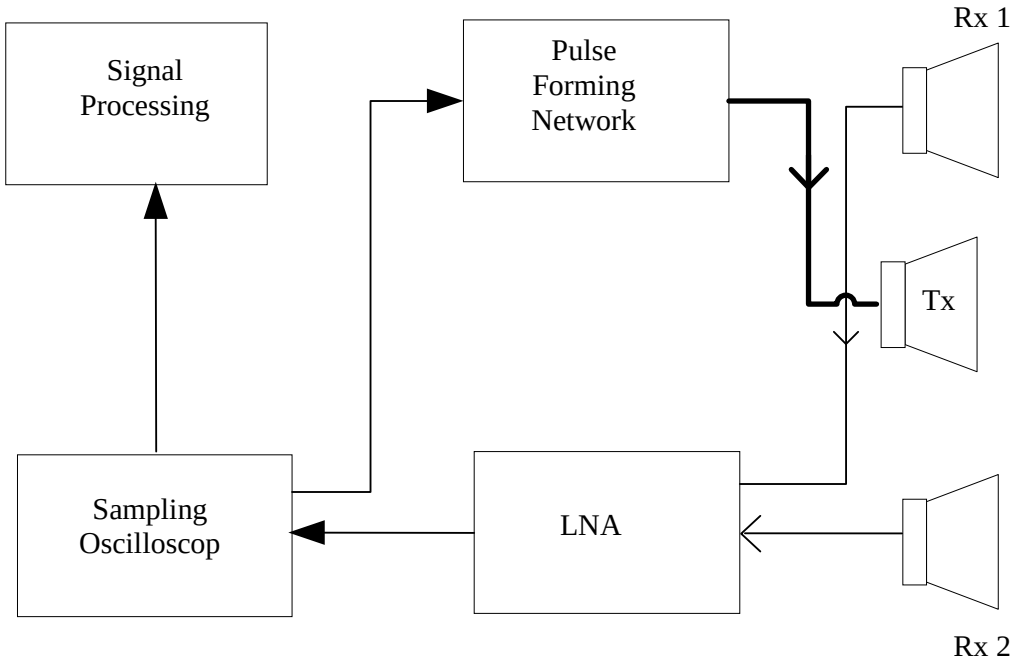

Figure 4.3: *Block diagram of measurement setup.*

connect a UWB Vivaldi antenna to transmit the pulse. Two receiving antennas are set up on different sides of the transmitting antenna. One of them will receive the reflected signals first and save it. Then, the other one will follow. After that, the signals will be processed immediately.

The output of the pulse forming network which is shown in chapter 3 is connected to a Vivaldi antenna for transmitting the pulse. The Vivaldi antenna is an ideal type of antenna used for EM beamforming. High directivity is important for focusing most of the radiated energy in well-controlled beams. To transmit short-duration Gaussian pulses, the wide bandwidth of the antenna is crucial for reducing distortions. The antenna is a useful configuration because of its simplicity, wide bandwidth, and high gain at microwave frequencies. The output pulse

has a pulse width of 600 ps, a peak to peak output voltage of 4.2 volts and a pulse repetition frequency of 200 KHz. The Gaussian pulse is the same as the previous measurement shown in Figure 3.3.

The transmitting pulse touches the chest of person whose breathing rate is 12-15 times/minute (0.2-0.25 times per second). The radiated pulse is reflected and received by double-ridged horn antennas. There are two antennas which receive the reflected data independently. The received signal is amplified by the same amplifier as discussed in chapter 3. The *Tektronix TDS-8000* sampling oscilloscope (t_s = 12.5 ps) is triggered by the internal pulse generator. Every 100 ms an actual reflection measurement trace is captured for a total measurement time of 20 seconds. Therefore 200 data vectors are collected from each measurement.

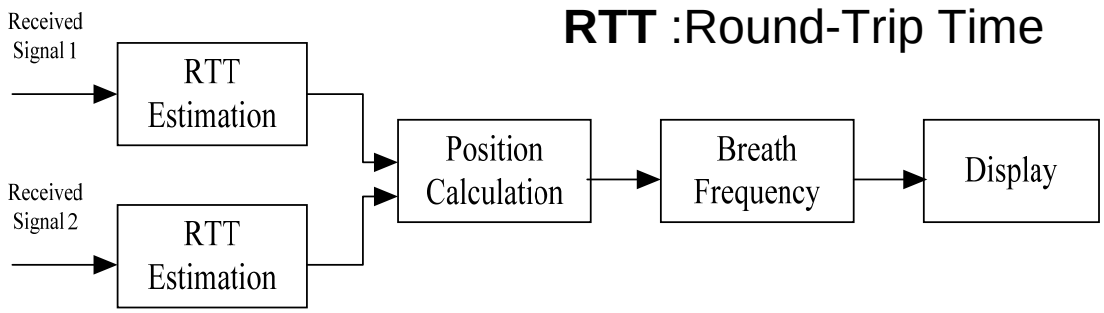

Figure 4.4: *Block diagram of signal processing.*

4.2 Signal processing

4.2.1 Calculation of the position

Figure 4.4 shows the block diagram of signal processing for position and breath frequency detection. When two receiving antennas receive data from the chest of the person, one can get the round trip time, the position and frequency by a mathematical processing which is successfully used in the previous chapter. The results can be displayed on the screen of a computer.

As mentioned in chapter 3.2, the speed of an electromagnetic wave in air is equal to the speed of light. The travelling speed is different when the wave enters into a wall of varying materials. The delay time caused by the wave travelling in the wall should be considered. For getting object data in two dimensions, the waves both for transmission and reception travel at varying penetration angles. By equation 2.30 the travelling time can be calculated. The effect of delay time in the wall compared to air can be described as

$$T_{delay} = \sum_{i=1}^{n} \left(\frac{w_n}{c}\right)\left(\frac{\epsilon_n}{\sqrt{\epsilon_n - \sin^2\theta_i}} - \frac{1}{\cos\theta_i}\right). \tag{4.1}$$

In our case, the angle range will be 0° to 45°. The range of delay time due to the wall can be computed as 0.13105 to 0.21662 ns. That means, the travelling distance calculated directly from travelling time will have an error of 3.93 to 6.50 cm caused by the wall. After the pulse penetrated the wall it is reflected by the object. Then it penetrates the wall a second time and is received by the antennas. The mean delay time is about 0.17384 ns. For more accuracy, it will be subtracted twice from the round trip time.

With the presented UWB radar set-up, several breath movements in a given area with four types of measurements are made. An example of the original reflected pulses of a person behind a near homogenous wall measured by the receiving radar is shown in Figure 4.5.

Because the transmitting and receiving signals penetrate the wall at a bigger angle than in one-dimensional measurement, the disorder of the crosstalk is wider. The crosstalk is also much higher than the reflection in the original data. The expected signal is not observed clearly. A *Matlab* program was therefore developed to process the measured signal. Firstly, a mean subtraction method is used to remove the mean value part of the original data $\mathbf{X}$. The single matrix $\mathbf{X}$ of dimensions $M \times N$ with column vectors $\mathbf{X_1} \ldots \mathbf{X}_N$, each of which has M rows, can be described as the same as equation 3.3. After the mean-subtraction, the data can be defined

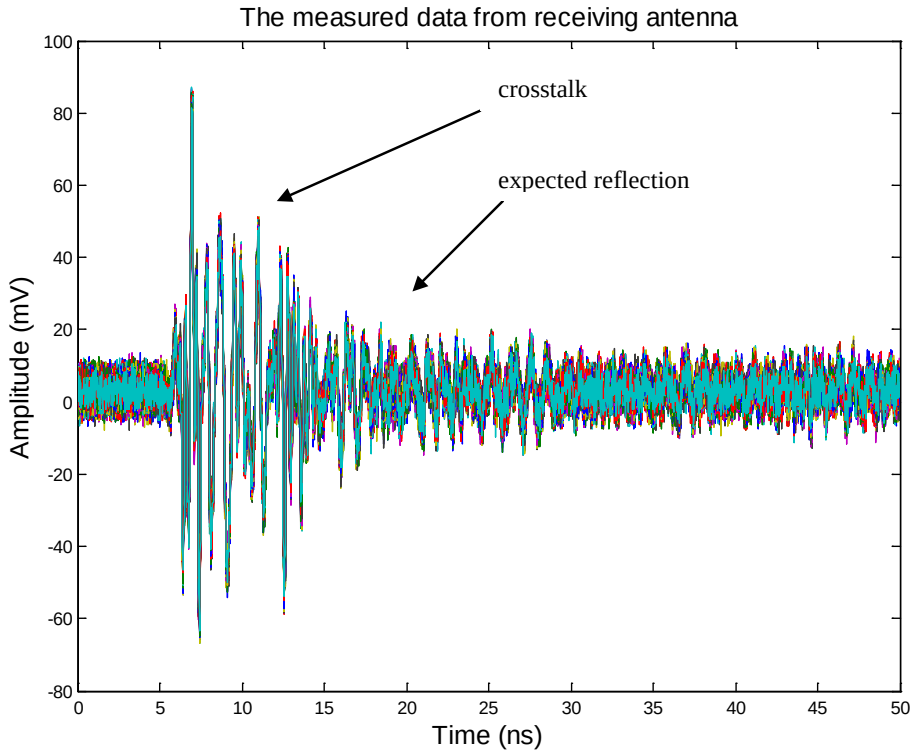

Figure 4.5: *Measured data from receiving antenna.*

as the same as equation 3.5

$$\mathbf{A}_{m,n} = \mathbf{X}_{m,n} - \mathbf{X}u_n, \tag{4.2}$$

where

$$\mathbf{X}u_n = \frac{1}{M}\sum_{m=1}^{M}\mathbf{X}_{m,n}. \tag{4.3}$$

Then, a zero phase low pass filtering with an orders l is used to remove background noise. The digital filtering performs by processing the input data, in both the forward and reverse directions. The result has the characteristics of zero-phase distortion, a filter transfer function which equals to the squared magnitude of the original filter transfer function. After filtering the data in the forward direction, the filtered sequence reverses and runs back through the filter. It is also possible

and robust to find the expected signal behind the noise, as with the method mentioned in chapter 3.2. The effect can be seen in Figure 4.6 and the equation can be written as

$$\mathbf{B}_{m,n} = \sum_{k=-l}^{l} \mathbf{b}(k)\,(\mathbf{A}_{m,n-k})\,, \tag{4.4}$$

where the vector $\mathbf{b}(k)$ $k = -l, \ldots, l$ provides the denominator coefficients. Hence $\mathbf{b}(k) = \mathbf{b}(-k)$, equation 4.4 can be rewritten as

$$\mathbf{B}_{m,n} = b_0 + 2\sum_{k=1}^{l} \mathbf{b}(k)\,(\mathbf{A}_{m,n-k})\,. \tag{4.5}$$

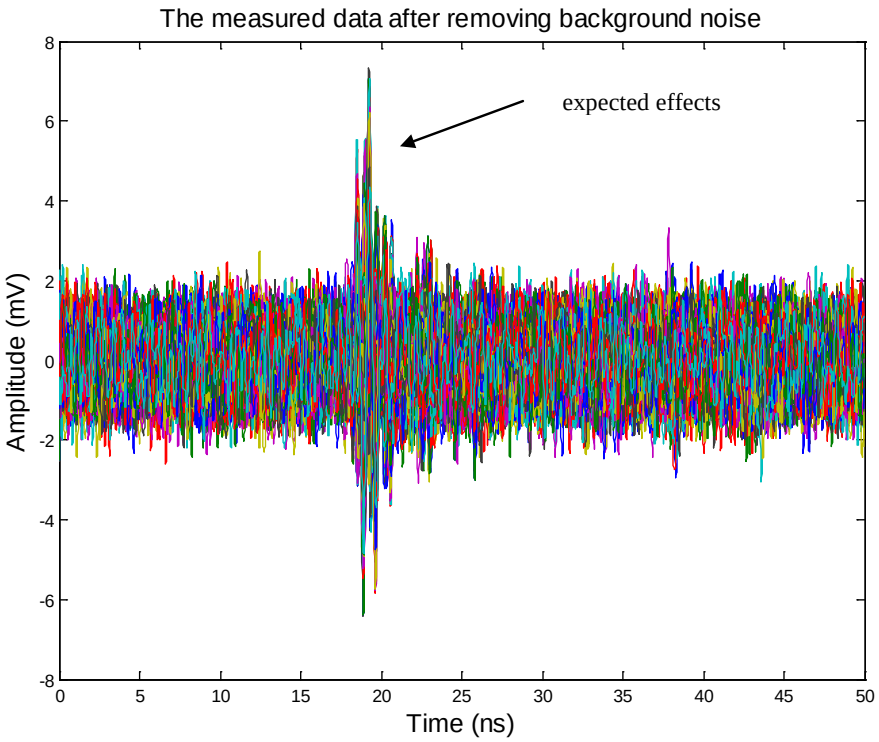

Figure 4.6: *Measured data after removing background noise.*

The signal of breath movement is clear. Then, the unbiased variance of each column in the input over a period of time is computed to determine how large

the differences are. Calculating the variance of each data column, the determined data of a row vector is defined as

$$\begin{aligned}\mathbf{C}_n &= s^2 \\ &= \frac{\mathbf{1}}{M-1}\sum_{m=1}^{M}(\mathbf{B}_{m,n} - \overline{\mathbf{B}}_n)^2, \end{aligned} \tag{4.6}$$

where

$$\overline{\mathbf{B}}_n = \frac{1}{M}\sum_{i=1}^{M}\mathbf{B}_{m,n}. \tag{4.7}$$

The variance data, which is more distorted than in the one-dimensional measurement, is shown in Figure 4.7. A zero-phase finite impulse response (FIR) filtering is used to get the moving average wave without a linear phase shift from variance. This low-pass filter provides a smoother form and zero-phase distortion of a signal, removing the short-term fluctuations, and leaving the longer-term trend. The equation 4.6 can be written to

$$\mathbf{D}_n = \sum_{k=0}^{\mathbf{n-1}}\mathbf{b}(k)\mathbf{C}_{n-k}. \tag{4.8}$$

See Figure 4.8, the position in time (t_p) ns of the peak of this wave, which is called the round trip time, can be found easily by a detection of the maximum. The position in time (t_p) ns of the peak of that wave can be found easily.

From equation 4.8, the maximum peak value is shown in Figure 4.8 and it can be determined exactly. The value of the t_p can be written as same as equation 3.10

$$t_p = Max(\mathbf{D}_n). \tag{4.9}$$

As mentioned in chapter 3.2, after subtracting some factor(t_s), double of the delay time in the wall (around 0.17384 ns), double of the short travelling time(STT) from

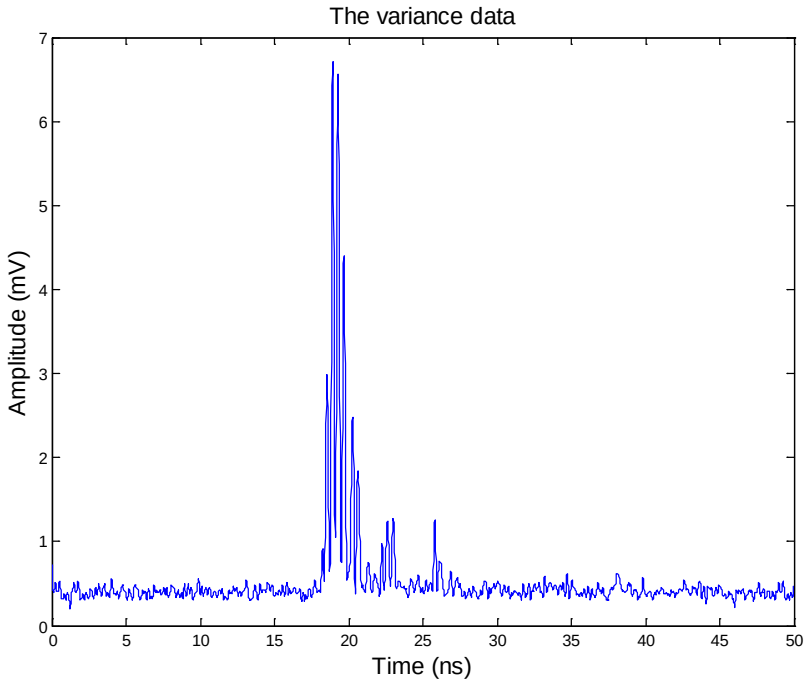

Figure 4.7: *Variance data of the signal.*

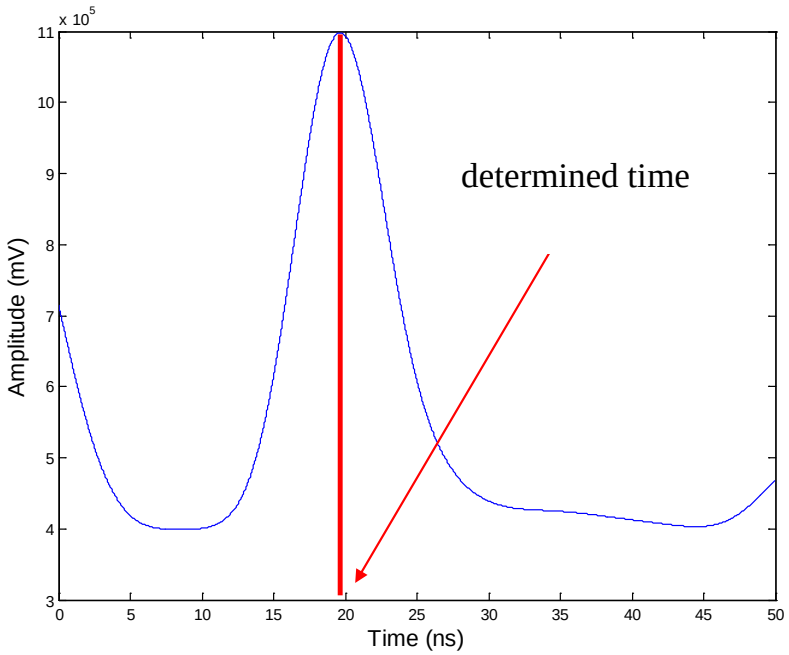

Figure 4.8: *Data after passing a zero-phase with FIR filtering.*

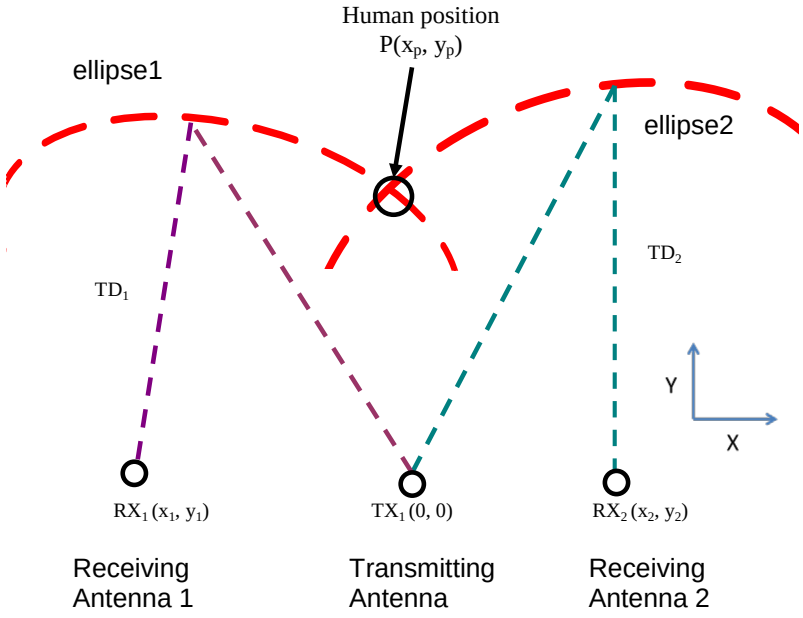

Figure 4.9: *The human position.*

antennas to and through the wall, the trip distance (TD) from the transmitting antenna to the person and back to the receiving antenna is determined from the equation

$$TD(cm) = \left((t_p - t_s) * 3 * 10^{10} cm/s\right)/2, \tag{4.10}$$

where

$$t_s = 2(0.17384 + STT). \tag{4.11}$$

As mentioned in chapter 4.1, because two measurements are received from two receiving antennas, two ellipse equations are determined from travelling distance. The position of the object is found at the intersection of the two ellipse functions. The detection of human position is shown in Figure 4.9.

As can be seen in this figure, it is necessary to measure the distance from the point of signal reception to the human from two different places (x_1, y_1) and (x_2, y_2), the

human position is defined to be $P(x_p, y_p)$, the transmitting antenna is at the origin of the coordinate system (0, 0) and the signals are received at different antennas. The respective trip distances (TD) are TD_1 and TD_2. Then the following equations hold

$$TD_1 = \sqrt{x_p^2 + y_p^2} + \sqrt{(x_1 - x_p)^2 + (y_1 - y_p)^2}, \tag{4.12}$$

and

$$TD_2 = \sqrt{x_p^2 + y_p^2} + \sqrt{(x_2 - x_p)^2 + (y_2 - y_p)^2}. \tag{4.13}$$

Here, because all terms other than the human position are measured values, $P(x_p, y_p)$ can be determined from the solution of the simultaneous equations 4.12 and 4.13.

4.2.2 Breath Frequency

Furthermore, a way to determine the breath frequency was developed. At any point in the affected area the magnitude cycle rate corresponds to the breath frequency. The definition positions of different selected points are shown as the same as Table 3.1. Because seven points are better than 1, 3 and 5 points as recommend in chapter 3.3, a sample of seven points in the affected area is chosen for this signal processing and shown in Figure 4.10.

According to equation 3.13, the seven points "t_p"-0.0125 × 3, "t_p"-0.0125 × 2,"t_p"-0.0125, "t_p", "t_p"+0.0125, "t_p"+0.0125 × 2 and "t_p"+0.0125 × 3 are the column number of the matrix 4.5. Every point has 200 row values. Therefore, the **H** with 7 points

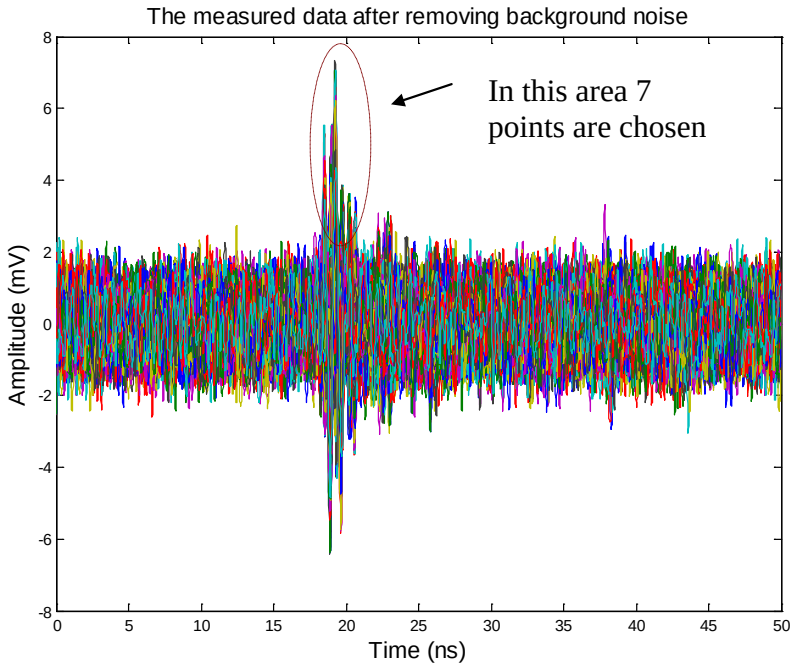

Figure 4.10: *Seven points are chosen.*

and size 200×7 can be written as

$$\mathbf{H} = \begin{bmatrix} h_{1,1} & h_{1,2} & \dots & h_{1,7} \\ h_{2,1} & h_{2,2} & \dots & h_{2,7} \\ h_{3,1} & h_{3,2} & \dots & h_{3,7} \\ \vdots & \vdots & \ddots & \vdots \\ h_{m,1} & h_{m,2} & \dots & h_{m,7} \end{bmatrix}. \tag{4.14}$$

The matrix $\mathbf{S}$ with size 7×100 is denoted by transpose operation of the matrix $\mathbf{H}$.

The transposed matrix can be determined

$$\mathbf{S} = \begin{bmatrix} s_{1,1} & s_{1,2} & \dots & s_{1,100} \\ s_{2,1} & s_{2,2} & \dots & s_{2,100} \\ s_{3,1} & s_{3,2} & \dots & s_{3,100} \\ s_{4,1} & s_{4,2} & \dots & s_{4,100} \\ s_{5,1} & s_{5,2} & \dots & s_{5,100} \\ s_{6,1} & s_{6,2} & \dots & s_{6,100} \\ s_{7,1} & s_{7,2} & \dots & s_{7,100} \end{bmatrix}. \tag{4.15}$$

For each chosen point, the extracted data of each row of **S** which has the similar characteristics of the time of the magnitude cycle rate over 20 seconds can be plotted as shown in Figure 4.11.

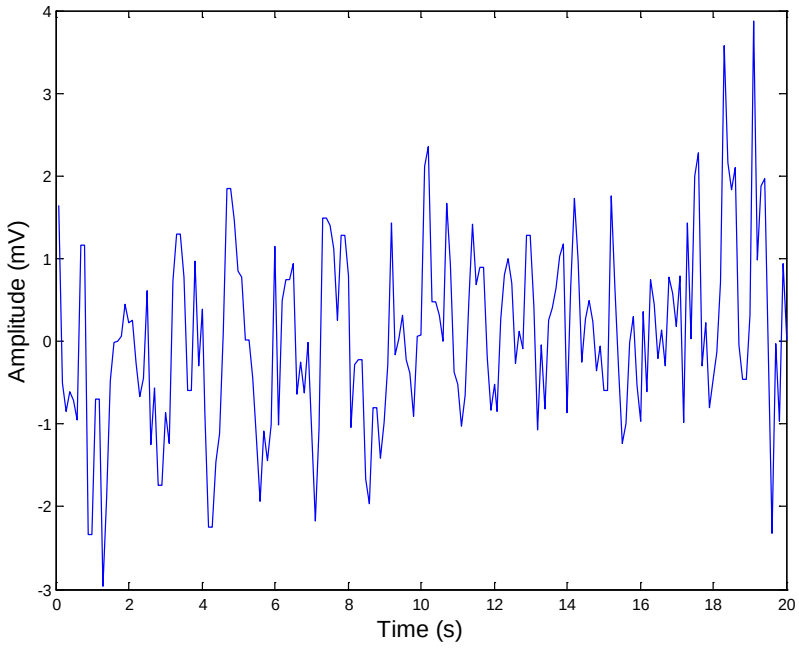

Figure 4.11: *One point of the magnitude cycle rate of the selected seven points on the measured signal.*

In this Figure, it is not easy to identify the frequency components by looking

at the original signal. Converting to the frequency domain, the discrete Fourier transform of the signal amplitude is found by taking the fast Fourier transform (FFT) as mentioned in chapter 3.2. For each row of matrix **S**, the breath frequency can be determined from magnitude circle rate by using the fast Fourier transform as same as equation 3.19

$$\mathbf{S}(k) = \sum_{q=1}^{Q} \mathbf{s}(q)\omega_Q^{(q-1)(k-1)}, \tag{4.16}$$

where $\omega_Q = e^{(-2\pi i)/Q}$ is an Q_{th} root of unity.

The mean data and the peak value of breath frequencies of seven points are obtained by two equations 3.20 and 3.21 respectively. The frequency spectrum from an observation time of twenty seconds is shown in Figure 4.12.

As mentioned in chapter 3.2, a waveform with a zero DC component is known as a DC-balanced waveform. The DC-component, the mean value of the waveform, is removed. A trip distance of 214.5 cm from transmitter to the chest of the person and back to the receiving antenna and a breath frequency 0.2 Hz of the hidden person are determined. The measuring time from starting the procedure (sending the pulses, measuring, receiving, signal processing) to getting a result for trip distance and frequency is approximately 44 seconds.

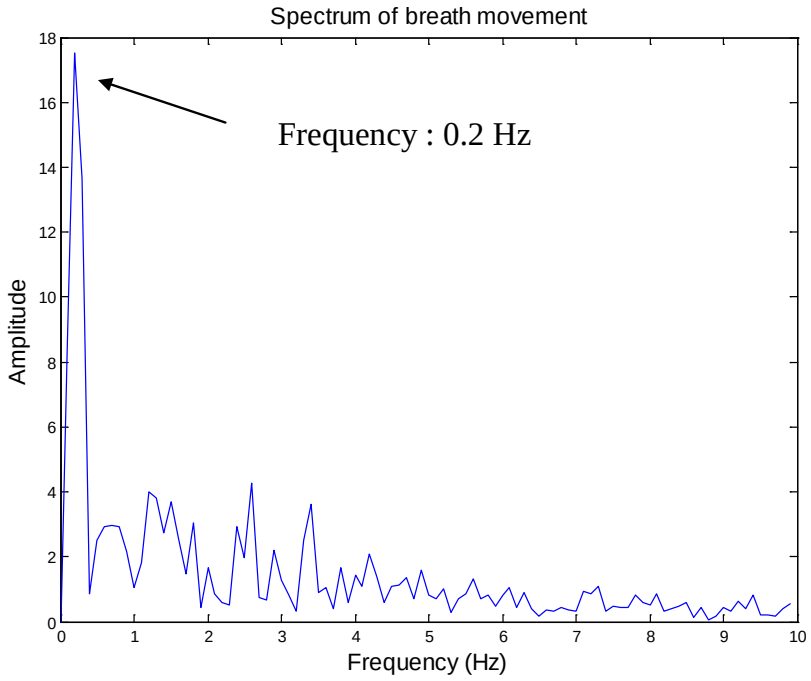

Figure 4.12: *Breath frequency determined by using fast Fourier transform (The DC-component has been removed).*

4.3 Results

The result of the detection through an almost homogenous wall (12 cm) is shown in Figure 4.13. Two signs ○ and + express the expectation and measurement position respectively. The results of the measurements are close to our expectation at a distance of up to 4 m from the radar's X-axis to the person. The accuracy of the position of a person is calculated and shown in this figure. Two respiration frequencies of a person are detected by the two receiving antennas. The mean frequencies corresponding to each position are about 0.15 Hz to 0.3 Hz.

As mentioned in chapter 4.1, the four types of measurements include the tin plate moving with the chest of the person, detection tested directly on the chest of the

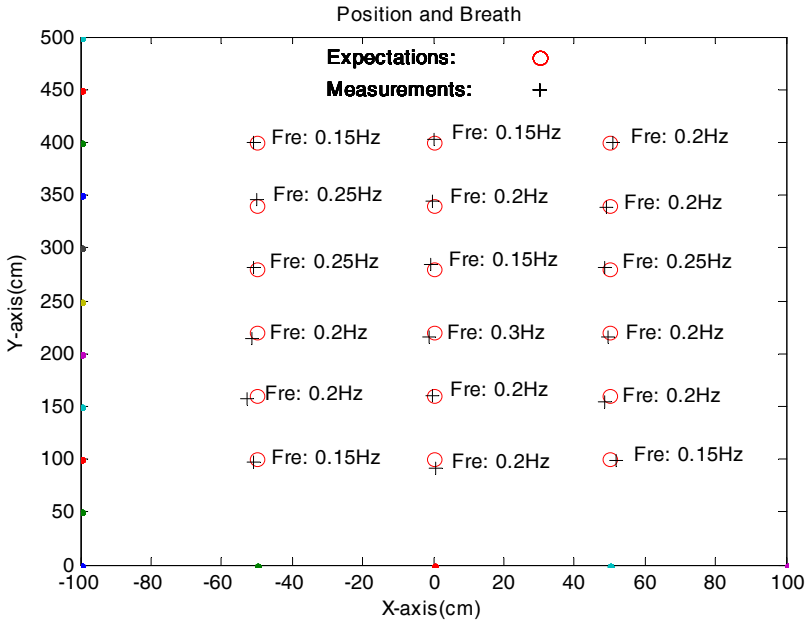

Figure 4.13: *Results of the detection through a near homogenous wall (12 cm).*

person, detection with a small wood board between the antennas and the person and detection tested at a certain distance close to a homogenous wall between the antennas and the person. The results of both position and breath frequency from these four measurements are shown in Figure 4.14.

Two signs ○ and + express the expectation and measurement position respectively. The first figure presents the results of the detection with a tin plate in front of the chest of a human. The second one shows the results of the detection direct on the chest of a human. The third one presents the results of the detection through a thin wood board between antennas and a human. The last one expresses the results of the detection through a near homogenous wall. For the first to third figure, the maximum measurement distance limited by our laboratory is 350 cm. The results of position are close to the expectation but deviate slightly and more

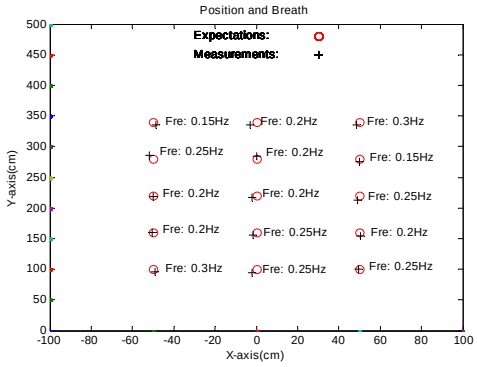

Results of the detection with a tin plate in front of the chest of human

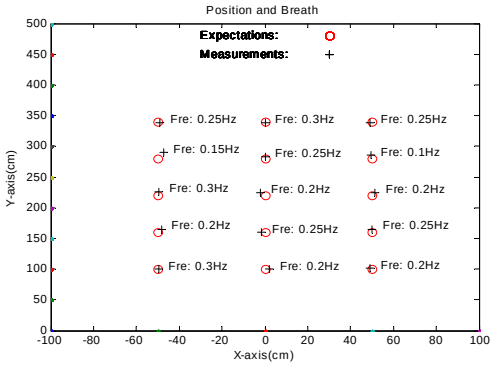

Results of the detection direct on the chest of human

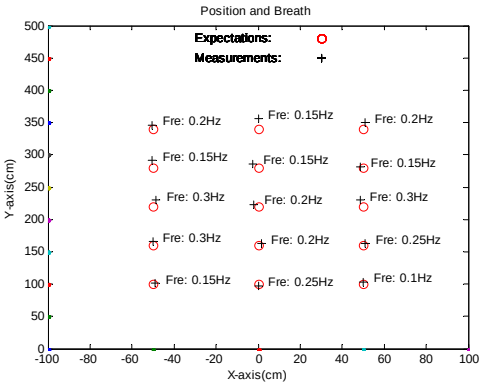

Results of the detection through a thin wood board between antennas and human

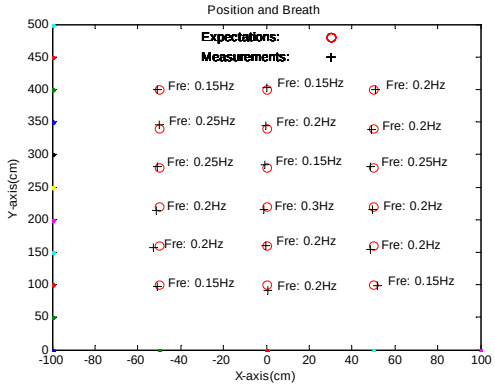

Results of the detection through a near homogenous wall

Figure 4.14: *Results of four types of measurements.*

in the latter figures. There are two reasons for this. One is that the amplitude of the reflected signal becomes weaker from the first to the third type of measurement as mentioned before. The other is that the delay time in the board was not considered in distance calculation.

The mean respiration frequencies of a person are also detected by two receiving antennas. The frequencies corresponding to each localization are about 0.1 Hz to 0.3 Hz. In the last measurement, the detection is tested with no limiting distance

Table 4.1: Position finding errors of measurements

Measurement type	Max absolute error (cm)	Root mean squared error (cm)
The 1^{st} measurement	7	4.7
The 2^{nd} measurement	10	4.4
The 3^{rd} measurement	16	7.5
The 4^{th} measurement	9	4.8

and a wall between the antennas and the person. The maximum measurement distance is 400 cm. The breath frequencies corresponding to each localization are expected to be approximately 0.15 Hz to 0.3 Hz.

The radar position finding errors in these four measurements are shown in Table 4.1. From the table, the maximum absolute and root mean squared errors of the first, second and fourth measurements are similar with each other. It is proven that considering the time delay in the TOA calculation is essential and effective. The error of the third measurement is higher than that of the others because for this measurement with a wood board, the time delay was not considered. However, in the fourth measurement the time delay which was caused from the wall was taken into consideration. The position error is then close to the measurements which is without obstacles. The maximum error of 9 cm in the fourth measurement should be low enough to locate a person in a pile of debris.

Chapter 5

Breathing Simulator System

There are many necessary reasons for building a breathing simulator to get characters of breathing measurements at different angles through a wall in different situations. The first is that this measurement needs a lot of time to obtain a large amount measurement data. Therefore, a person should be in front of a UWB system for a long time. It is impossible for a human to breath with a constant and given frequency for that time. The second reason is that even when finding a person, the error could be larger by the chest movement, the human position, human shaking and so on. Finally, it can be checked whether the algorithm which was mentioned in chapter 3.2 and 4.2 works or not by comparing the extracted results with a reference (frequency of breath simulator). For these reasons, it is best to create a simulator having an adult breath frequency of 15-20 times/per minute.

The principle of this simulator is shown in Figure 5.1. It includes a PC which gives a speed command to a microcontroller. The microcontroller transforms the

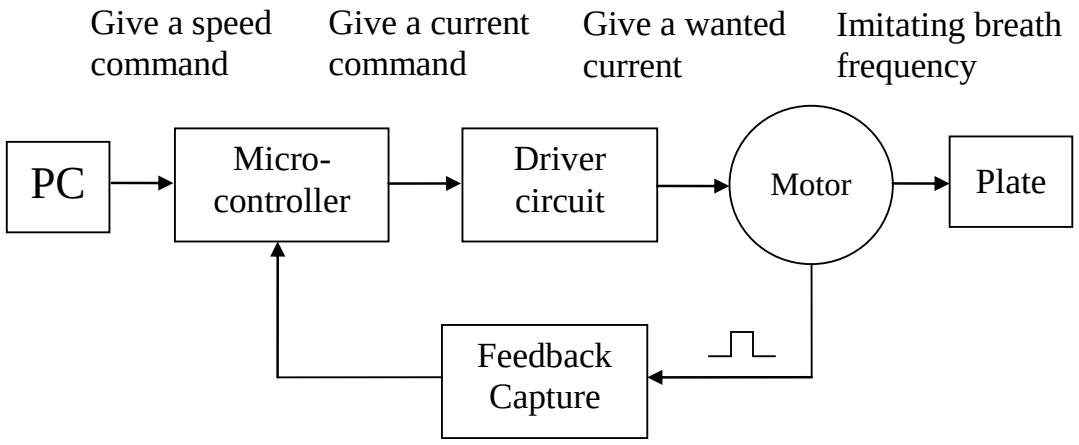

Figure 5.1: *The principle of the breath simulator.*

wanted speed into a current command and gives it to a device with a driving circuit. This device receives the command and feeds the wanted current into a motor. The motor is connected to a tin plate which is moved forward and backward to imitate human breath. A light sensor is connected to the motor and set to be a feedback capture. When the motor rotates, the sensor will capture the feedback pulse according to the motor speed. The feedback pulse will be sent back to the microcontroller to compute the speed of the motor. The speed will be compared to the speed command in the microcontroller. The microcontroller will produce a new current command and give it to the driving device.

According to the principle of the breath simulator, the base of the simulator is like a horn antenna and is shown in Figure 5.2. The base of the simulator is made of wood. The number ① shows the square dimension of the front side which is 100 cm × 100 cm. The inner number ② shows a tin plate which is 24 cm × 20 cm connected to the corners of the front side with elastic cords (number ③). The number ④ shows a string connecting both the motor and the elastic cords. The

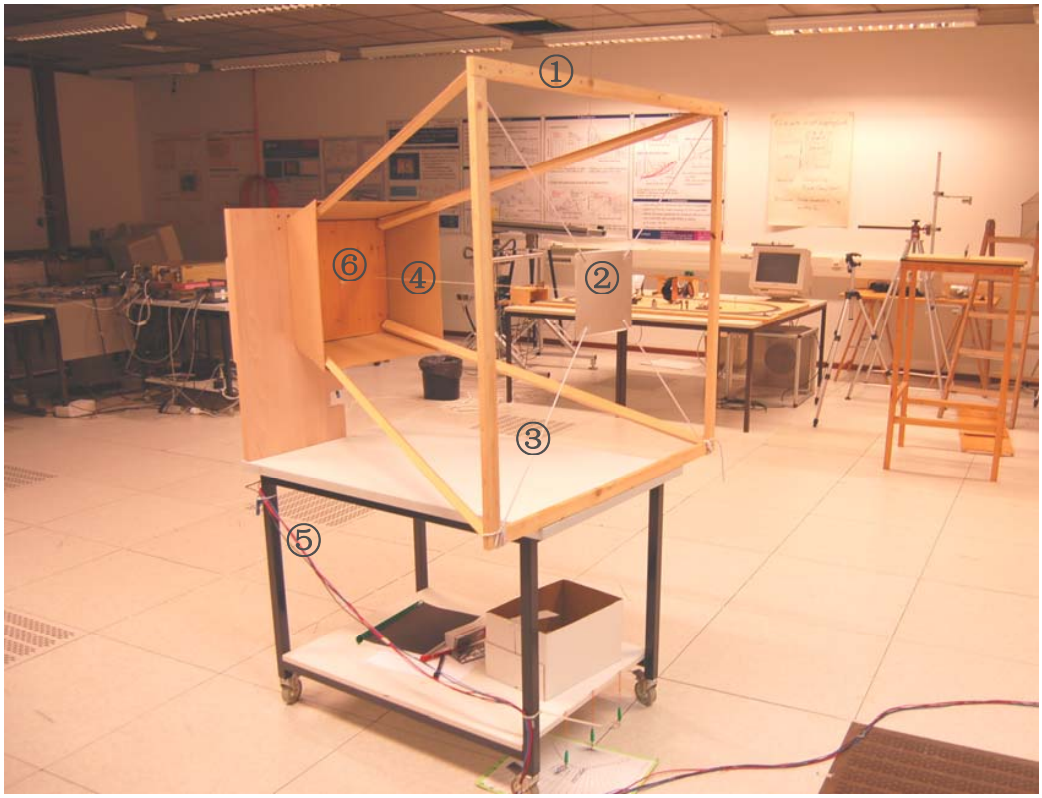

Figure 5.2: *The base of the simulator.*

number ⑤ shows the power lines connected to the sensor and motor, and lines for sending feedback signals to the microcontroller. Behind the wood plate (number ⑥) there is a rotating DC motor connected to the string and a light sensor. The tin plate will be moved forward and backward following the motor speed. In other words, the simulator system converts rotation movement of the motor to the tin plate's linear movement.

The concept of a closed loop system model is shown in Figure 5.3. A speed command in rotations / -second from a computer is sent to the speed control unit. The speed command is transformed into a digital signal in the unit and is sent to the external digital to analog converter (DAC). The DAC driver input serial data

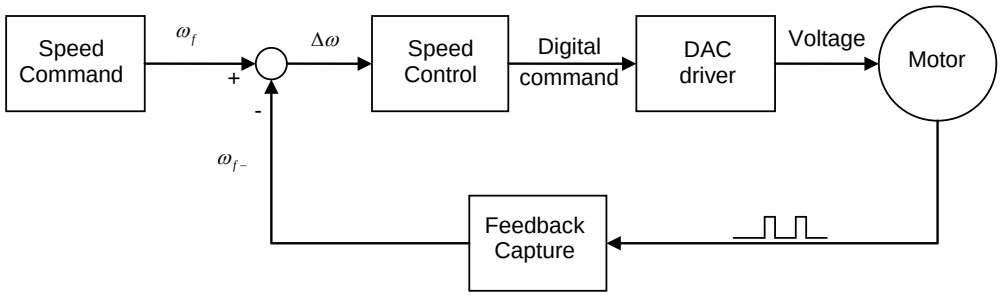

Figure 5.3: *Close loop system model.*

command and the output analog voltage is used to drive a motor. The feedback unit captures the motor sensor pulse, calculates the speed and then feeds it back to the controller. The controller calculates the difference $\triangle\ \omega$ between the speed command w_f and actual motor speed feedback w_{f-}. The speed command is adjusted by the control unit according to the difference.

The system block diagram of the simulator is shown in Figure 5.4. The voltage stabilizing circuit feeds 5 volts to the DAC and motor device. A microcontroller is used to get a speed command from the computer. The speed command is transformed into a digital signal serial CLOCK, serial DATA and frame synchronization and sent to the external DAC hardware. The DAC driver receives the serial data command and generates an analog voltage to drive a motor. The feedback unit captures the motor sensor pulse, calculates the speed and then feeds it back to the controller. The comparison between the wanted speed and the feedback data makes a new speed command given to the DAC.

The algorithm function will be described in detail in the following.

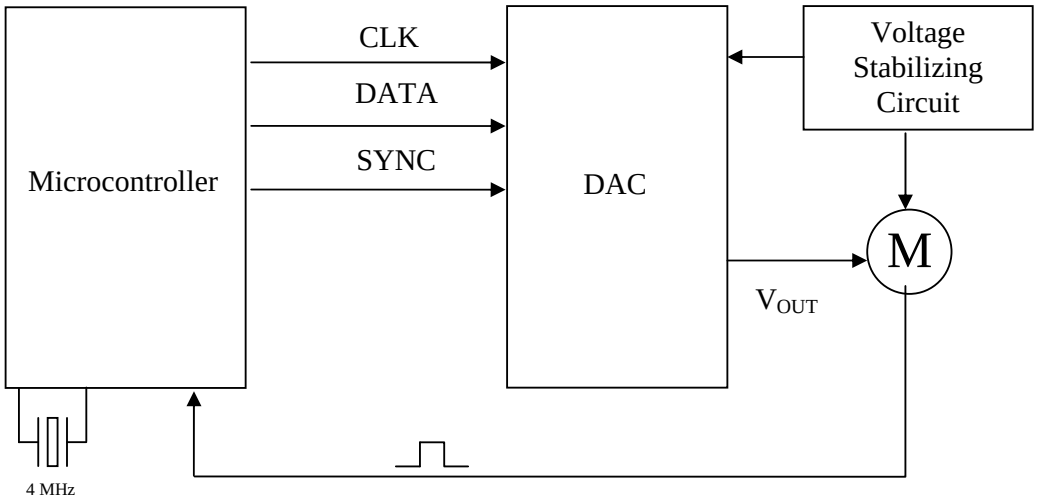

Figure 5.4: *System block diagram of breath simulator.*

5.1 The Microcontroller Fujitsu MB90F595

The Fujitsu MB90F595 Microcontroller includes a Full-CAN interface and a Flash-ROM memory, a 32-bit accumulator for processing large data. It also has some features of including 8/10-bit A/D converters, UART (SCI), an extended I/O serial interface, an 8/16-bit PPG timer, a 16-bit I/O timer (input capture units(ICU), output compare units(OCU)) and a stepping motor controller [26].

The instruction set of the CPU $F^2MC-16LX$ is supplied with a high level programming language(C language). Below the principal characteristics are reported:

1. 16-bit core CPU; external clock 4 MHz (16 MHz internal, 62.5 ns instr. cycle

time).

2. 0.5 μ m CMOS Process Technology.

3. FULL-CAN interface: 1 channel, conforming to version 2.0 Part A and Part B, flexible message buffering (mailbox and FIFO buffering can be mixed) and powerful interrupt functions (8 programs; priority levels; 8 external interrupts).

4. EI^2OS - Automatic transfer function independent of CPU; 10 channels of intelligent I/O Services.

5. 18-bit time-base counter.

6. Watchdog timer.

7. Full duplex UARTs.

5.2 The DAC121S101

When digital information must be converted into a continuous quantity like voltage or current, a DAC (digital-to-analog converter) is used. The DAC121S101 is a full-featured, general purpose 12-bit voltage-output digital-to-analog converter that can operate from a single +2.7 V to 5.5 V supply and consumes less power. The converter is chosen to supply a programmable voltage for the transistor in order to adjust the current to the motor [27].

5.3 The three-terminal positive regulators of L7805CV

The regulator can provide local on-card regulation, eliminating the distribution problems associated with single point regulation and can employ internal current limiting, thermal shut-down and safe area protection. Although designed primarily as a fixed voltage regulator, the device can be used with external components to obtain adjustable voltages and currents [28]. The maximum current is 1.5 A. This regulator will be used to supply the voltages and currents for the DAC input power and a power transistor current to run the motor.

5.4 DC Motor and rotational speed measurement

The BD677 is a silicon and epitaxial-based NPN power transistor. It is intended for using in medium power linear and switching applications. The maximum current I_E of this transistor is 4 A [29]. It is enough to supply the current to the used motor.

The Modelcraft high performance geared motor has a nominal voltage of 12 V/DC and a maximum load current of 0.75 A. It is used to connect the emitter of the power transistor BD677. The normal starting pulse current with a load (tin plate) is approximately 1.2 A. Four pieces of metals are adhered to the rotor of the motor.

The EE-SX672 T-shaped light sensor is available with Light-ON output configu-

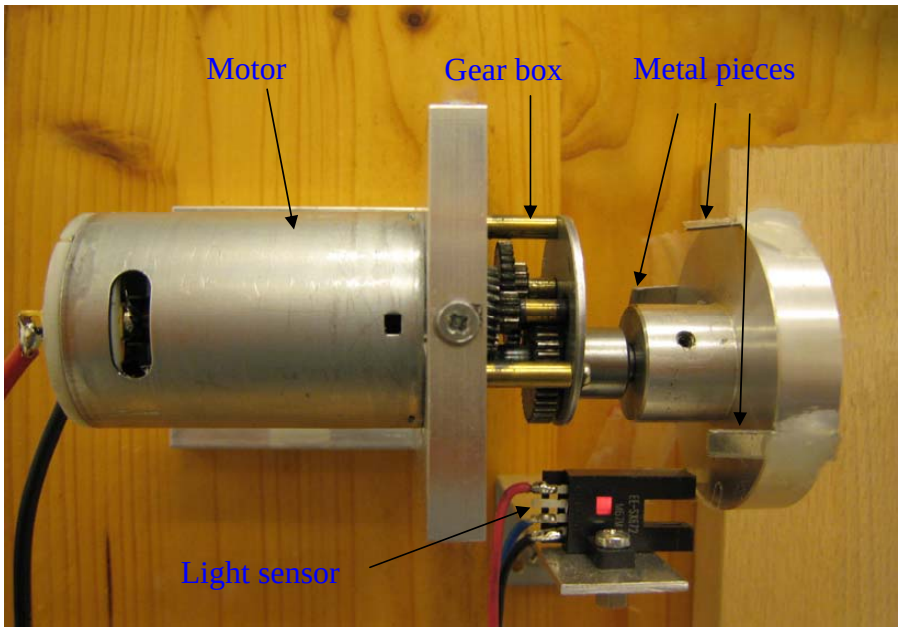

Figure 5.5: *Motor and light sensor device.*

rations and a wide DC operating voltage range of 5 to 24 V. It also has a response frequency as high as 1 KHz and an easy operation monitor with a bright LED [30]. The sensor is used for catching pulses when the metal pieces pass the GaAs infrared LED. The motor and light sensor device is shown in Figure 5.5. When the motor rotates, the metal pieces will pass the infrared LED of light sensor. The sensor will generate pulse cycle according to the real motor speed. The pulse is sent back to the microcontroller. The microcontroller determines the speed by the time interval between two pulses. With this information the true speed can be compared with the wanted speed.

5.5 Microcontroller and driven circuit devices

Figure 5.6 shows the complete assembly of the Fujitsu MB90F595 and the motor drive circuit. Moreover, there is also a switch that enables the microcontroller to work in the programmable or release state: when loading a program on the microcontroller is required, it must be set to "P" position; when it is required that the program runs on the microcontroller, it must be set to "R" position. It is also possible to connect the PC and the microcontroller through the USB interface.

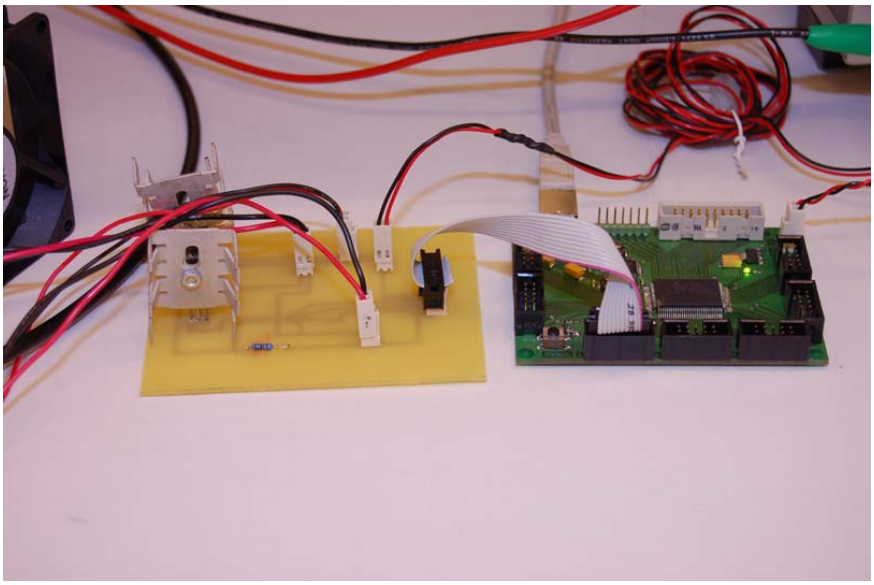

Figure 5.6: *Realized microcontroller board and motor drive circuit.*

5.6 Simulator device

Figure 5.7 shows the simulator system device. The $F^2MC-16LX$ 16-BIT Microcontroller MB90F595 of Fujttsu Semiconductor Company is used to control and

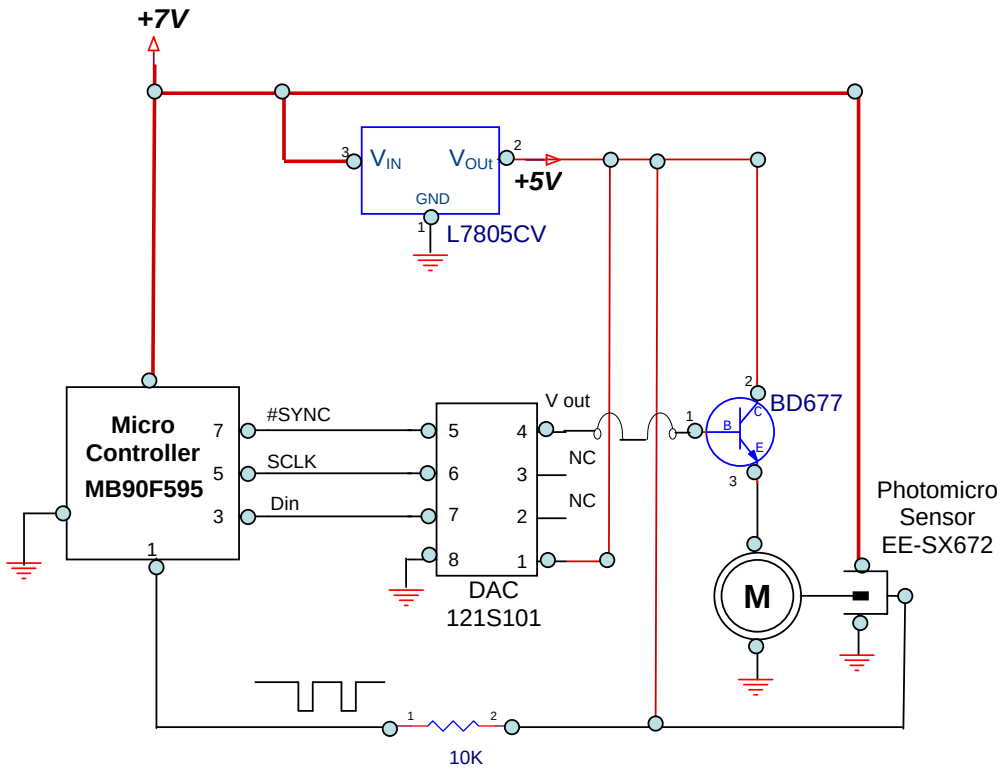

Figure 5.7: *Simulator system device.*

calculate the speed of the motor. The connection pins and functions of the micro-controller are shown in Table 5.1. The pin name p20 (pin 1) of this controller is set to input mode (0), in order to get a feedback signal. The pin name P24 (pin 5) is set to output mode (1). It is used to create the serial CLOCK. The pin name P22 (pin 3) is in output mode (1). It is used to create the serial DATA. The pin name P26 (pin 7) (output mode (1)) is defined to create frame synchronization (SYNC) [27]. The pins with numbers 5, 6 and 7 of the DAC are partly connected the pins numbered 7, 5 and 3 of the U.C. The output voltage of the DAC goes into the base of a power darlington transistor BD677. The L7805CV positive voltage regulator is chosen to supply 5 V to the DAC and the collector of the BD677. The power transistor BD677 feeds a current to the motor. Four metal pieces adhered

Table 5.1: The connection pins and functions of microcontroller

Microcontroller pin(name)	Sensor feedback	DAC pin 5	DAC pin 6	DAC pin 7
p20(pin 1)	Input mode to get feedback signal			
P22(pin 3)		Output mode to create serial DATA		
P24(pin 5)			Output mode to create serial CLOCK	
P26(pin 7)				Output mode to create Frame synchronization (SYNC)

to the rotor of the motor passing the LED light of a sensor causes four pulses. The pulses are sent back to the microcontroller to calculate the delay time with the previous pulse and compare it to the original speed.

The simulator system uses automatic feedback control theory to auto trace and adjust motor speed. When a lower speed is detected by the micro-controller, the current will be increased to speed the motor up or will be decreased to slow the

motor down in a higher speed situation. The system will adjust the actual motor speed to the wanted speed automatically. The speed of the motor can be adjusted from 2 to 6 sec/per rotation. That means it can simulate a breath frequency of 10-30 times/per minute. This includes our expected frequencies which are 15-20 times/per minute.

5.7 C program

A C program is developed to control the system. This program runs on the Microcontroller after compilation. The function of this program is described in the following:

5.7.1 Programming the Microcontroller

For programming the microcontroller, the tool Softune Workbench [31] is used, while for the transfer of the created programs from PC to the flash memory of the microcontroller, the software "Fujitsu Flash MCU Programmer" is used. The goal is to control the outputs of the DAC with the *Matlab*.

5.7.2 Programming with Softune Workbench

Softune Workbench is a software collection for developing programs for the F^2MC-16 family of microcontrollers. It is combined a development manager, simulator debugger, emulator debugger, monitor debugger, and an integrated development environment. For the microcontroller program, a scheme of the synthesis for the code was written. The MAIN PROGRAM is the first that appears when Softune Workbench is opened. The first code line includes some libraries with the command INCLUDE. The first of them is the MB90F595.h library which is provided by Fujitsu to initialize the microcontroller. The function of each port of the device is defined in a C language [31].

The second included library allows the execution of the bit operations. The serial library allows a serial communication to be settled the interface of computer and the UART1. In our case, the MC internal registers are assigned to receive and transmit data. The ports are also assigned. The other important is the DAC address. This is a physical address set to connect to the DAC121S101 at the corresponding pins. The whole firmware flowchart of the C program is shown in Figure 5.8.

5.7.3 Microcontroller - USB interface

The Universal Asynchronous Receiver Transmission (UART) is one of the most popular serial protocols. The data bus can support a full duplex transmission between two pairs of receivers and/or transmitters. This type of protocol is used

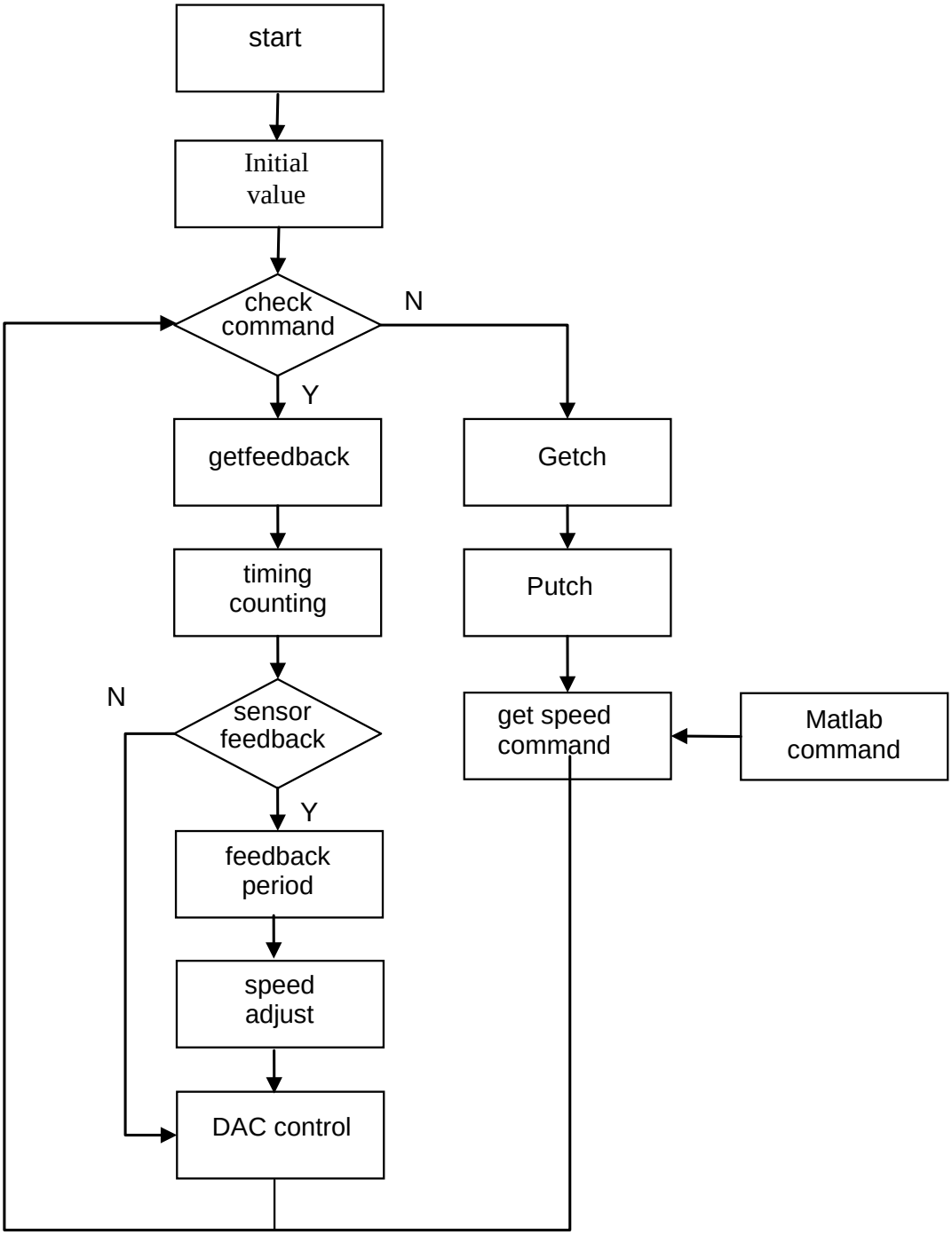

Figure 5.8: *Firmware Flowchart.*

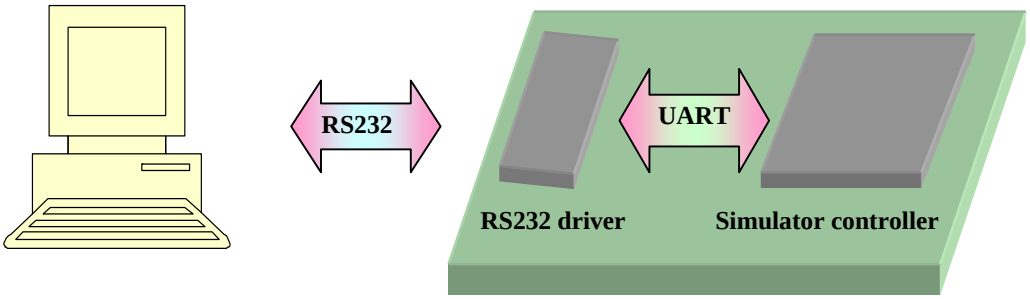

Figure 5.9: *Connections between PC and Microcontroller.*

for the communications between the computer, microcontroller and motor sensor [26] [31].

The UART is the chief component that communicates through the serial ports of computers. Normally, it is connected to the circuit that generates a signal conforming to the RS232 standard. Therefore, the connection between UART, microcontroller and the computer should have a driver to convert the voltage levels in conformity with the RS232 as shown in Figure 5.9.

Chapter 6

Measurement with Breathing Simulator

An application of UWB radar system with breathing simulator (UWBSBS) for remote measuring of the position and respiration of hidden persons in varying positions and angles is presented in this chapter. The system can both control the simulator and measure the breath frequency at the same time. The concept is based on transmitting sub-nanosecond pulses to achieve the measurement of imitated breathing movement. For signal processing variance, zero-phase filtering and round trip time are used to determine the position after removing background distortions. Breath frequency is determined by the magnitude cycle rate due to the imitated breathing movement. A fast, robust and accurate method to get measurements was achieved. The real measuring method, signal processing and practical results of the tests are presented here.

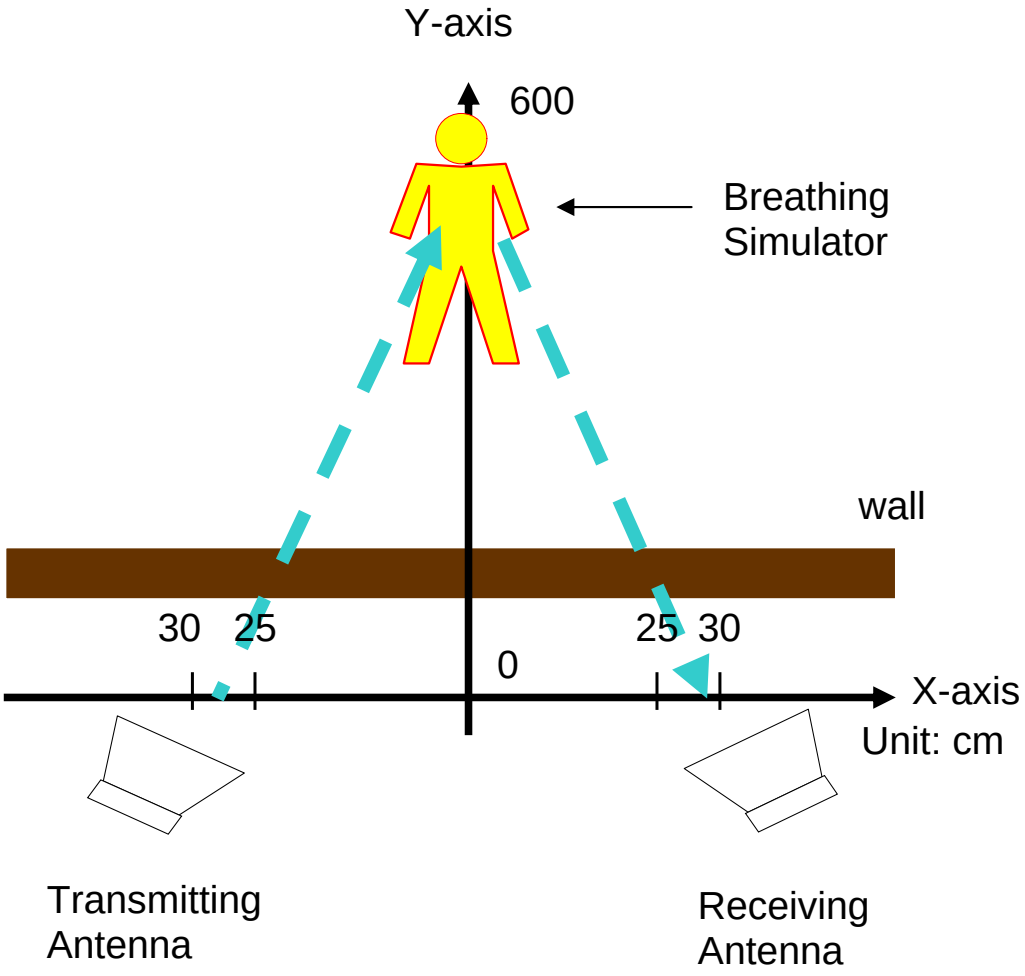

Figure 6.1: *Geometrical setup.*

6.1 Measurement setup

Figure 6.1 shows the geometrical setup, using one transmitting antenna and one receiving antenna to detect the breathing movement of the simulator behind a near homogenous wall. The transmitting signal penetrates the wall and touches the plane of the simulator. The forward and backward movement of the simulator is controlled by the computer. In this way, there are reflective signals coming back to the receiving antenna. The travelling time from the transmitting antenna to the

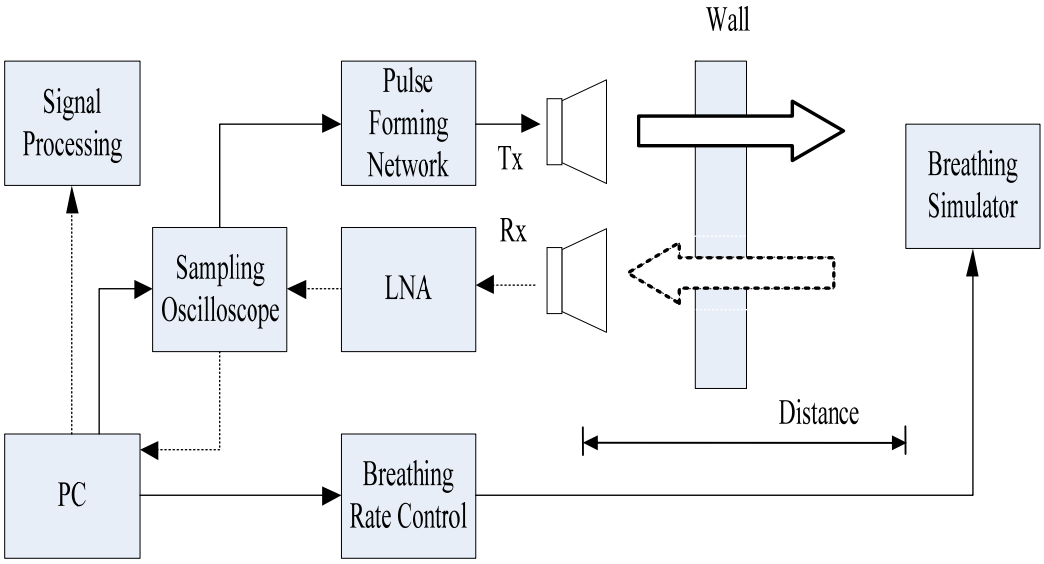

Figure 6.2: *Block diagram of measurement set-up.*

breathing simulator and back to the receiving antennas is measured. According to the travelling time, the frequency of the chest movements of the person is calculated from the magnitude cycle rate due to breathing movement.

An ultra wideband impulse radar test setup for generating real air/simulator boundary reflection data was built. The block diagram of the measurement set-up is shown in Figure 6.2. A pulse generator is used to generate a step pulse. But the transmitting antenna can not transmit the DC pulse. It is essential to connect the generator to a pulse forming network to produce a Gaussian pulse. The output port of the pulse forming network is connected to a UWB transmitting horn antenna. The antenna is placed on the axis tilted at an angle of about 80 degrees and transmits the radiated pulse. The receiving antenna is set up at the right hand side of the transmitting antenna at a distance of 60 cm. The antenna is also arranged on the X-axis and toward the Y-axis at an angle of approximately

10 degrees.

The base of the simulator is put on a moving table. The front of the simulator is rotatable due to the moving table. There are two steps to measure the characteristics in different situations. The first is to know whether the algorithm works or not. Therefore, a reference is needed to compare the extracted results. The simulator is set to three reference frequencies 0.3333, 0.2857 and 0.25 Hz (3, 3.5 and 4 seconds / rotation). The distances along the Y-axis are 150, 210, 270, 330, 390, 450, 510 and 570 cm. Because the antennas are separated by 60 cm along the X-axis, the real distances will be 152.97, 212.13, 271.66, 331.36, 391.15, 451, 510.88 and 570.79 cm. The base of the simulator is stationed on a moving table and behind a wall. The result of this measurement shown in the following section, is good enough to prove that the algorithm works.

The second step is to use the same algorithm while rotating the moving table. The simulator starts facing left and parallel to the wall. The angle is 0°. The simulator will then be turned counterclockwise by 5° step by step until the simulator face is perpendicular to the wall and further until the simulator faces right and it is parallel to the wall. The angle is then 180°. The angles in our measurement are 0° to 175°. Therefore every position has 36 different angles called rotation angles. The rotation angles that are measured at the reference frequencies 0.3333, 0.2857 and 0.25 Hz of the simulator are called sensitive or reasonable angles. Continuous sensitive (reasonable) angles are called sensitive (reasonable) range. The others called insensitive (unreasonable) range. The setup of the rotation of the simulator is shown in Figure 6.3.

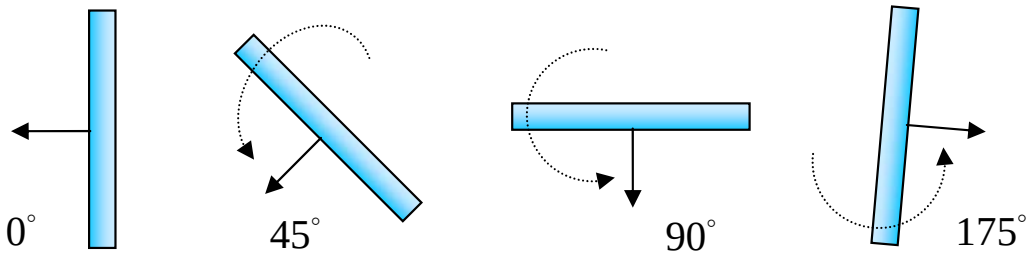

Figure 6.3: *Setup of the rotation of the plane of simulator in steps of* 5° .

The measurement points in a given area of 210 cm × 570 cm are shown in Figure 6.4. A wall is between the two antennas and the simulator. Two antennas are set to the positions (-30, 0) and (30, 0). The simulator is placed in 8 different rows (distances) away from the X-axis. The distances are 150, 210, 270, 330, 390, 450, 510 and 570 cm. The first row has the distance of 150 cm away from the X-axis and the last has the distance of 570 cm. There are 15 column points every 15 cm for each distance. The column 01 is at the left edge, 08 is the middle and the last column 15 is at the right edge. Each of these points has a number. For example number 21008 means that the row (distance) is 210 cm away from the X-axis and on this line the eighth column from the left edge. The configuration leads to 120 positions of measurement. The front side of the simulator faces the transmitting and receiving antennas. There are two lines from the simulator to each antenna. These two lines cause an angle ϕ called transmitting and reflecting angle (TRA). There is a different TRA at each point.

The output of the pulse forming network is connected to a UWB double-ridged

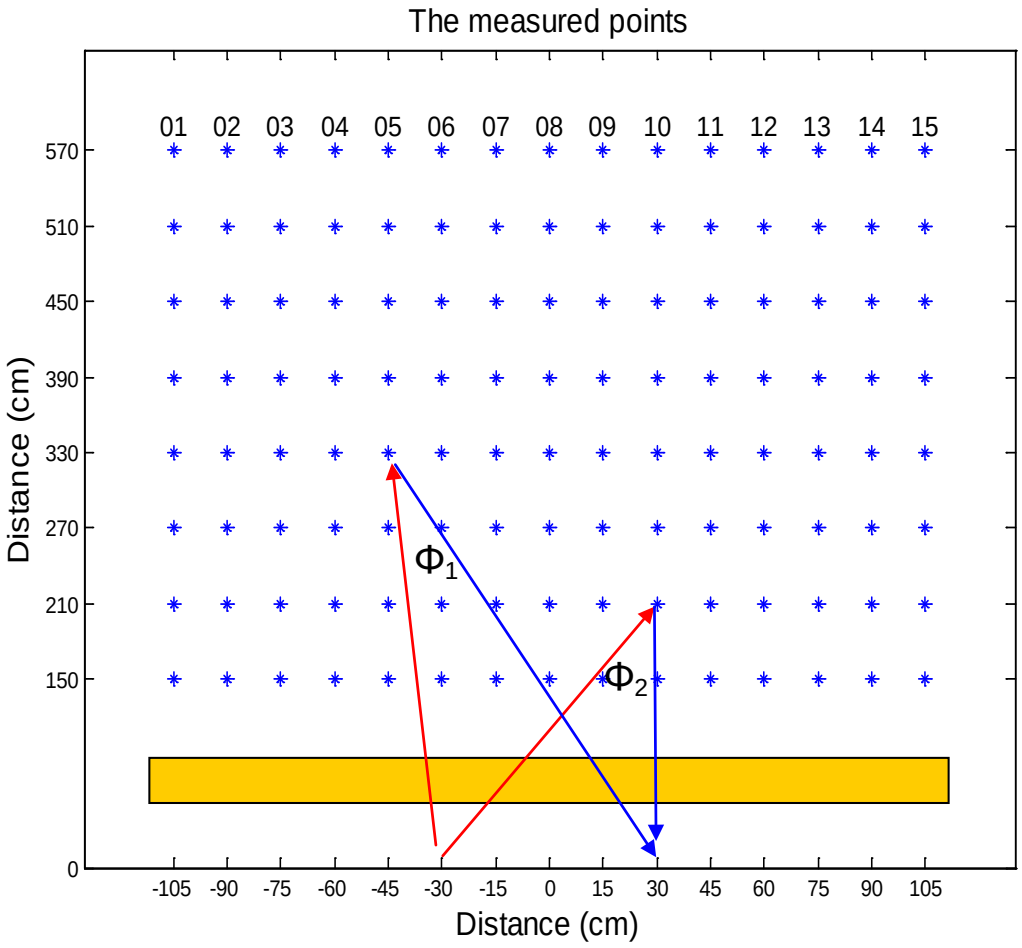

Figure 6.4: *Measurement points in a given area.*

horn antenna for the transmitting pulse. The pulse width of output pulse is about 600 ps, an output voltage $U_{pulse} \cong 4.2V_{pp}$ and a pulse repetition frequency of 200 kHz.

The transmitting pulse penetrates the wall and travels to the simulator. The radiated pulse is reflected by the surface of the simulator, penetrating the wall again and is received by the other double-ridged horn antenna. The measurement set-up for breath detection is behind a wall having a thickness of 12 cm,

and the distance between the antennas and the wall is 43 cm. Every 100 ms an actual reflection measurement trace is captured for a total measurement time of 20 seconds. Therefore, we got 200 data vectors from each measurement.

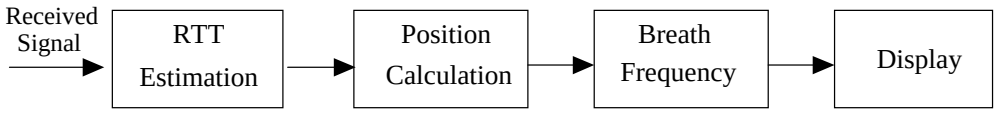

Figure 6.5: *Block diagram of signal processing.*

6.2 Signal processing

6.2.1 Calculation of position

Figure 6.5 shows the block diagram of the signal processing for position and breath frequency detection. After the receiving antenna received data from the chest of a person, the data was sent to a computer to do mathematical processing. Firstly, the round trip time (RTT) can be determined, then the distances and frequencies can also be determined. The results including distances and frequencies can be displayed on the screen of a computer.

With the presented UWB radar set-up, several breath movement measurements at different positions and angles were made. As an example measurement shown in Figure 6.6, the distance of the simulator from the X-axis is 270 cm and the breath frequency is set to 0.3333 Hz. The figure shows that the original reflected pulse caused by the simulator movement behind a wall was measured by the receiving radar.

The crosstalk is much higher than the reflection in the original data. The expected data is not observed clearly. A *Matlab* program was developed to process the

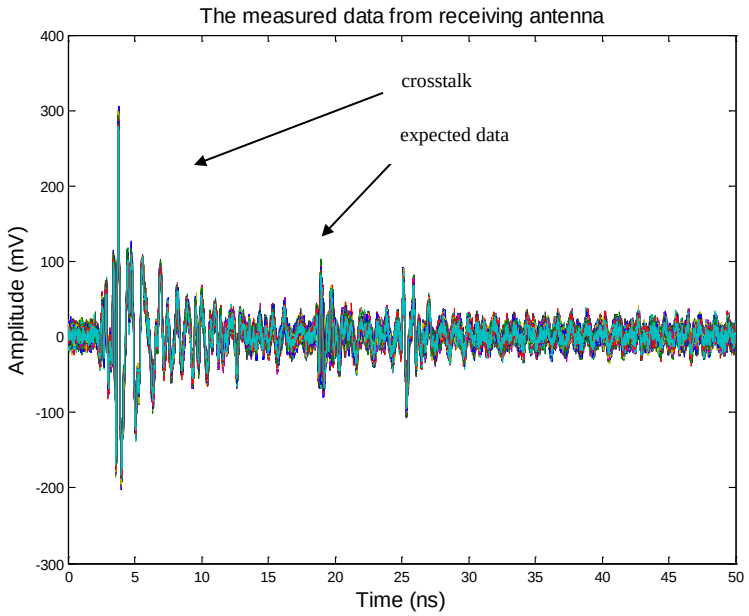

Figure 6.6: *Measured data from receiving antenna.*

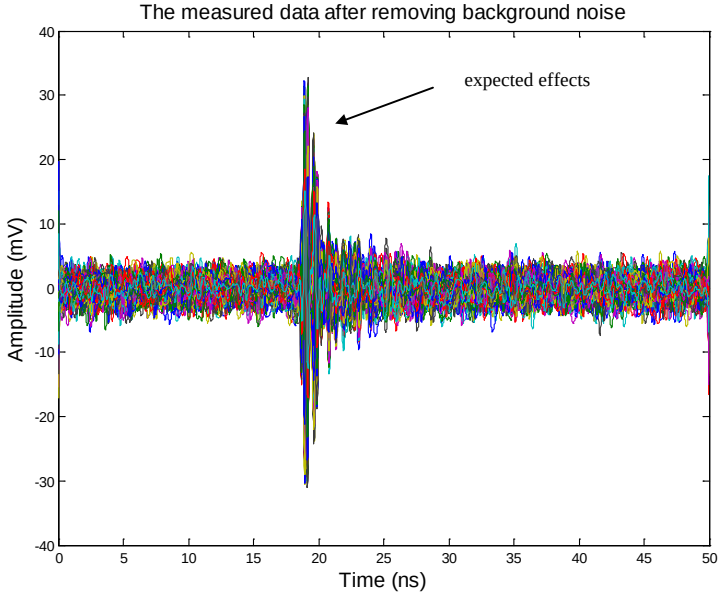

Figure 6.7: *Measured data after removing background noise.*

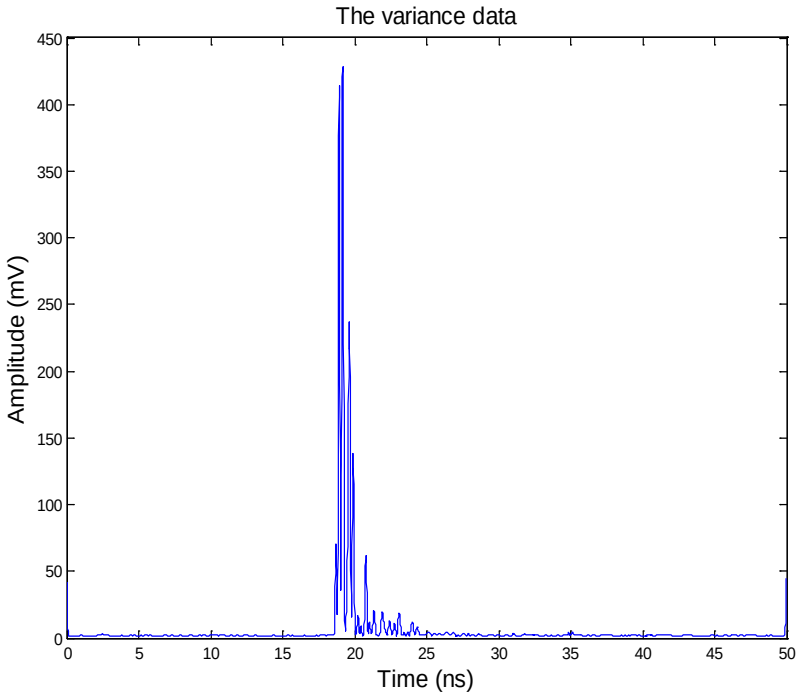

Figure 6.8: *Variance data.*

measured signal. Firstly, because obstacles are stationary in comparison to the chest movement, a moving average method is used to get the mean value of the original data. The stationary part of signal will be removed, similar to chapter 3.2. After this, a digital zero-phase low pass filtering as mentioned in chapter 4.2 is used to remove background noise. With these two methods, it is possible and robust to find the expected data behind the noise, similar to chapter 3.2 and 4.2. The expected effects can be seen in Figure 6.7 and the processed data can be described as the same as equation 4.5.

The signal of the breath movement is clear. Then, the unbiased variance of each column in the input over a period of time is computed to determine how large the differences are. The variance data is shown in Figure 6.8 and the data is expressed

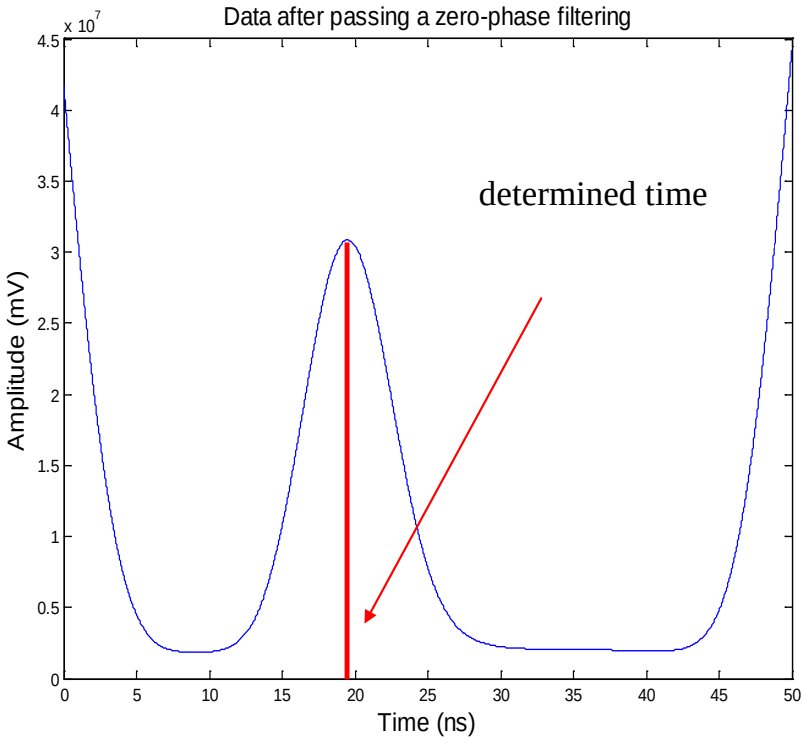

Figure 6.9: *Data after passing a zero-phase filtering.*

as equation 4.6. Zero-phase filtering is used to get the peak position time in the data. The determined time of the data is shown in Figure 6.9 and can be described as the same as equation 4.8.

From equation 4.8, the maximum peak value is shown exactly in chapter 4.2. The value of the t_p can be written as the same as equation 4.9

$$t_p = Max(\mathbf{D}_n), \tag{6.1}$$

where the **D** is the data matrix **A** after mean-subtraction, the first zero-phase low pass filter, variance and the second zero-phase low pass filter.

After subtracting the double starting and delay time in the wall we can get the

round trip time. The distances (D) along the Y-axis from the receiving antenna to the person is determined by the equation

$$D = \frac{(time * 3 * 10^{10} cm/s)}{2}. \tag{6.2}$$

6.2.2 Breath frequency

Furthermore, a way for determining the breath frequency was developed as one- and two-dimensional measurements in chapter 3 and 4. As mentioned in the two chapters, at any point in the affected area the magnitude cycle corresponds to the breath frequency. The defined positions of different selected points have been shown as in Table 3.1. Because seven points are better than 1, 3 and 5 points as recommended in chapter 3.3, a sample of seven points in the affected area is chosen for signal processing and shown in Figure 6.10.

The seven chosen points were selected. Every point has 200 column values. From equation 4.5, where x_{nm} is the n^{th} data value of the m^{th} point, the matrix H with 7 points and size 200×7 can be written

$$\mathbf{H} = \begin{bmatrix} h_{1,1} & h_{1,2} & \dots & h_{1,7} \\ h_{2,1} & h_{2,2} & \dots & h_{2,7} \\ h_{3,1} & h_{3,2} & \dots & h_{3,7} \\ \vdots & \vdots & \ddots & \vdots \\ h_{m,1} & h_{m,2} & \dots & h_{m,7} \end{bmatrix}. \tag{6.3}$$

The matrix **S** with size 7×100 is derived by the transpose operation of the matrix **H**. The transposed matrix can be determined as same as equation 4.15. In this

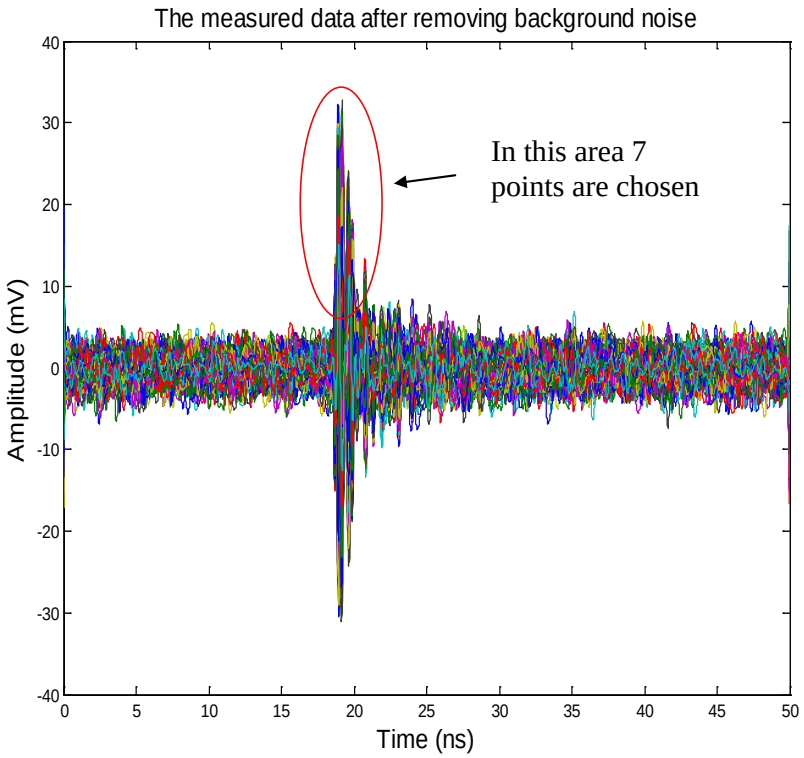

Figure 6.10: *Seven points are chosen.*

research, for each chosen point, the similar characteristics of time of the magnitude cycle over 20 seconds can be seen in Figure 6.11. The breath frequency can be determined from the magnitude cycle rate by using the fast Fourier transform. For each row of matrix **S**, the breath frequency can be determined from equation 4.16

$$\mathbf{S}(k) = \sum_{q=1}^{Q} \mathbf{s}(q)\omega_Q^{(q-1)(k-1)}, \tag{6.4}$$

where $\omega_Q = e^{(-2\pi i)/Q}$ is an Q_{th} root of unity.

The mean data and the peak value of breath frequencies of seven points are obtained by two equations 3.20 and 3.21 respectively as same as the two-dimensional measurement. The frequency spectrum from an observation time of twenty seconds is shown in Figure 6.12. As mentioned in chapter 3.2 and 4.2, a waveform

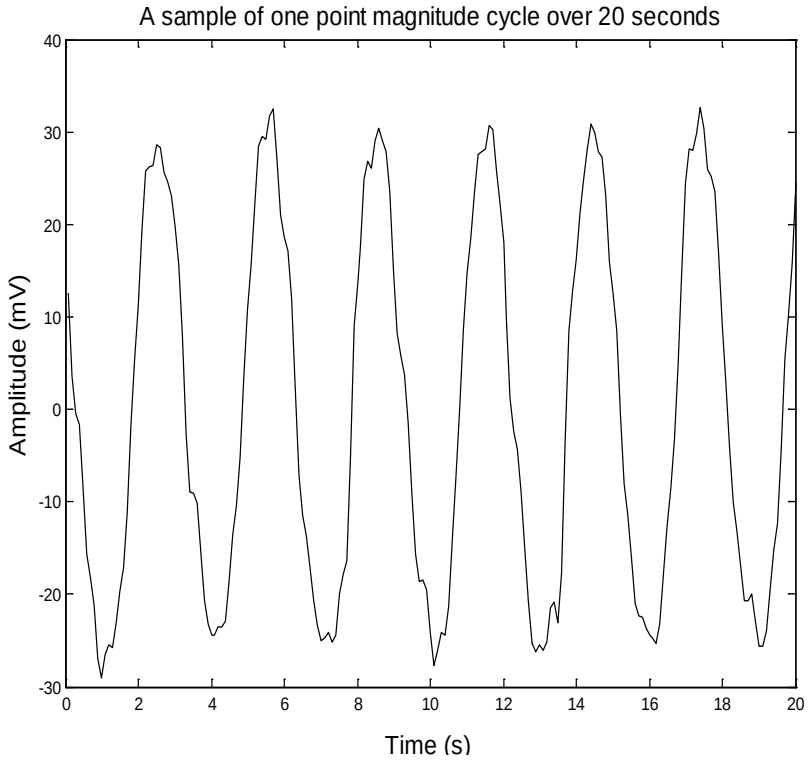

Figure 6.11: *A sample of one point magnitude cycle over 20 seconds.*

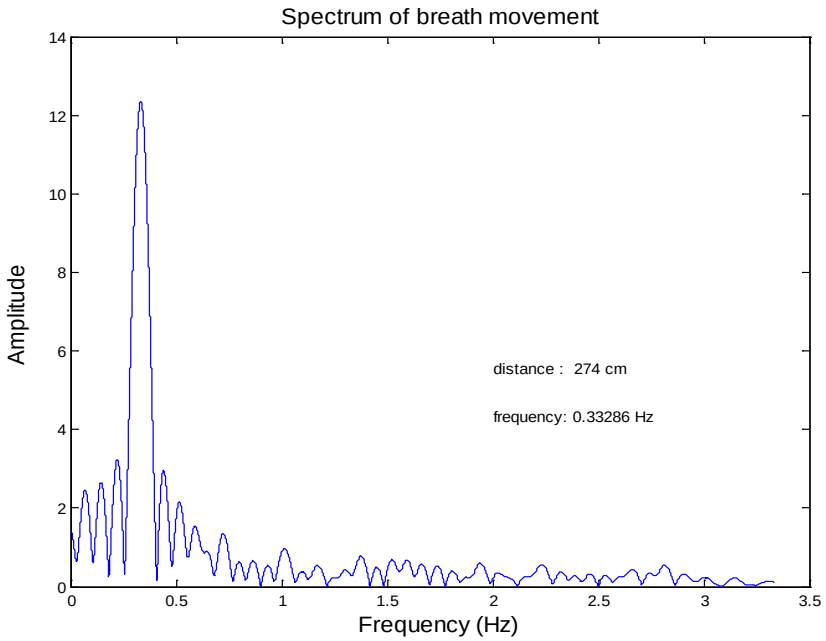

Figure 6.12: *Mean of seven breath frequencies determined by using fast Fourier transform.*

with a zero DC component is known as a DC-balanced waveform. The DC-component, the mean value of the waveform, is removed. A distance along the Y axis of 274 cm with a breath frequency of 0.33286 Hz was determined. The result is close to the real situation which is 272.07 cm along the Y-axis with a breath frequency 0.3333 Hz. The whole processing takes more or less 22 seconds.

6.3 Results

The result of the first step as mentioned in chapter 6.1 is shown in Table 6.1. The first column shows different real distances along the Y-axis due to the separated transmitting and receiving antenna as also mentioned in chapter 6.1. The corresponding predicted distance along the Y-axis, the error between real and predicted distance, the real frequency (0.3333, 0.2857 and 0.25 Hz) for every real distance, the predicted frequency and the error between the real and predicted frequency are shown in the following columns respectively. For comparison of the real and predicted distance, the maximum error is approximately 6.7 cm and happens at the predicted distance of 212.13 cm. The maximum error is 3.9 %. For comparison of the real and predicted frequency, the maximum error is 5.4%. The results for the predicted distance and frequency are good enough for a practical application of the system.

Next, the results of the second step, measurement at different simulator angles, were determined. There are 120 figures that correspond to the 120 measured points. Three signs $\bigcirc$, $*$ and $\triangledown$ express measuring in different imitated breath frequencies 0.3333 Hz (3 sec/per rotation), 0.2857 Hz (3.5 sec/per rotation) and 0.25 Hz (4 sec/per rotation) of simulator respectively. Some samples are shown in Figures 6.13 to 6.16. In Figure 6.13, the measurement point for the distance of 210 cm along the Y-axis and column number 10 is shown. The result shows the TRA between 74.1° to 90°. The sensitive range is 20° to 145°. It extends beyond both sides of the TRA.

Table 6.1: The results of the first step measurement

Real distance (cm)(1)	Predicted distance (cm)(2)	The error (%) of (1) and (2)	Real frequency (Hz)(3)	Predicted frequency (Hz)(4)	The error (%) (3) and (4)
152.97	147	3.9	0.3333	0.3461	3.9
152.97	147	3.9	0.2857	0.2855	0.1
152.97	147	3.9	0.25	0.2513	0.5
212.13	205.5	3.1	0.3333	0.3150	5.4
212.13	205.5	3.1	0.2857	0.2943	3
212.13	205.5	3.1	0.25	0.2605	4.2
271.66	266.5	1.9	0.3333	0.3400	2
271.66	269	0.9	0.2857	0.2725	4.6
271.66	266.5	1.9	0.25	0.2446	2.1
331.36	328.5	0.8	0.3333	0.3468	4.1
331.36	328.5	0.8	0.2857	0.2855	1
331.36	328.5	0.8	0.25	0.2586	3.5
391.15	389.5	0.4	0.3333	0.3447	3.4
391.15	389.5	0.4	0.2857	0.2969	3.9
391.15	389.5	0.4	0.25	0.2627	5
451	450.5	0.1	0.3333	0.3363	0.9
451	450.5	0.1	0.2857	0.2919	2.1
451	451	0	0.25	0.2379	4.8
510.88	516.	1.1	0.3333	0.3276	1.7
510.88	516.5	1	0.2857	0.2831	0.9
510.88	516.5	1	0.25	0.2517	0.7
570.79	575	0.7	0.3333	0.3381	1.4
570.79	574.5	0.6	0.2857	0.2815	1.5
570.79	575.5	0.6	0.25	0.2588	3.5

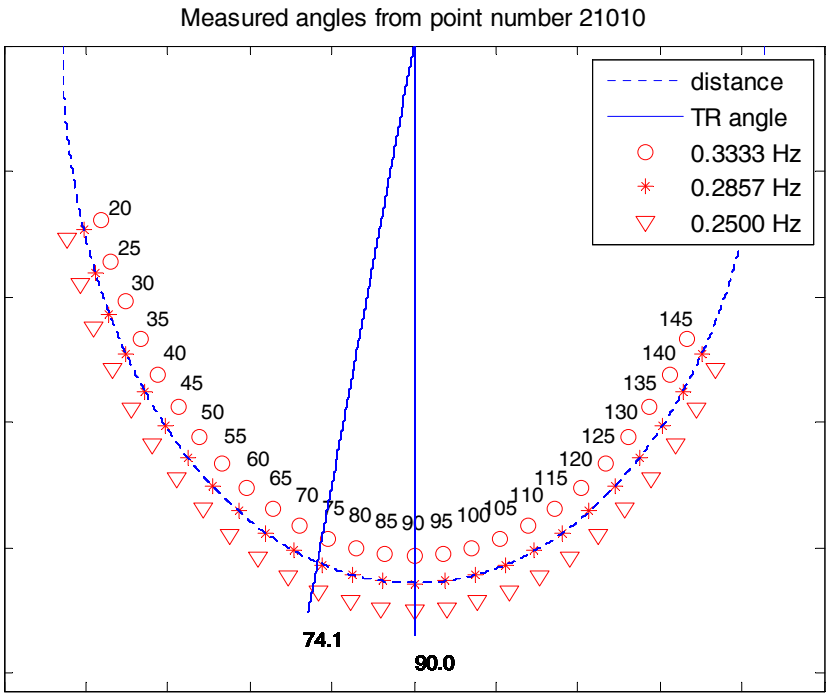

Figure 6.13: *The result of point No.21010.*

Figure 6.14 shows the measurement point having the distance of 330 cm along the Y-axis and the column number 08. The TRA is between 84.8° to 95.2°. The sensitive range is 50° to 135°. It also extends beyond both sides from the angles of the TRA. Only 0.3333 Hz and 0.2857 Hz were measured at the edge angle of 50°. The lower breath frequencies are detectable in the same way as the higher ones. The error in the frequency of 0.25 Hz at the angle of 50° is acceptable.

In Figure 6.15, the measurement point with the distance of 510 cm along the Y-axis and column number 12 is shown. The TRA is between 80° and 86.6°. The sensitive range is between 65° and 100°. It still extends beyond both sides of the angles of the TRA.

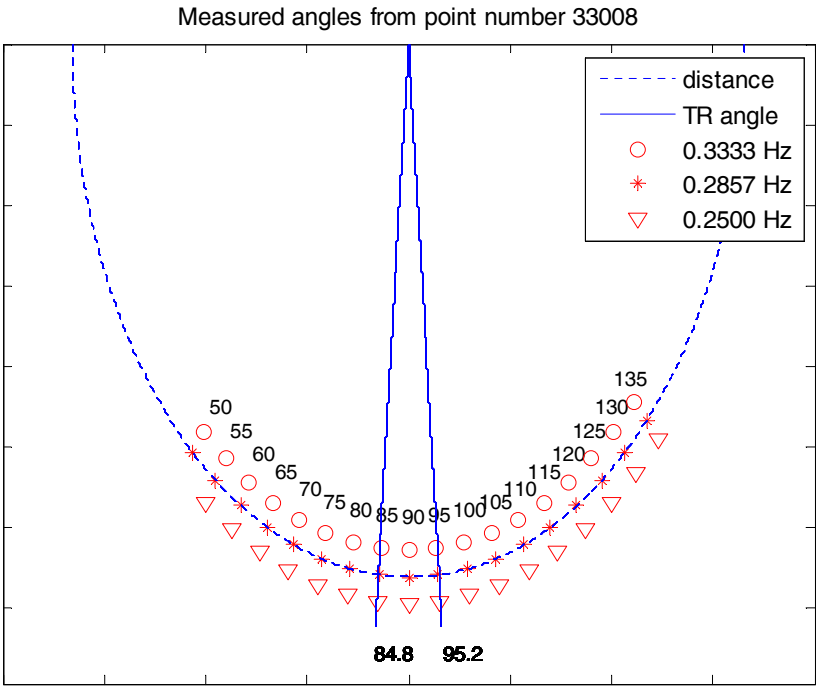

Figure 6.14: *The result of point No.33008.*

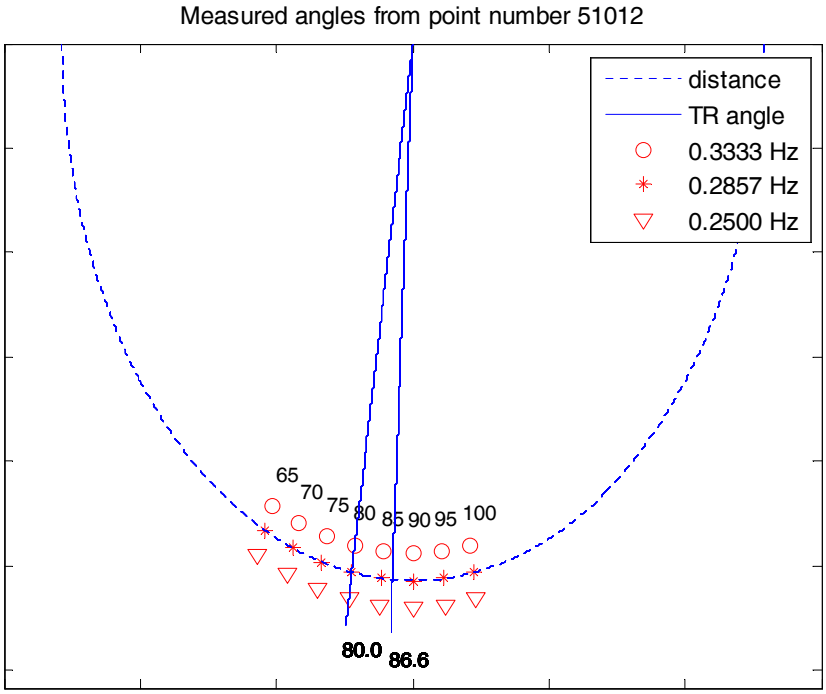

Figure 6.15: *The result of point No.51012.*

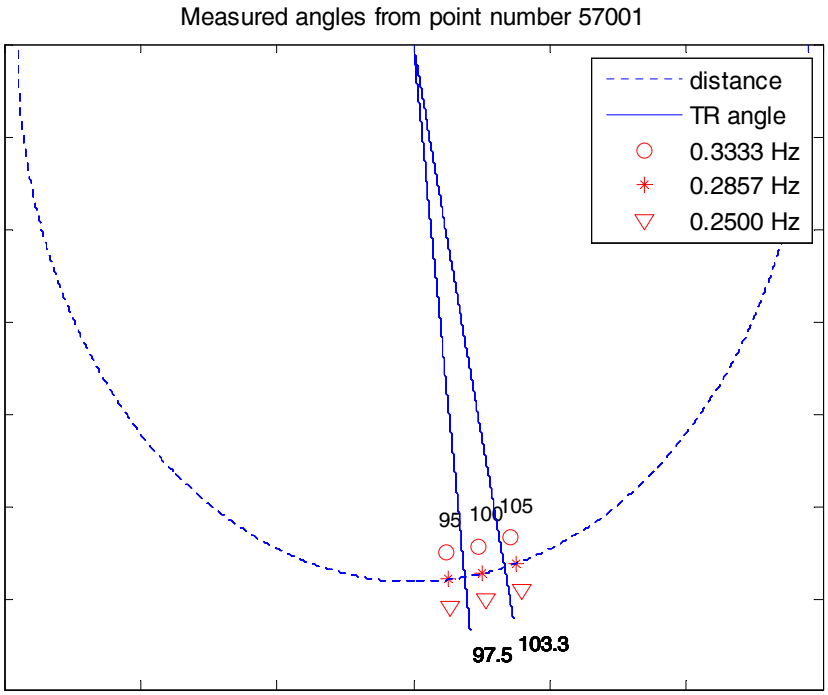

Figure 6.16: *The result of point No.57001.*

The measurement for the point with the distance of 570 cm along the Y-axis and the column number 01 is shown in Figure 6.16. The TRA is from 97.5° to 103.3°. The sensitive range is between 95° and 105°. It extends beyond both sides of the angles of the TRA as the same as Figures 6.13 to 6.15.

For getting more information on different positions, 15 measurements for 15 columns were made. The columns 01, 05, 10 and 15 are displayed graphically in Figures 6.17, 6.18, 6.19 and 6.20. Figure 6.17 shows the measured distance of 8 different positions for column 01. Every distance is measured with different rotation angles of the simulator. The angles are changed in steps of 5 degrees. In the first row, the distance was able to be measured for 16 angles with a sensitive range 80° to 155°. In the second row, the distance was able to be measured for

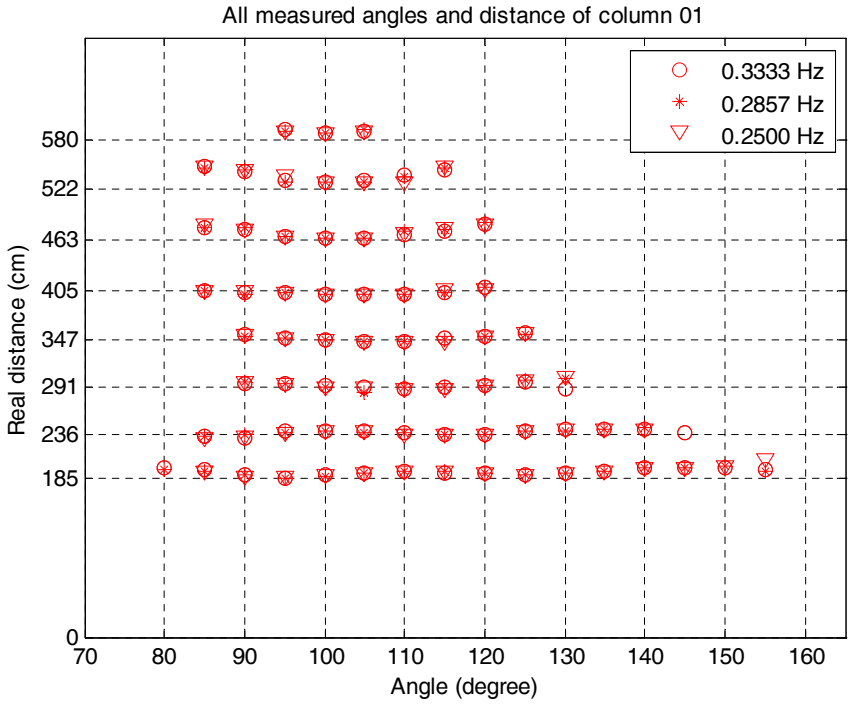

Figure 6.17: *Result of column number 01 (see Figure 6.4).*

13 angles with a sensitive range 85° to 145°. In the third row, the distance was able to be measured for 9 angles with a sensitive range 90° to 130°. According to the Figure 6.17 the sensitive ranges of the rest and first three rows are shown in Table 6.2.

The predicted distance compared to the real distance is shown in the same Figure 6.17. The numbers of angles which produce a measurement vary at different distances. The larger the distance, the less the measurable angles. The result for 0.25 Hz at 155° in the first row deviates slightly from 0.3333 and 0.2857 Hz, and the 0.3333 Hz at 130° in the third row deviates slightly from 0.2857 and 0.25 Hz. The reason is that both of the angles are on the edge of all measured angles. This situation could happen and is tolerable in practical applications. The second row

Table 6.2: The sensitive ranges for column 01.

position	sensitive ranges
The 1^{st} row	80° to 155°
The 2^{nd} row	85° to 145°
The 3^{rd} row	90° to 130°
The 4^{th} row	90° to 125°
The 5^{th} row	85° to 120°
The 6^{th} row	85° to 120°
The 7^{th} row	85° to 115°
The 8^{th} row	95° to 105°

only gets a result for 0.3333 Hz at 145°. That is also tolerable in practical situations.

Generally speaking, the range of measurable angles depends on the antenna beamwidth of different frequencies. The gain of horn antennas often increases and the beamwidth decreases as the frequency of operation is increased. At lower frequencies, a wider beamwidth and lower gain occurs than at higher frequencies. The lower frequency part is used to detect life parameters in a both wider and shorter range. On the other side, the higher frequency part is used to find out expected data in a narrower and longer area. There is a trade off between beamwith and dynamic range.

Figure 6.18 shows measured distance of 8 different positions for column 05. The angles of the simulator also change in steps of 5 degrees as the same as column 01. The first to eighth row has measured at a distance with 30, 27, 17, 17, 11,

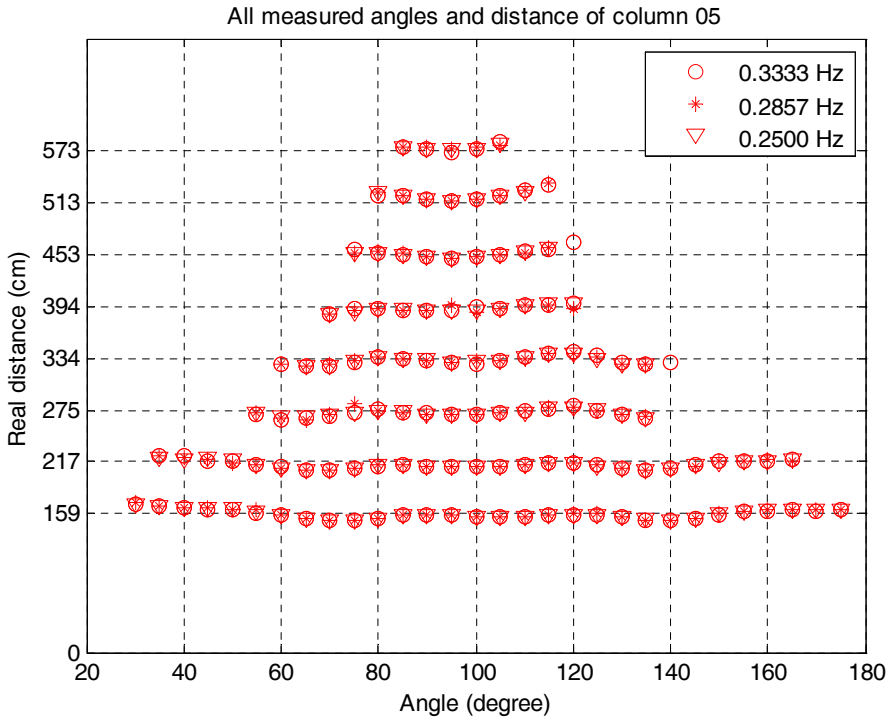

Figure 6.18: *Result of column number 05 (see Figure 6.4).*

10, 8 and 5 angles. The sensitive ranges are shown in Table 6.3. The predicted distance compared to the real distance is shown in this figure. The numbers of angles which produce a measurement vary at different distances. The higher the distance is, the less the measurable angles are. The forth row at 140° and the sixth row at 120° only gets a result for 0.3333 Hz. This situation can happen but is tolerable in practical applications.

Figure 6.19 shows measured distance of 8 different positions for column 10. The angles of the simulator also change in steps of 5 degrees. The first to eighth row has measured at a distance with 31, 26, 24, 12, 10, 9, 8 and 5 angles. According to those angles, the sensitive ranges can be determined and shown in Table 6.4. The predicted distance in comparison to the real distance is shown clearly in this

Table 6.3: The sensitive ranges for column 05.

position	sensitive ranges
The 1^{st} row	30° to 175°
The 2^{nd} row	35° to 165°
The 3^{rd} row	55° to 135°
The 4^{th} row	60° to 140°
The 5^{th} row	70° to 120°
The 6^{th} row	75° to 120°
The 7^{th} row	80° to 115°
The 8^{th} row	85° to 105°

figure. The numbers of angles which produce a measurement vary at different distances. The more distance, the less are the measurable angles. The first row at 160° and the forth row at 115° only gets a result for 0.3333 Hz. That could be 0.3333 Hz higher than the other. The third row at 150° only gets 0.3333 and 0.2857 Hz. This situation can also happen but is tolerable in practical applications.

Figure 6.20 also shows measured distance of 8 different positions from column 15. The angles of the simulator also change in steps of 5 degrees like in Figures 6.17, 6.18 and 6.19. The first to eighth row has measured distance with 16, 13, 10, 10, 8, 8, 7 and 2 angles and the sensitive ranges have been shown in Table 6.5. In this figure, the predicted distance in comparison to the real distance is seen clearly. The numbers of angles which produce a measurement vary at different distances. The higher distance, the less are the measurable angles as mentioned before. The first row at 100° and the forth row at 95° only get 0.3333 and 0.2857 Hz. The

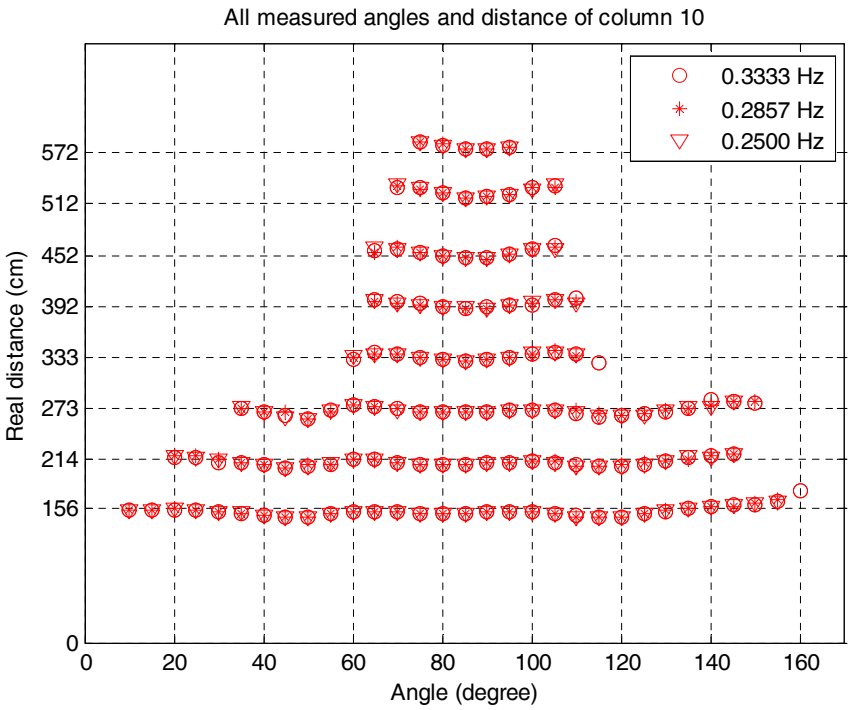

Figure 6.19: *Result of column number 10 (see Figure 6.4).*

Table 6.4: The sensitive ranges for column 10.

position	sensitive ranges
The 1^{st} row	10° to 160°
The 2^{nd} row	20° to 145°
The 3^{rd} row	35° to 150°
The 4^{th} row	60° to 115°
The 5^{th} row	65° to 110°
The 6^{th} row	65° to 105°
The 7^{th} row	70° to 105°
The 8^{th} row	75° to 95°

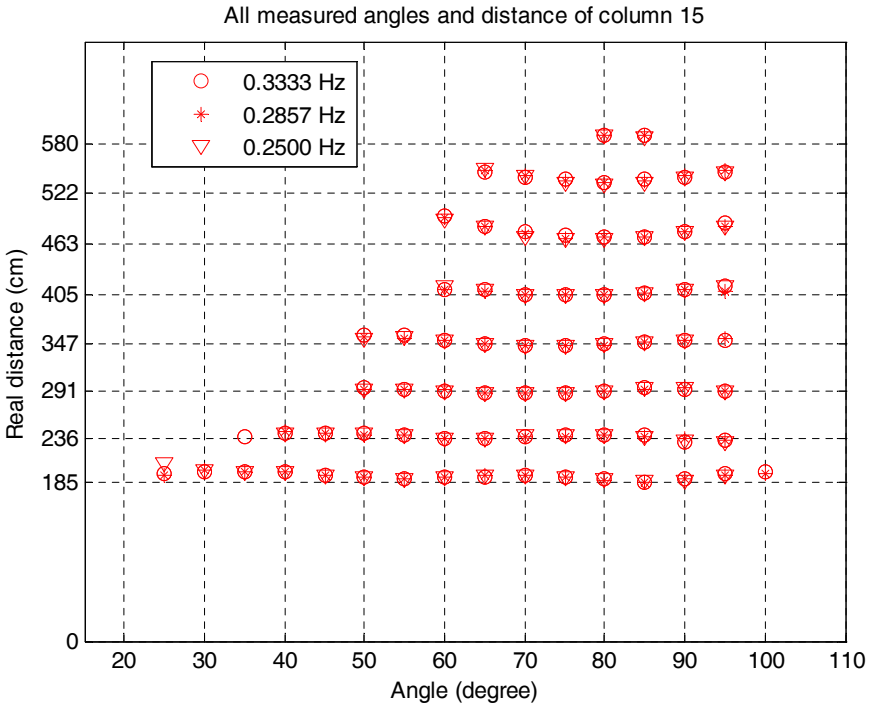

Figure 6.20: *Result of column number 15 (see Figure 6.4).*

second row at 35° only gets a result for 0.3333 Hz. This situation can also happen but is tolerable in practical applications.

Comparing Figures 6.17 - 6.20, there is no symmetrical result between them. The reason includes the error of the antennas setup and the position and different angles of the simulator. The almost homogeneous wall also can cause a very small error. This error is permitted in this situation and measurement. In addition, sometimes the errors for one or two breath frequencies were missed at the edge of the sensitive angle range in Figures 6.17 - 6.20. Those one are tolerable in real applications.

In Figure 6.12 there is a peak value in the main frequency called a relative ampli-

Table 6.5: The sensitive ranges for column 15.

position	sensitive ranges
The 1^{st} row	25° to 100°
The 2^{nd} row	35° to 95°
The 3^{rd} row	50° to 95°
The 4^{th} row	50° to 95°
The 5^{th} row	60° to 95°
The 6^{th} row	60° to 95°
The 7^{th} row	65° to 95°
The 8^{th} row	80° to 85°

tude. Every main frequency has its own relative amplitude. In Figures 6.21 - 6.24 there are four figures to show the relative amplitude of angles in the sensitive range in different rows after smoothing. The X-axis shows measured angle and the Y-axis shows relative amplitude. "Row 1",..., "row 8" means the row distance away from the X-axis is 150 cm to 510 cm with a step 60 cm respectively. The angles extend beyond both sides of the TRA as mentioned above and the size of sensitive range depends on the row distance. In Figure 6.21, all measured angles and magnitudes of column 02 with breath frequency 0.3333 are shown. The highest relative amplitude is over 0.017 V and happens at 120° of row 1 which is nearest to the antennas. The farther the distance of the row, the lower the main amplitude. This sensitive angle with the highest relative amplitude is called P-angle. For every row the P-angle is in its middle area and also in TRA range. The P-angles move from 120° of row 1 toward the left 100° of row 8. The convergence of reasonable angles is a little toward the left, around 90° to 105°. The reason

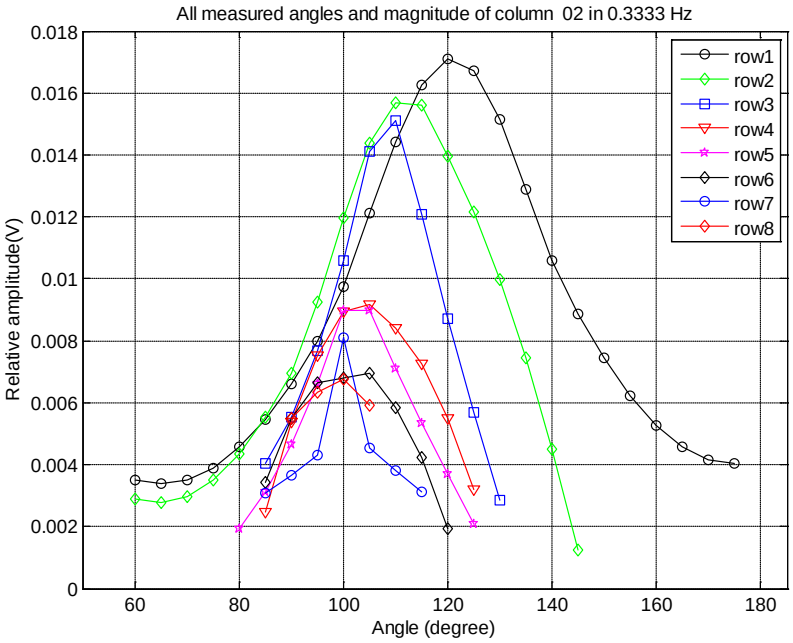

Figure 6.21: *Relative powers of angles with different rows in column 02.*

could be that column 02 is on left side of the Y-axis.

Similarly, Figure 6.22 shows all measured angles and magnitudes of column 05 for breath frequency 0.3333. The X-axis shows measured angle and the Y-axis shows relative amplitude. For column 05, the highest relative amplitude is approximately 0.06 V, happens in row 1 like column 02. The same principle as with Figure 6.21 applies, the farther the distance of the row, the lower the main amplitude. In each row of this column P-angle is in its middle area. And these angles happen in TRA range precisely. The P-angles move from 105° of row 1 toward the left 95° of row 8. The convergence of reasonable angles is a little toward the left, around 85° to 105° and the sensitive ranges are wider than column 02. The reason could be that the position of column 05 is slightly on the left side.

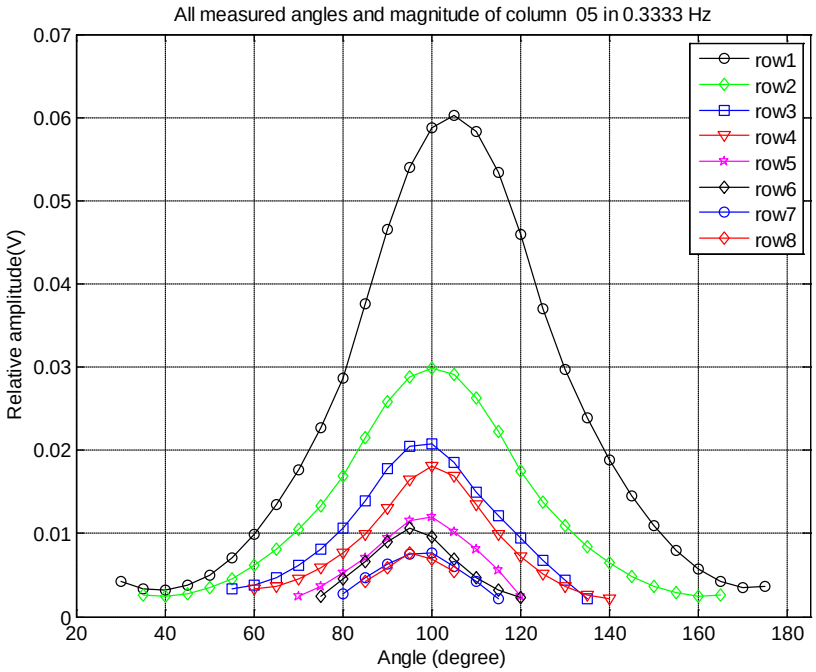

Figure 6.22: *Relative powers of angles with different rows in column 05.*

In the Figure 6.23, all measured angles and magnitude of the middle column 08 for breath frequency 0.3333 are shown. The highest relative amplitude approximately 0.07 V happened in the row 1 which is nearest to the antennas. For the same reason as with Figures 6.21 and 6.22 the farther the distance of the row, the lower the main amplitude. In every row the P-angle has been found in its middle area. In a precise expression, the P-angles appear in TRA range. The convergence of reasonable angles is around 80° to 100° and the sensitive ranges are wider than column 02 and 05. The reason could be that the position of column 08 is the Y-axis.

Figure 6.24 shows all measured angles and magnitudes of column 12 for the breath frequency 0.3333 Hz. The highest relative amplitude approximately 0.425 V has been found in row 1. The farther distance of the row, the lower is the main am-

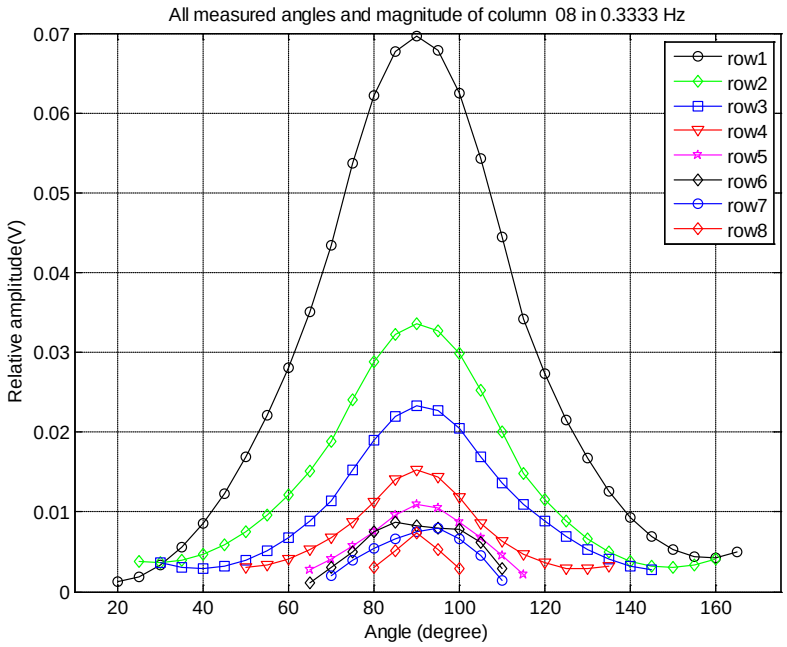

Figure 6.23: *Relative powers of angles with different rows in column 08.*

plitude. In each row of this column the p-angle is also in its middle area (TRA) as same as column 02, 05 and 08. The convergence of sensitive angles shifted toward a little right side than column 08 is about 70° to 90° and the sensitive ranges are wider than column 02 but narrower than column 05 and 08. The reason could be the position of column 12 is farther in comparison to column 05 and 08 but closer to the Y-axis than column 02.

To summarize the results of this measurement, an application was made of a UWB radar system with a breath simulator (UWBSBS) and signal processing according to the previous algorithm as a two-dimensional measurement. The system can control both simulator speeds to imitate human breath frequency and measure the breath frequency at the same time. The whole process of life detection in this case is also done automatically. The results of this process which takes more or

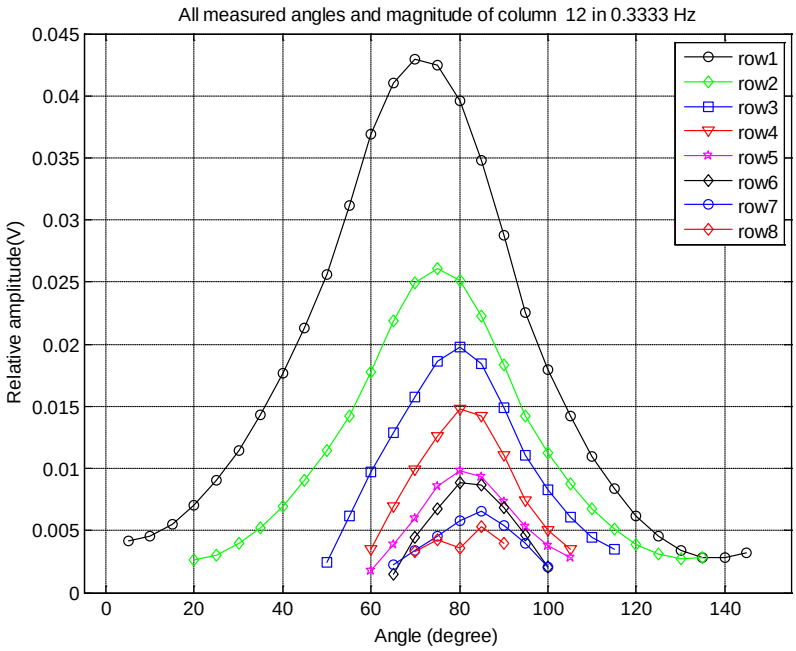

Figure 6.24: *Relative powers of angles with different rows in column 12.*

less 22 seconds are distance and breath frequency determination of the person. The result of the first step has successfully verified the fast, robust and accurate algorithm in one- and two-dimensional measurements. And the use of the same algorithm, a measurement has been done in a given area of 210 cm × 570 cm, with 120 measurement points. The result is only certain angles can get the imitated breath frequency for each point. The angles extend beyond both sides of the TRA area. The higher the distance, the less angles are available to get breath frequency and the TRA gets smaller. The best results are obtained with angles where the object person is facing the line which connects the transmitting and receiving antenna. In every row, the highest relative amplitude is in its middle (TRA) area. The columns 02, 05, 08 and 12 were selected to represent columns 1 to 15, the peak amplitude becomes smaller values with larger distances and farther angles than P-angle.

Chapter 7

Conclusion

An ultra wideband radar system for breath and position detection of hidden humans has been presented in this research. By using a UWB radar it is possible to penetrate materials and detect the distance, position and chest movement of hidden persons. The UWB radar setup which is in one-dimensional measurement consists of a sub-nanosecond pulse generator, two wideband antennas and two low noise amplifiers. For a background subtraction, digital low pass filters are used to remove the background noise. The effect of human breath on the received signal is computed using the unbiased variance. This method is successful to find the expected data behind the noise. The FIR filtering is used to get the peak and interprets it as the position of a human being. Using the magnitude cycle rate with various numbers of averaged points, the breath frequency is determined easily. The more points used, the closer the frequency is to the real values. The algorithm is fast, accurate and robust. The whole process of life detection which contains sending and receiving microwave signals and processing of reflected signals is done automatically. The results of this process which takes approxi-

mately 12 seconds are position and breath frequency determination of the person. The presented results show that the radar system can easily determine almost accurately the position and breath frequency up to a distance of 4.75 m behind a wall.

In a two-dimensional measurement, three antennas are used in the UWB radar setup for sending and receiving pulses. The Vivaldi antenna is set to transmit the pulse. There are two double-ridged horn antennas which receive the reflected data independently. The receivers are put on the left and right hand sides of the transmitting antenna separated by a distance of 60 cm. The first of them is used to receive the reflected signals for 20 seconds and than it is switched to the other one. For the signal processing, we still use the one-dimensional algorithm and use a zero-phase FIR filter instead of the FIR filter to get the peak of effects and then transform it to the position of the human. The whole process of life detection in the two-dimensional case was done automatically like the one-dimensional one. The results of this process which takes about 44 seconds are position and breath frequency determination of the person. The presented results of four kinds of measurement show that the radar system can easily determine both the 2D position and respiratory frequency up to a distance of 4 meters from the radar X-axis to the person.

An application of UWB radar system with a breath simulator (UWBSBS) for remote measurement of the position and respiration of hidden persons in varying positions and angles has been presented. There are two double-ridged horn antennas for the UWB set-up. The receiving antenna is set up at the right side of the transmitting antenna at a distance of 60 centimeters. The antennas are also

arranged on the X-axis and facing the Y-axis at an angle of around 10 degrees. The signal processing follows the previous algorithm for the two-dimensional measurement. The system can control both simulator speeds to imitate human breath frequency and measures the breath frequency simultaneously. The whole process of life detection in this case is also done automatically. The results of this process which takes approximately 22 seconds are distance and breath frequency determination of the person. The result of a first step successfully verifies the algorithm for one- and two-dimensional measurements. And measurements using the same algorithm have been done in a given area of 210 cm $\times$ 570 cm, with 120 measurement points. The result is that only at some angles can get the imitated breath frequency for each point. The angles extend beyond both sides of the TRA area. The higher the distance, the less angles are possible to get breath frequency and the smaller the TRA will be. For each point, the highest amplitude is in the TRA area. As a summary of the result in this measurement, the best angles for measurement are in the TRA area. In other words, for getting the best measurement results, the best sensitive angle for the object person is facing the line which connects the transmitting and receiving antennas.

For the given measurements there were four challenges: The first problem was not only the error from the effect of the wall with different permittivity and thickness but also the wave transmitting angle toward the wall. The second problem was that the signal processing was not fast, robust and accurate enough for an application. The third problem was building an automatic system. The last problem was that the surface of human chest was not smooth and the chest movement in front of a human was more intensive than at the back. In this research, an

automatic system with a fast, robust and accurate algorithm has been developed. A one-dimensional and four kinds of two-dimensional measurements have been performed and good results were achieved. An automatic system is used with a breath simulator to find the best sensitive angles. The breath simulator provides a good reference system.

In the future, there are four matters which could be done:

1. Upgrade or optimize the algorithm to apply it to more practice situations, for example, in ground or in ice.
2. Enhance the system to be a commercial product.
3. Based on the best angle results, develop a double or triple system to cover more measurement angles to find a person behind a wall.
4. Develope a 3D system based on this technology.

The challenges mentioned above are fulfilled with the system presented in this work. An automatic UWB system with a fast, robust and accurate algorithm for signal processing has been improved to be applied in practical situations. The system is used to perform one- and two-dimensional measurements for the position and breath frequency of person behind a wall. The development of a reference breath simulator has been successful to achieve the characteristics of breathing at different angles. These results could be used for rescue operations to find persons quickly. Two setups would complete the sensitive angles. The system could also be used for medical measurement of patients in hospital or at home to get stable life data.

Bibliography

[1] I. Oppermann, M. Hamalainen, and J. Iinatti, *UWB Theory and Applications*. John Wiely and Sons Ltd., 2004.

[2] E. J. Rothwell, K. M. Chen, D. P. Nyquist, and J. E. Ross, "Time-domain imaging of airborne targets using ultra-wideband or short-pulse radar," *Antennas and Propagation, IEEE Transactions on*, vol. 43, pp. 327–329, 1995.

[3] C. H. Liao, L. D. Fang, P. Hsu, and D. C. Chang, "A UWB microwave imaging radar system for a small target detection," *Antennas and Propagation Society International Symposium*, pp. 1–4, 2008.

[4] M. J. Seitz, O. H. Schaub, and R. Zetik, "UWB feature localization for imaging ultra-wideband," *ICUWB IEEE International Conference*, vol. 2, pp. 199–202, 2008.

[5] I. H. Naqvi, A. Khaleghi, and G. Elzein, "Performance enhancement of multiuser time reversal UWB communication systeml," *Wireless Communication Systems, ISWCS 2007*, vol. 4th International Symposium on, pp. 567–571, 2007.

[6] T. Li, Y. Rao, and Z. Niu, "Analysis and design of UWB Vivaldi antennas," *Microwave Antenna, Propagation and EMC Technologies for Wireless Communi-*

cations, vol. 2007 International Symposium on 10.1109/MAPE.2007.4393685, pp. 579–581, 2007.

[7] L. Lizzi, M. D. Migliore, D. Pinchera, F. Schettino, M. Benedetti, R. Azaro, and A. Massa, "Experimental channel characterization of a MIMO-UWB communication system," *Antennas and Propagation Society International Symposium, AP-S 2008 IEEE*, pp. 1–4, 2004.

[8] L. Carin, N. Geng, M. McClure, J. Sichina, and L. Nguyen, "Ultra-wide-band synthetic-aperture radar for mine-field detection," *Antennas and Propagation Magazine, IEEE*, vol. 41, pp. 18–33, 1999.

[9] G. Ossberger, T. Buchegger, E. Schimback, A. Stelzer, and R. Weigel, "Noninvasive respiratory movement detection and monitoring of hidden humans using ultra wideband pulse radar," *Ultra Wideband Systems, Joint with Conference on Ultra Wideband Systems and Technologies, International Workshop on 18-21*, pp. 395–399, May 2004.

[10] S. L. Earp, E. S. Hughes, T. J. Elkins, and R. Vickers, "Ultra-wideband ground penetrating radar for the detection of buried metallic mines," *Aerospace and Electronic Systems Magazine, IEEE*, vol. 11, no. Issue: 9, pp. 30–39, 1996.

[11] Y. Chen, E. Gunawan, K. S. Low, Y. Kim, C. B. Soh, A. R. Leyman, and L. L. Thi, "Non-invasive respiration rate estimation using ultra-wideband distributed cognitive radar system," *Engineering in Medicine and Biology Society, 28th Annual International Conference, IEEE*, pp. 920–923, 2006.

[12] M. Y. W. Chia, S. W. Leong, C. K. Sim, and K. M. Chan, "Through-wall UWB radar operating within FCC's mask for sensing heart beat and breathing rate," *Radar Conference, 2005 European*, vol. 3, pp. 267–270, OCT. 2005.

[13] E. M. Staderini, "UWB radars in medicine," *Aerospace and Electronic Systems Magazine, IEEE*, vol. 17, pp. 13–18, 2002.

[14] A. G. Yarovoy, L. P. Ligthart, J. Matuzas, and B. Levitas, "UWB radar for human being detection," *Aerospace and Electronic Systems Magazine, IEEE*, vol. 21, pp. 22–26, 2006.

[15] N. V. R. S. Venkatesh, C. Anderson and R. M. Buehrer, "Implementation and analysis of respiration-rate estimation using impulse-based UWB," *IEEE Military Communications Conference*, pp. 395–399, OCT. 2005.

[16] K. Kang, I. Maravic, and M. Ghavami, "Ultra-wideband respiratory monitoring system," *Ultra Wideband Systems, Technologies and Applications, 2006.*, pp. 191–195, 2006.

[17] P. C. Clemmow, *The plane wave spectrum representation of electromagnetic fields*. IEEE Press, 1996.

[18] L. F. Chen, C. K. Ong, C. P. Neo, V. V. Varadan, and V. K. Varadan, *Microwave electronics: measurement and materials characterizations*. John Wiely and Sons Ltd., 2004.

[19] *Dielectric properties of Body Tissues, Italian National Research Council, Florence Italy*, http://niremf.ifac.cnr.it/tissprop/htmlclie/htmlclie.htm.

[20] K. Kimura and O. Hashimoto, "An experimental study on the installation effect of the EM wave absorber to wireless LAN communication environ-

ment," *Electromagnetic Compatibility, 2005 International Symposium on*, vol. 1, pp. 130–134, 2005.

[21] M. Miyakawa, K. Yaguchi, N. Ishii, T. Saeki, and Y. Kanai, "Accuracy improvement in permittivity measurement of construction materials by use of a model of the standing wave method in free space," *Electromagnetic Compatibility, IEEE International Symposium on*, vol. 2, pp. 809–814, 2002.

[22] D. M. Pozar, *Microwave engineering*. University of Massachusetts at Amherst, 1990.

[23] D. Schlichthaerle, *Digital filter: basic and design*. Springer, 2000.

[24] E. C. Ifeachor and B. W. Jervis, *Digital signal processing-a practical approach*. Prentice Hall, 2002.

[25] J. G. proakis and D. G. Manolakis, *Digital signal processing-principles, algorithms, and applications*. Prentice Hall, 1996.

[26] *Manufacture datasheet of Fujitsu F^{2}MC-16LX 16-bit microcontroller MB90595 series hardware manual*, http://edevice.fujitsu.com/fj/MANUAL/MANUALp/en-pdf/CM44-10106-6E.pdf.

[27] *Manufacture Datasheet of National Semiconductor DAC121S101*, http://www.national.com/ds/DA/DAC121S101.pdf.

[28] *Manufacture Datasheet of STMicroelectronics Positive voltage regulators L7805CV*, http://www.st.com/internet/com/TECHNICAL_RESOURCES/TECHNICAL_LITERATURE/DATASHEET/CD00000444.pdf.

[29] *Manufacture Datasheet of STMicroelectronics Complementary silicon power Darlington transistors*, http://www.st.com/internet/com/TECHNICAL_RESOURCES/TECHNICAL_LITERATURE/DATASHEET/CD00000939.pdf.

[30] *Manufacture Datasheet of Photomicrosensor EE-SX672*, http://www.ia.omron.com/data_pdf/data_sheet/ee-sx47_67_ds_csm483.pdf.

[31] *Operation Manual V3-00 of Fujitsu F^{2}MC-16 Family Softune Workbench*, http://www.fujitsu.com/downloads/MICRO/fma/pdfmcu/CM41-00312-3E.pdf.